PROBING AND OVERCOMING EXTRACELLULAR BARRIERS TO INHALED NANOMEDICINE

by

Benjamin S. Schuster

A dissertation submitted to Johns Hopkins University in conformity with the
requirements for the degree of Doctor of Philosophy

Baltimore, Maryland

August, 2014

Abstract

Inhaled nanoparticles are a promising technology for delivering therapeutic molecules to the lungs to treat diseases such as cystic fibrosis (CF) and lung cancer. This dissertation focuses on characterizing and overcoming a critical extracellular barrier to inhaled nanomedicine: the mucus gel that coats the lung airway epithelium. Mucus is an adhesive meshwork that can trap particles and facilitate their removal from the lungs via mucociliary clearance. Although this defense mechanism protects the lungs from pathogens and particulate pollution, it can also prevent inhaled drug and gene nanoparticles from reaching their target. We therefore investigated strategies to improve particle penetration through human lung mucus. To measure nanoparticle transport, we used multiple particle tracking, a high resolution microscopy technique for quantifying movement of individual particles.

First, we examined how particle size and surface chemistry affect mobility in respiratory mucus. We prepared polymeric nanoparticles densely coated with low molecular weight polyethylene glycol (PEG) to minimize muco-adhesion, and compared their transport to that of uncoated, muco-adhesive particles in respiratory mucus collected from endotracheal tubes of surgical patients without pulmonary comorbidities. We found that 100 and 200 nm diameter PEG-coated particles rapidly penetrated respiratory mucus, at rates exceeding their uncoated counterparts by more than one order of magnitude. In contrast, coated and uncoated particles 500 nm in diameter were sterically immobilized by the mucus mesh. These findings identify small size and adhesion-resistant surface as design criteria for therapeutic, respiratory-mucus-penetrating nanoparticles.

Next, we studied viruses – nature's nanoparticles – for CF lung gene therapy. We investigated whether CF sputum acts as a barrier to adeno-associated virus (AAV) gene vectors including AAV2, the serotype tested in CF clinical trials, and AAV1, a leading candidate for future trials. We found that sputum strongly impeded diffusion of AAV, regardless of serotype, and may thereby inhibit access to target cells. However, an AAV2 mutant engineered to have reduced heparin binding diffused twice as fast as AAV2 on average, presumably because of reduced adhesion to sputum. We also discovered that the mucolytic N-acetylcysteine could markedly enhance AAV diffusion. These studies offer strategies for increasing AAV penetration through sputum to improve clinical outcomes.

Advisor: Justin Hanes, Ph.D.

Readers: Justin Hanes, Ph.D.; Richard Cone, Ph.D; Scot Kuo, Ph.D.

Acknowledgements

During my undergraduate days at the University of Minnesota, I spent many hours studying in the ornate second floor of Walter Library. Sometimes, when I needed to stretch my legs, I would walk around the perimeter of the north reading room, whose walls were lined with shelves of science and engineering Ph.D. theses from the past few decades. I would pull a thesis off the shelf, read the title, and then flip to the Acknowledgements. Therein lay a glimpse of the people and personalities behind the research. I peered into the future and wondered: If one day I have the opportunity to write my own Acknowledgements, where would I be and whom would I be thanking?

That day has arrived, and I am grateful to say I have a long list of individuals to acknowledge. Some of these individuals helped me conduct, and learn how to conduct, research here at Johns Hopkins. Others have helped me live a more complete, friend-filled life. For both, I am grateful. My list of acknowledgements is long enough that I will surely, inadvertently, omit someone, and for that I apologize.

First, I thank my advisor, Dr. Justin Hanes, who has impressed upon me the importance of big-picture thinking and of pursuing important research questions. I am grateful to Drs. Scot Kuo, Richard Cone, and Bill Guggino for serving on my thesis committee and for their guidance on microscopy, biophysics, and cystic fibrosis, respectively. I also thank Dr. Joel Bader for serving on my qualifying exam committee and for advice. I am indebted to Dr. Michael Boyle for sharing his clinical expertise, for his assistance with collecting cystic fibrosis patient specimens, and for also serving on my qualifying exam committee.

I am indebted to my predecessors and colleagues in the Hanes Lab for showing me the ropes and teaching me how to do research. I thank Dr. Anthony Kim for many scientific discussions and ideas, and for his friendship and encouragement. It has been a pleasure to share a lab bay with my classmate Tao Yu, with whom I have enjoyed many philosophical conversations about research and life. I acknowledge Dr. Jung Soo Suk for his assistance with designing experiments, and for his tireless editing to improve the structure and clarity of my papers. I thank Dr. Graeme Woodworth for helping me initiate my first project, for his clinical insight, and for his assistance collecting patient specimens. Drs. Craig Schneider, Laura Ensign, and Elizabeth Nance were a hard-working, productive, and impressive trio to follow into the lab. They set a high bar and were always generous with their time. Jane Chisholm deserves special praise for being the most selfless, all-around helpful member of the Hanes Lab. It has been fun to watch Clark Zhang, Dr. Panagiotis Mastorakos, and Katharina Maisel join the lab and make impressive contributions of their own. Drs. Ying-Ying Wang, Qingguo Xu, and Himat Patel also deserve thanks for assistance at the early stages of my research. I appreciate the behind-the-scenes work of Nicole Turner and Joseph Vargas to keep the lab running.

A few other colleagues merit special mention. Daniel Allan has been a fantastic collaborator during the past year and a half. I am grateful for the insightful discussions we have had about particle tracking, soft matter physics, and scientific programming, and I look forward to our continued collaboration. My undergraduate research assistants, Joshua Kays and Mia Kanzawa, were stellar. I thank them for their help with experiments and for their dedication. Having the opportunity to mentor Josh and Mia, envision projects with them, watch their projects come to fruition, and see them grow in the process has been one of the most enjoyable aspects of my Ph.D. experience.

I also owe a big thanks to the many friends I have met and who have made Baltimore home during these past six years. Countless potluck meals and Ultimate Frisbee games have been a wonderful way to spend time outside of lab. In particular, I thank Drs. Shimon Unterman and Natan Davidovics, who helped me get established in Baltimore and started in the BME Ph.D. program.

Most of all, I am grateful for my family. I thank my parents for their love and support and for inspiring me to pursue science in service to humanity. My dear wife, Aliza, deserves that I write a whole book of thanks to her, but I will spare her the embarrassment. We met early during our time in Baltimore and have been through most of this Ph.D. together. Aliza, your love and kindness has brought me immeasurable joy and has supported me these past few years. Thank you. I look forward to a lifetime of adventures together.

Perhaps someday, an aspiring young scientist or engineer eager to begin his or her own journey in research will pull my (digital) thesis off the (electronic) shelf. Hopefully these Acknowledgements will serve as a reminder that, behind all the technical jargon and impersonal prose in the pages that follow, this research was built upon the contributions of many, much appreciated individuals.

Table of Contents

List of Tables

List of Figures

1. INTRODUCTION

1.1. Overview and significance

Inhaled nanoparticles are a promising approach for delivering therapeutic molecules to the lungs with increased efficacy and decreased side effects. Examples of inhaled nanomedicines currently under investigation include gene vectors for cystic fibrosis (CF), chemotherapeutic-loaded particles for lung cancer, and antibiotic nanoparticles for lung infections.[1] However, extracellular barriers can trap inhaled nanoparticles and prevent the therapeutic cargo from reaching its intended site of action. This dissertation is about characterizing extracellular barriers to inhaled nanomedicines, and overcoming these barriers for therapeutic applications. Specifically, we focus on the viscoelastic mucus gel that coats the lung airways. Mucus can trap particles and facilitate their removal from the lungs by mucociliary clearance, rendering the therapeutic nanoparticles less effective.

A key experimental method we used in these investigations was particle tracking, an optical microscopy technique for recording the motion of individual particles in complex environments at high spatial and temporal resolution. We implemented a user-friendly automated tracking code in MATLAB, based on the established algorithm of Crocker and Grier,[2] which enabled us to process hundreds of particle tracking videos and analyze tens of thousands of particle trajectories. Following this introductory chapter, we discuss particle tracking methods for drug and gene delivery in Chapter 2 (and we provide the tracking code in the Appendix). The transport rate measured by particle tracking indicates the ability of a specific nanoparticle type to penetrate a given biological specimen and reach the desired therapeutic target.

A major role of respiratory mucus is to trap inhaled particles, including pathogens and environmental particulates, to limit body exposure. Despite the tremendous health implications, how particle size and surface chemistry affect mobility in respiratory mucus from humans without lung disease was not known until our work in Chapter 3. We prepared polymeric nanoparticles densely coated with low molecular weight polyethylene glycol (PEG) to minimize muco-adhesion, and compared their transport to that of uncoated, muco-adhesive particles in human respiratory mucus, which we collected from the endotracheal tubes of surgical patients with no respiratory comorbidities. We found that PEG-coated particles 100 and 200 nm in diameter rapidly penetrated respiratory mucus, at rates exceeding their uncoated counterparts by approximately 15- and 35-fold, respectively. In contrast, PEG-coated particles ≥ 500 nm in diameter were immobilized by the mucus mesh. Thus, even though respiratory mucus is a viscoelastic solid at the macroscopic level (as measured using a bulk rheometer), nanoparticles that are sufficiently small and non-adhesive can penetrate the mucus as if it were primarily a viscous liquid. These findings help elucidate the barrier properties of respiratory mucus and provide design criteria for therapeutic nanoparticles capable of penetrating mucus to approach the underlying airway epithelium.

Next, we studied lung gene therapy for CF, which we describe in Chapter 4. CF is caused by a genetic defect in the CFTR chloride channel, and while this defect affects a number of organs, lung disease is the greatest cause of morbidity and mortality in CF patients. Despite promising preclinical studies, gene therapy has not yet improved CF patient lung function in human trials. In the human CF lung, inhaled gene vectors must penetrate the viscoelastic secretions coating the airways to reach target cells in the underlying epithelium. We investigated whether CF sputum acts as a barrier to leading adeno-associated virus (AAV) gene vectors, including AAV2, the only serotype tested in CF clinical trials, and AAV1, a leading candidate for future trials. We found that sputum strongly impeded diffusion of AAV, regardless of serotype, by adhesive interactions and steric obstruction. Approximately 50% of AAV vectors diffused >1,000-fold slower in sputum than in water, with large patient-to-patient variation. We thus tested two strategies to improve AAV diffusion in sputum. We showed that an AAV2 mutant engineered to have reduced heparin binding diffused twice as fast as AAV2 on average, presumably because of reduced adhesion to sputum. We also discovered that the mucolytic N-acetylcysteine could markedly enhance AAV diffusion by altering the sputum barrier properties. These studies underscore that sputum is a major barrier to CF gene delivery, and offer strategies for increasing AAV penetration through sputum to improve clinical outcomes.

Thus, in this dissertation we probed and tested strategies to overcome extracellular barriers to inhaled nanomedicines. We conclude with a future outlook on the field in Chapter 5.

1.2. Background

1.2.1. Cystic fibrosis and CF gene therapy

Cystic fibrosis is an autosomal recessive disorder that afflicts approximately 70,000 people worldwide.[3] CF is caused by a mutation in the CF transmembrane conductance regulator gene (*CFTR*) on chromosome 7.[4] The *CFTR* gene codes for an ion channel that conducts chloride across cell membranes. Approximately 4% of Caucasians carry one CF mutation.[5] Nearly 2,000 variants of the gene have been identified, of which 127 are known to be deleterious.[3] About 70% of defective *CFTR* alleles have the most common mutation, called F508del, which causes defective maturation and premature degradation of the CFTR protein.[4]

Cystic fibrosis affects the mucus-covered lumens of the body, including the lungs, pancreatic ducts, reproductive tract, and GI tract. Lung disease is the main source of morbidity and mortality in CF. A vicious cycle of impaired mucociliary clearance, infection, and inflammation takes a toll over time, causing bronchiectasis and declining lung function. Approximately 90% of patients with CF also suffer from pancreatic enzyme insufficiency, and nearly all males with CF are infertile.[5,6] The median life span of CF patients has increased in recent decades, thanks to aggressive treatment. The three pillars of CF treatment are antibiotic therapy for lung infections, respiratory therapy to clear lung obstruction, and enzyme replacement and dietary supplementation to achieve nutritional repletion.[7] However, the median survival age of CF patients is still only approximately 40 years.[6]

The CF gene was discovered in 1989, opening the possibility of treating CF by delivering the correct gene to cells to mediate proper CFTR activity. Numerous clinical trials for CF gene therapy have been conducted during the past two decades, using both viral and non-viral vectors, including adenovirus, adeno-associated virus, and liposomes. However, the results have been disappointing. There are a variety of possible reasons for these poor results, including immune response to the vectors and poor cellular targeting.[8] In this dissertation, we investigated an important but often overlooked barrier to CF gene therapy: the sputum barrier that obstructs CF patients' lungs.

The gene therapy vector we studied here is adeno-associated virus (AAV), a leading viral vector currently under preclinical and clinical investigation for treating diseases of the lung, heart, liver, eye, and central nervous system.[9] Between 1999 and 2007, six clinical trials for CF were conducted using AAV serotype 2.[8] AAV is promising for gene therapy because it does not cause any known disease, induces only mild immune response, and can efficiently transduce many cell types. AAV is a non-enveloped virus with an icosahedral capsid. With a diameter of approximately 25 nm, it is among the smallest of viruses. Dozens of AAV serotypes have now been discovered, with different receptors and tissue tropisms. In the recombinant AAV vectors used for gene therapy, the wild-type genes are removed and replaced with the therapeutic genes of interest.

1.2.2. Drug and gene delivery to the lungs

Delivery of therapeutics via inhalation offers a number of advantages for treatment of lung diseases ranging from asthma to CF. Compared to systemic delivery, inhalation permits local delivery with reduced side effects, and may require lower doses to achieve the desired therapeutic outcome.[10] Inhaled therapeutics also avoid first-pass metabolism, which is an advantage relative to oral delivery.[1] Although the focus of this dissertation is delivery to the conducting airways, we note that delivery to the alveoli is useful for targeting alveolar macrophages or for rapid systemic delivery, since the alveoli have a large surface area and a rich blood supply.[1,11]

A number of devices are used to deliver medications to the lung. Metered-dose inhalers deliver a short burst of the therapeutic aerosol in a propellant. Dry powder inhalers deliver micron-sized drug particles, and no propellant is used. Nebulizers turn liquid solutions or suspensions into a fine mist, which is inhaled.[10] Particle deposition in the lungs is size-dependent. Large particles, with an aerodynamic diameter >5 μm, deposit by inertial impaction in the upper airways. Smaller particles, with 1-5 μm aerodynamic diameter, deposit deeper in the lungs by inertial impaction and sedimentation. The ideal size for deposition in the alveoli is 1-3 μm. A large fraction of particles under 1 μm remain suspended and are exhaled, though particles <100 nm may deposit in the alveoli by diffusion.[1]

Increasingly, nanoparticle drug carriers are being explored in many areas of medicine for their ability to provide controlled release of therapeutics and achieve improved pharmacokinetics.[1,11,12] Furthermore, for gene delivery, a virus or nano-sized vector is essential to protect the DNA cargo from enzymatic degradation and to facilitate cell entry and trafficking. For targeting the airways, drug nanoparticles and gene vectors are most often delivered by nebulization of the nanoparticle suspension. Nebulization permits control of droplet size and thus the location of deposition.[1,10]

1.2.3. Mucus, mucociliary clearance, and mucus-nanoparticle interactions

Mucus is a viscoelastic gel that lubricates and protects wet epithelial surfaces in the body, including the conducting airways of the lungs. Mucus is more than 90% water. The solid components of mucus include mucins, globular proteins, lipids, salts, and cell debris. Mucins are large glycoproteins, up to 3 megadaltons in molecular weight, which give mucus its viscoelastic properties. Mucins are highly glycosylated, with sugars comprising 50-90% of the dry weight. These sugars are O-linked, attaching to long, flexible mucin regions rich in proline, threonine, and serine (PTS domains). At the ends of most of the glycans are carboxyl or sulfate groups, which make mucins highly anionic. Mucins are stored in a dehydrated form, and upon secretion, the highly hydrophilic, negatively charged glycan-coated PTS domains swell with water.[13] The glycan-rich domains on mucins are interspersed with relatively short, glycan-poor, hydrophobic domains.[14] In the lung airways, the two main types of mucins are MUC5AC and MUC5B.[13] Both are rich in cysteine residues at their termini, which permits disulfide bonding between mucins. Mucins can also crosslink via Ca^{2+} and physically entangle. Together, these mechanisms are responsible for mucus viscoelasticity.[14]

In the lungs, mucus is continuously produced, secreted, and then removed by mucociliary clearance. The airway epithelium is comprised of ciliated cells and mucus-producing secretory cells; in the large airways (diameter > 2 mm), mucus is also produced in submucosal glands.[13] The mucus gel layer sits atop the periciliary layer, which is composed of membrane-bound mucins and other cell-grafted macromolecules.[15] Mucociliary clearance (MCC) and cough remove inhaled particles, pathogens, and even dissolved chemicals that could harm the lungs. MCC velocity is approximately 1 mm/min, but is highly dependent on the extent of mucus hydration and other variables.[13]

In disease states, mucus hydration and composition can change. CF, for instance, is characterized by a lack of luminal liquid. Furthermore, neutrophils are abundant in the inflamed CF lung, and dead neutrophils leave behind DNA and actin that can alter mucus rheology. It is also believed that decreased bicarbonate secretion, a consequence of the CFTR mutation, contributes to excess mucin crosslinking by Ca^{2+}.[13] Bacteria in infected CF lungs can secrete and envelop themselves in biofilms, which can also alter the rheology of CF airway secretions. The altered rheology contributes to poor MCC, which in turn promotes further lung infection, inflammation, and injury.

Nanoparticles can interact in a number of ways with a porous biological gel such as mucus. If the particle is not adhesive and is small relative to the mesh size of the gel, it will be able to diffuse through the pores of the gel. If the particle is small but adhesive, it may adhere to the gel fibers and be immobilized. If the particle is large relative to the mesh size of the gel, it will be caged and cannot readily diffuse through the gel.[16] This paradigm is worth remembering throughout the research chapters of this dissertation.

2. AUTOMATED PARTICLE TRACKING FOR APPLICATIONS IN NANOMEDICINE

2.1. Introduction

Successful nanoparticle-based drug and gene delivery depends on the transport behavior of the particles following their administration. To achieve therapeutic efficacy, drug and gene carriers must often diffuse through extracellular barriers,[17-19] and gene carriers must be transported to the cell nucleus.[20,21] Particle tracking is a powerful technique for studying transport processes by tracking the motion of individual particles at high spatial and temporal resolution using light microscopy. Particle tracking can quantify transport rates of drug carriers, imaging agents, synthetic gene vectors, and viruses in cells, tissues, and biological fluids.[22] Compared to earlier techniques, which measure average values over entire ensembles of particles, tracking with single-particle resolution permits the analysis of heterogeneous particle behavior.

Particle tracking has matured over the past three decades into a broadly accessible technique, useful in a variety of fields. Early applications were in cellular biophysics[23,24] and fundamental colloid science.[2] During the past 15 years, our lab and others have harnessed particle tracking for drug and gene delivery research. Particle tracking experiments can be conducted with microscopes and modern cameras that are now standard in biomedical research facilities. Numerous software packages for analysis of particle tracking videos are now freely available, and they can perform well even when studying complex biological specimens. Users do not require much, if any, prior programming experience to process even large data sets.

To facilitate even more widespread adoption of this powerful technique in the field of drug and gene delivery, we present a user-friendly introduction to particle tracking methods, review the state of the art in tracking algorithms, and discuss how to minimize errors to achieve reliable results.

2.2. Design of particle tracking experiments

Time-lapse videos of particles in a specimen are the raw data in particle tracking experiments. Collecting videos with the highest possible quality – in short, bright particles with high contrast against a uniform background – will greatly simplify data analysis and enable reliable interpretation. Three critical factors that influence video quality are the particles, microscope, and camera. Here, we provide guidelines for their selection and use. Optical properties of the biological specimen under investigation will also strongly impact the quality of videos that can be acquired, but those factors are typically beyond a researcher's control.

A variety of particles and illumination schemes can be used for particle tracking, including micron-sized colloids imaged via brightfield illumination,[2] and gold nanoparticles via darkfield microscopy.[25] However, we focus our discussion on fluorescent particles and fluorescence microscopy, which are particularly useful for identifying drug and gene delivery nanoparticles in heterogeneous biological materials. The more intensely fluorescent the particle, the more reliable the particle identification and localization. Bright, fluorescent polystyrene nanospheres are commercially available from companies such as Life Technologies, Bangs Laboratories, and Polysciences, and they are often used as model drug and gene nanoparticles in particle tracking studies.[17,18,26] For researchers interested in tracking nanoparticles prepared in their own laboratories, a number of fluorescent labeling strategies are possible. Particles can be internally labeled, either by physically encapsulating the fluorescent dye in the particle core (though this strategy is discouraged if dye leaks from the nanoparticle core), or by chemically conjugating the dye to a polymer from which the particle is then formulated.[18,19] Alternatively, a particle can be externally labeled by chemically conjugating fluorescent dye to functional groups on the particle surface. Internal labeling is preferable, as it is less likely to change the surface properties of the particle and alter the particle's interaction with the specimens of interest. Internally labeled particles are also more photostable than externally labeled particles, in general. Many fluorescent dyes, with various chemical reactivities, are commercially available, though photostable dyes with high quantum yield and extinction coefficient should be selected whenever possible.[27] The color of the fluorophore is another critical consideration. Biological specimens often have high autofluorescence, especially at shorter excitation wavelengths, which can interfere with particle detection and tracking. Thus, red or dark red fluorescent dyes may be advantageous.

Although some research groups use microscopes specially designed and optimized for particle tracking,[28] custom-built instrumentation is not required. In fact, particle tracking videos can be collected using hardware common in biomedical research labs and core facilities.[29] For tracking of fluorescent particles, a widefield microscope with epifluorescence illumination and appropriate fluorescence filter sets is typically used. Objectives with large numerical aperture are ideal for high resolution particle tracking, since they collect more light, and tracking precision is proportional to the square root of the number of photons emitted by a fluorescent particle.[29] A high-powered light source, such as a mercury or metal halide arc lamp, should be used at its highest intensity setting. Then, the exposure time of the camera should be adjusted so that the image is neither under- nor over-saturated.[29] This procedure will minimize particle tracking errors, as discussed in a later section. The microscope should be placed on a pneumatic vibration-isolation table to dampen any external vibrations, such as from footsteps and lab equipment. If the microscope stage is to be heated for the experiment, the temperature should be at equilibrium before collecting tracking videos, to prevent sample drift arising from expansion or contraction of microscope components.

A sensitive (high quantum efficiency), low-noise camera is essential for precise particle tracking. The best choice is an electron-multiplying charge coupled device (EMCCD) camera, though scientific complementary metal oxide semiconductor (sCMOS) cameras can be used as well.[30] The required frame rate will depend on the particle dynamics and research question. We have found 15 frames per second to be sufficient for studying transport of particles with diameters on the order of 100 nm in biological fluids and tissues, including mucus, vitreous, and brain tissue. Faster frame rates will be necessary for studying more rapid movement. If the exposure time can be set independently of the frame rate, the exposure should be no longer than necessary to achieve bright particle images. The rationale behind this guideline will be discussed in the section on errors in particle tracking. Although particle tracking videos are large files, it is important that the data be saved in a file format with lossless compression, since lossy compression discards data and worsens the tracking resolution.[29]

Two rules should be kept in mind when preparing specimens for particle tracking experiments. First, when possible, the chamber containing the specimen should be well sealed to minimize sample evaporation and convective flow during the experiment. Second, the particle concentration must be appropriate for visualizing and tracking individual particles. The average particle spacing must be larger than the average particle displacement from frame to frame, or else the paths of multiple particles will intermingle, making it difficult to accurately construct individual trajectories. If the particles are moving very rapidly, a faster frame rate can be used, but if that is not sufficient or feasible, a new specimen with lower particle concentration should be prepared.

When performing particle tracking using unfamiliar hardware or software, it is helpful to track particles in a simple fluid with known viscosity, like water or glycerol, and verify that the diffusion coefficients can be measured to within a few percent of the value predicted by the Stokes-Einstein equation. Note well that simple systems give cleaner images than most biological systems; treat them as a best-case scenario.

2.3. Extracting quantitative measurements from particle tracking videos

2.3.1. Automated particle tracking using the Crocker and Grier algorithm

There are two main stages to automated particle tracking: locating the spatial coordinates of particles in each frame of the movie, and then linking the coordinates through time into probable trajectories. Typically, tracking algorithms only require a video of particles and a few parameters, such as the apparent particle size and the maximum frame-to-frame particle displacement, as their inputs. As their output, they provide the particle trajectories (Figure 2.1), from which the mean square displacement

(MSD) can be calculated. Here, we describe the tracking algorithm of Crocker and Grier,[2] which has been widely used in fields such as colloid science, microrheology, biophysics, and, more recently, drug and gene delivery. The algorithm was originally implemented in the IDL programming language, but it has since been translated into various other languages, including Python, MATLAB, and C++. Numerous alternative algorithms have been developed for tracking particles, which we discuss later.

In the algorithm of Crocker and Grier, particle coordinates are identified in four steps: 1) preparing the image using common image-processing techniques; 2) finding local maxima of brightness that may correspond to particles; 3) honing in on each candidate particle's exact center with subpixel precision; and 4) discerning which of the candidates are true particles based on their morphology and measured brightness. The foundational paper[2] explains these steps in precise mathematical detail. Here, we will conceptually describe each step in intermediate detail.

The images are prepared using a spatial bandpass filter, which uses a Fourier transform of the image to eliminate all features with small-scale variation (e.g., camera noise) and large-scale variation (e.g., uneven lighting) (Figure 2.2). This effectively erases any objects in the background that are much smaller or much larger than the size of the particles. Next, all local maxima in the processed image are identified. (This is accomplished by taking the union of the image with its own morphological dilation.) If two or more local maxima are separated by a distance smaller than the particle diameter, only the brightest is retained. Then, the intensity-weighted centroid ("center of mass") of each spot is iteratively refined. Finally, the neighborhood surrounding each spot is characterized by its total brightness, size, and eccentricity (deviation from circular shape).

Using these attributes, spots that correspond to actual particles can be distinguished – and the rest discarded – with minimal user input (Figure 2.3). For example, true particles tend to appear bright and circular.

At this point, the x and y locations of particles in each frame are known. Next, the locations must be linked together across frames into particle trajectories. The algorithm robustly handles the complications of real trajectories: Particles are allowed to leave the frame, new particles are allowed to enter, and particles can even be tracked if they temporarily vanish and reappear nearby within a user-specified number of frames. If particles are well separated and moving slowly relative to the frame rate, the task of linking them is simple and unambiguous. If particles are dense and moving quickly, the linking algorithm assigns particles in a way that minimizes the total length of the links. This is grounded in the statistics of random walks; a Brownian particle is most likely to be found right where it was last seen. As the number of particles in view grows, resolving ambiguous networks is difficult. To simplify the problem, the algorithm requires the user to specify the maximum displacement allowed from one frame to the next. For each trajectory, the time-averaged mean squared displacement is calculated as a function of time scale, τ, as $\langle \Delta r^2(\tau) \rangle = \langle [x(t + \tau) - x(t)]^2 \rangle + \langle [y(t + \tau) - y(t)]^2 \rangle$, where the angled brackets denote the average over many starting times t.

To process a set of videos with automated tracking, only a few minutes of user attention are required to input parameters and check that they are suitable. A standard computer will typically be able to process at least one video frame per second, though this depends on the density of particles (and therefore the number of calculations needed for a single frame) in the video, as well as the exact automated tracking algorithm and implementation used. The code will output the trajectories in a text file, spreadsheet, or database. Subsequent data analysis will depend on the scientific question under investigation. We discuss data analysis strategies in Section 3.3.

2.3.2. Sources of error and how to minimize them

Understanding the precision and accuracy of particle localization is critical for conducting reliable particle tracking experiments. In fact, failure to recognize and account for imprecision and inaccuracy in tracking data can lead to misinterpretation.[31,32] Precision refers to uncertainty in location, and is defined as the standard deviation of the measured locations when a single stationary particle is imaged and localized multiple times. In contrast, accuracy describes whether the position estimates deviate from the true particle position with systematic bias.[31,33] There is no limit on localization accuracy, but there is a limit on localization precision.

Tracking resolution (i.e., localization precision) is different than microscope resolution, as classically defined. Microscope resolution is the minimum distance between two distinguishable points. Because of diffraction, the best resolution of a traditional light microscope is approximately half the wavelength of visible light, or roughly 250 nm.[34] However, using an appropriate algorithm, it is possible to localize the center of an isolated particle or point source to better than the diffraction-limited resolution.[30,35] Thus, researchers can routinely track particles with a lateral spatial precision of tens of nanometers or less using a standard light microscope.[29]

Tracking precision is subject to both fundamental and experimental limitations. The fundamental limitation is photon noise: a particle can emit only a finite number of photons during the exposure time, and the number of photons that arrive at a given location on the camera detector in a certain time interval is stochastic, following a Poisson distribution.[36] Consequently, there is statistical uncertainty in locating the particle from its image (Figure 2.4). The size of this uncertainty is inversely proportional to the square root of the number of detected photons.[29,34] Experimental limitations related to detector and specimen properties can also degrade localization precision. Detector pixelation makes it impossible to determine the exact position where a photon arrives within a pixel. Detector noise, including dark current (thermally-induced electrons in the detector) and readout noise (errors in reading the number of photoelectrons built up in a pixel), can also interfere with particle localization.[31,34] Detector noise is greatly reduced in high-performance, cooled, EMCCD cameras. Specimen autofluorescence and out-of-focus background fluorescence can also reduce localization precision and accuracy, which can be an issue when tracking particles in a thick biological specimen using standard epifluorescence illumination. Image processing can remove some, but not all, of this background.[31] Finally, it is important to note that lateral localization precision of fluorescent particles is best for particles located in the focal plane – where the particle image is smallest, brightest, and closest to a Gaussian curve in shape – and decreases with increasing distance from the focal plane.[31,37]

The inability to exactly localize particles, even when they are stationary, is one source of error in particle tracking. This type of error has been referred to as static error, localization error, or random error.[25,29,38] Static error adds a constant offset to the MSD, as derived previously:[25,38] In two dimensions, $MSD_{measured} = MSD_{true} + 4\sigma^2$, where σ is the localization precision. A perfectly immobilized particle will have a true MSD = 0 for all time scales (τ), but because of static error, the actual measured MSD will be a non-zero constant, $MSD = 4\sigma^2$. For pure Brownian motion in two dimensions, the true MSD is $MSD(\tau) = 4D\tau$, but with static error, $MSD(\tau) = 4D\tau + 4\sigma^2$.[25,29] However, in most particle tracking experiments, the true underlying MSD is not known *a priori*, so it may not be immediately evident which component of the measured MSD is "true" and which is artifact.

Additional error is introduced when the particles are moving (Figure 2.4), as is typical in particle tracking experiments. Images cannot be collected instantaneously, and thus require a finite exposure time. If a particle moves substantially during this exposure time, a blurred spot will be recorded, representing the time integral of the particle's location. Particle motion during the exposure time reduces the observed MSD at short times for randomly diffusing particles, as they tend to revisit previously explored regions.[29,39] This effect has been called dynamic error.[38] In addition, particle motion increases static error, because motion blur reduces localization precision by roughly two-fold under typical experimental conditions, as compared to stationary particles.[40]

Static and dynamic error can alter the measured MSD, and can thus introduce inaccuracies when using the MSD to calculate diffusion coefficients and viscoelastic moduli. Static error alone adds a constant offset to the MSD, which flattens the MSD at short time scales on a log-log plot, and makes diffusive motion appear sub-diffusive.[25] Dynamic error, by itself, decreases the MSD at short time scales, which makes diffusive motion appear super-diffusive. Since static and dynamic error act in opposite directions, various scenarios are possible when both errors are present.[38] Depending on which type of error is larger, one effect may dominate, or occasionally, the two effects may largely cancel each other.[38] Both sources of error are more pronounced at short time scales, when the true MSD is smaller.

Prior to beginning a particle tracking experiment, researchers should consider how to minimize errors. Choosing bright particles, a microscope objective with large numerical aperture, and a sensitive camera with low noise will increase signal-to-noise ratio and reduce static error. Choosing image acquisition settings, however, requires a tradeoff between between static and dynamic error (Figure 2.4). Longer exposure time boosts the signal, which, all else being equal, decreases static error. Unfortunately, longer exposure time increases dynamic error as well. The only way to reduce dynamic error is to use an exposure time that is small compared to the frame interval.[29,38] A compromise is to use the longest exposure time possible without introducing large dynamic error. For Brownian motion, an exposure time no longer than one quarter the frame interval will cause dynamic error of <10% at the shortest time scale, and smaller dynamic error at longer time scales.[29]

Dynamic error is difficult to correct after an experiment, because it is time-dependent and also depends on the underlying type of motion, which is often unknown.[41] Static error is simpler to quantify and correct for, since static error adds a constant offset to MSD regardless of the nature of particle motion. Static error can be estimated by tracking particles fixed to a coverslip under signal-to-noise conditions similar to those of the experiment. However, this simple approach may not precisely mimic the background noise in the experiment, nor the effect that motion blur has on static error. An alternative method has recently been proposed for measuring localization precision of moving particles, though this technique requires a custom microscope configuration.[40]

To conclude this discussion, we consider the following question: How much do researchers conducting particle tracking experiments need to worry about static and dynamic error? The answer depends both on the system under investigation and on the desired analysis. If the research objective is to precisely quantify diffusion coefficients or viscoelastic moduli, or to fit the data to a model, it is critical to consider static and dynamic error to ensure proper analysis – especially if the imaging conditions were not ideal. In particular, higher spatial and temporal resolution are needed to accurately study particle motion at short times scales, where the MSD is smaller and the errors proportionally larger. However, if the research objective is to qualitatively compare the transport rates of two types of drug delivery nanoparticles with very different behavior, such as mobile and immobile, moderate errors require less thorough examination and are unlikely to alter the final conclusion.

2.3.3. Assessment of other algorithms for particle localization

Previously, we detailed the widely used automated tracking algorithm of Crocker and Grier. Many other research groups have developed their own tracking algorithms. In a recent competition with 14 entrants, no single algorithm proved to be universally best.[42] Rather, algorithm performance varied depending on characteristics of the experimental system under investigation, such as the type of particle motion, signal-to-noise ratio, and density of particles in the field of view. Therefore, we now outline other select approaches for particle localization and trajectory linking, and discuss their advantages and disadvantages. Regardless of the method chosen, proper algorithm implementation and careful choice of parameters are critical for minimizing error.[42]

There are two main classes of algorithms for locating particle positions in two dimensions: those using model fitting and those not. The model fitting methods fit the particle image to a mathematical model based on the point spread function (PSF). The PSF is the blur pattern formed by diffraction when a point source of light is imaged.[30] Fitting is accomplished by varying the model parameters, including the x and y spatial coordinates, and finding the best fit using a least squares method or maximum likelihood estimation (MLE). The MLE technique can, in theory, approach the best achievable localization precision.[30,36] However, a major limitation is that fitting methods require an estimate of the PSF, and for the MLE approach, of the camera noise as well.[30] The PSF for a point source that is in focus can be modeled by a Gaussian, though this is not exact, especially at the tails. Furthermore, modeling the particle image becomes more complex when the particle is out of focus, or if the particle is too large to be considered a point source, or if the image is asymmetric.[31-33] Another limitation is that fitting methods tend to be computationally intensive and slow.[32]

Particles can also be localized by methods that do not use model fitting. The centroid technique, used by Crocker and Grier, is perhaps the simplest and most widely used non-fitting method. Such algorithms do not require models of the PSF, and thus may be well suited for experimental conditions that distort the PSF, including rapidly moving particles, heterogeneous biological specimens, and imaging in deep in tissue,[30] all of which are common in drug and gene delivery experiments. Indeed, although Gaussian fitting was reported to perform better than the centroid method at localizing immobilized particles, especially at low signal-to-noise ratios,[33] a recent study found that the centroid method is more reliable for moving particles.[40] A different model-independent particle localization method, which was recently developed, localizes the particle using radial symmetry.[32] The radial symmetry method can be envisioned by drawing lines orthogonal to contours of constant intensity in the particle image. The point closest to the intersections of these lines is an estimate of the particle center. This method performed better than the centroid method, and nearly as well as Gaussian fitting using MLE, in one report.[32] In the same study, radial symmetry was 100 times faster (and the centroid method 1,000 times faster) compared to Gaussian fitting.[32] However, we note that radial symmetry is a new technique that should be further studied and tested under additional experimental conditions. Development of new algorithms for localizing particles rapidly and precisely continues to be an active area of research, motivated recently by localization-based super-resolution microscopy techniques such as PALM/STORM, which are based on finding the centers of isolated fluorescent spots.[43-45]

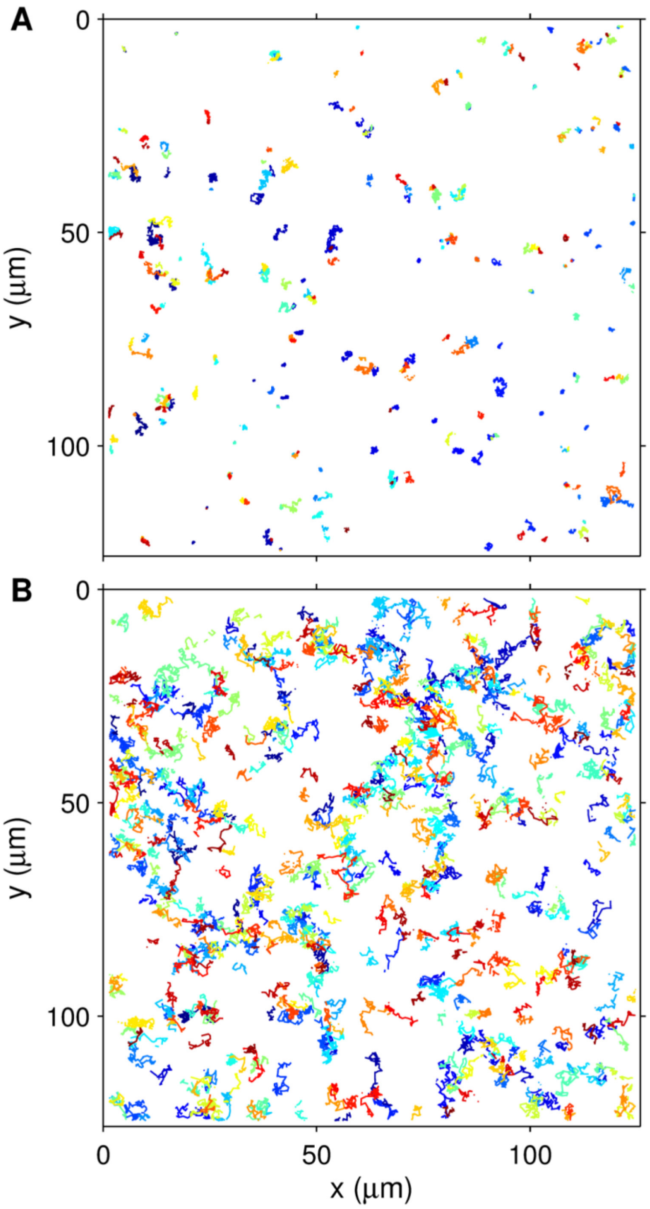

Figure 2.1. Trajectory maps from particle tracking.

(a) 100 nm PS-PEG particles in an inhomogeneous biological specimen, CF sputum, as compared to (b) the same size particles in water. As a visual aid, trajectories are assigned different colors.

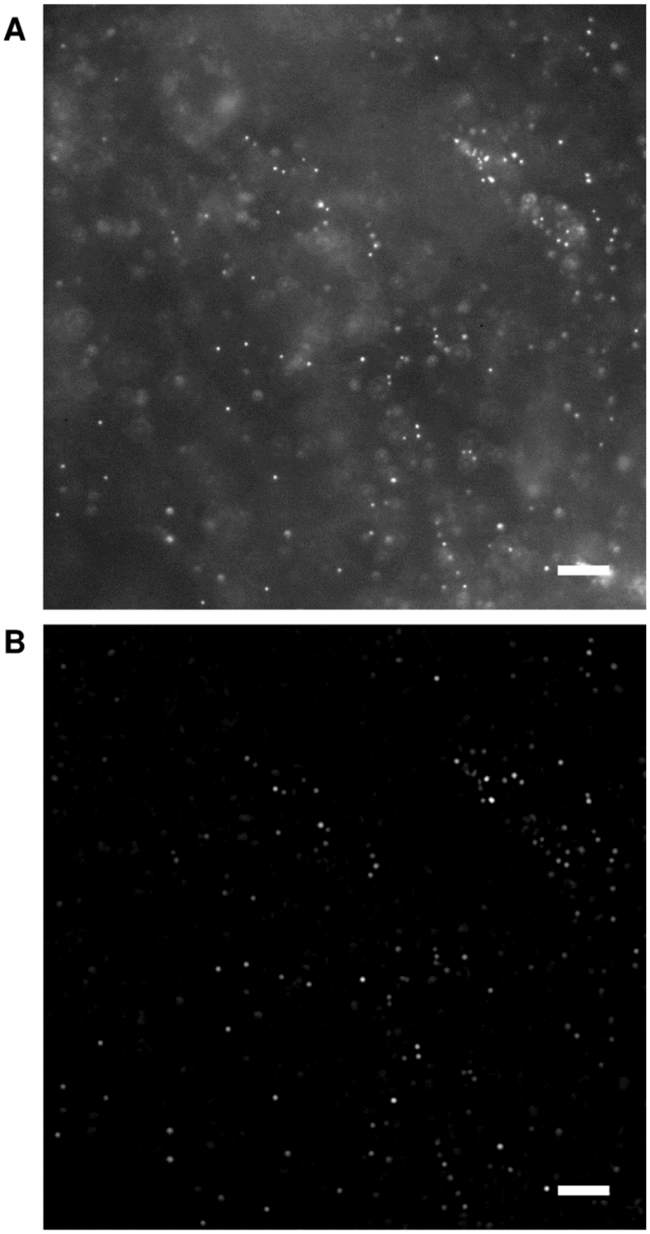

Figure 2.2. Image preparation using a spatial bandpass filter.

The bandpass filter reduces noise and background. Figures show image of 100 nm yellow-green fluorescent polystyrene (PS) particles in a CF sputum sample (A) before and (B) after processing with a bandpass filter. Scale bars represents 10 um.

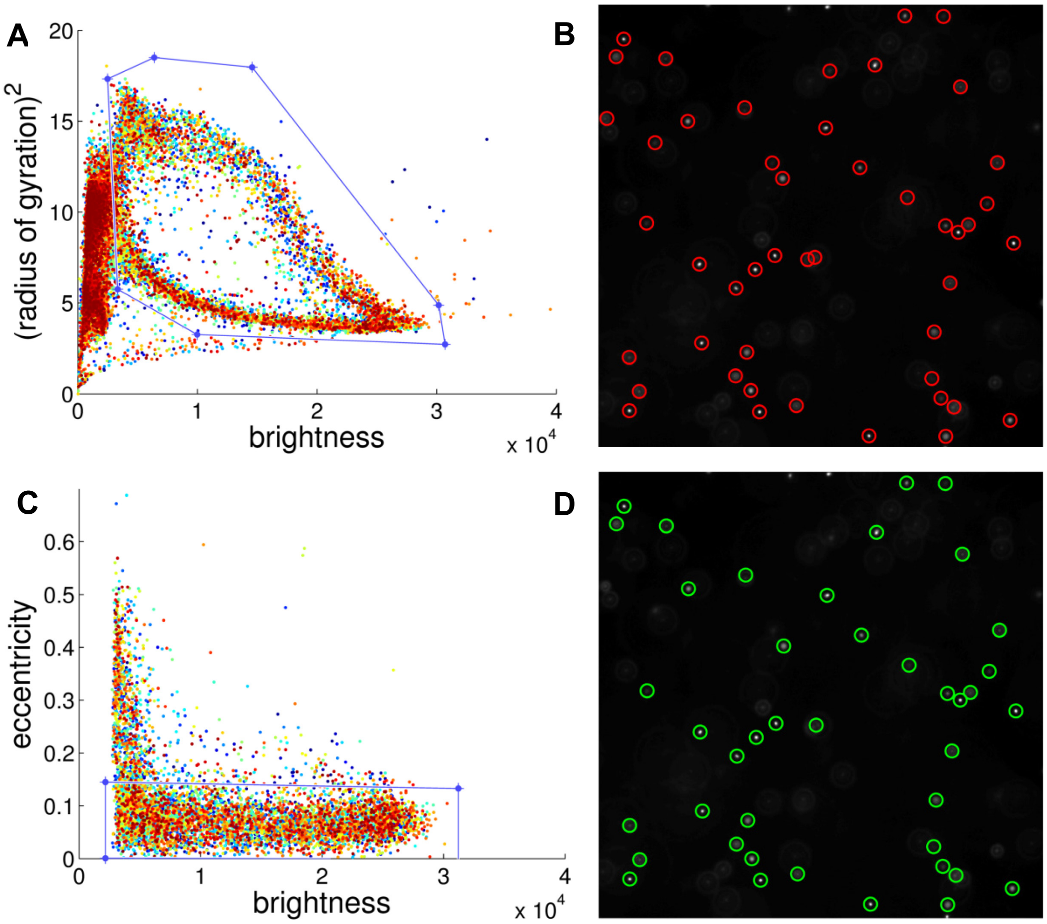

Figure 2.3. Selecting true particles using brightness, size, and eccentricity.

True particles are distinguished from spurious ones based on their brightness, size, and eccentricity. A video of fluorescent 500 nm polystyrene particles diffusing in water, imaged with a 1.46 N.A. oil-immersion objective, was analyzed. For such particles, a plot of particle radius vs. brightness (A) reveals that spurious particles (noise) are dim, whereas true particles are brighter and form a characteristic cluster, which is outlined by the blue polygon. The shape of this cluster is a consequence of the optics. Particles located at the focal plane are the brightest and most compact, while particles above and below the focal plane appear larger and less bright, forming the two prominent curved lines in (A). (B) One frame of the movie, highlighting particles retained after filtering candidate particles based on radius and brightness. The next step is to filter particles based on their eccentricity. (C) A plot of eccentricity (smaller number means more circular in shape) vs. brightness shows that most spots, except the dimmest ones, have eccentricity < 0.2. These are the true particles, and they are selected with the blue rectangle. (D) The particles identified on the same frame of the movie as in (B) after further filtering candidate particles based on eccentricity.

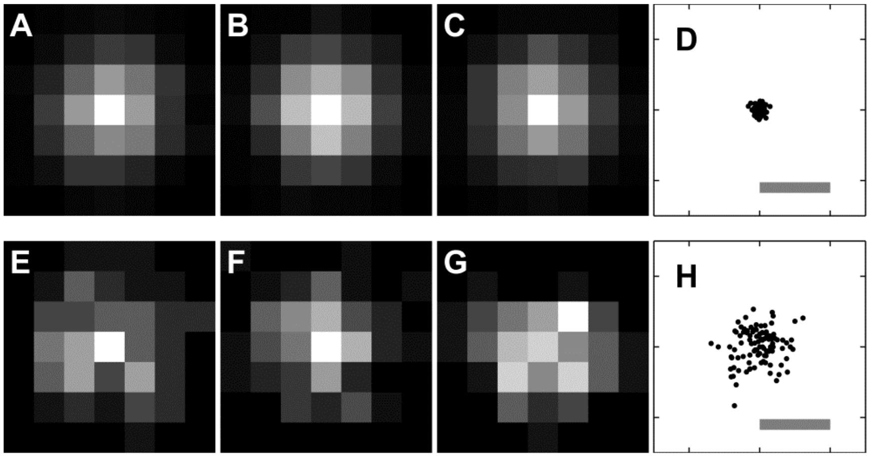

Figure 2.4. Demonstration of localization precision and static error.

(A-C) Three bright particle images (~2,500 photons each). The true particle centers are at the center of each image. The particle images are computer-generated with photon noise, per the method of Thompson (2002), but no camera or background noise. (D) Plot of measured particle centers, calculated from 100 such low-noise images by the centroid method. Scale bar represents half a pixel. (E-G) Three dim particle images (~100 photons each). The true particle centers are at the center of each image. (H) Plot of measured particle centers, calculated from 100 such high-noise images by the centroid method. Scale bar represents half a pixel.

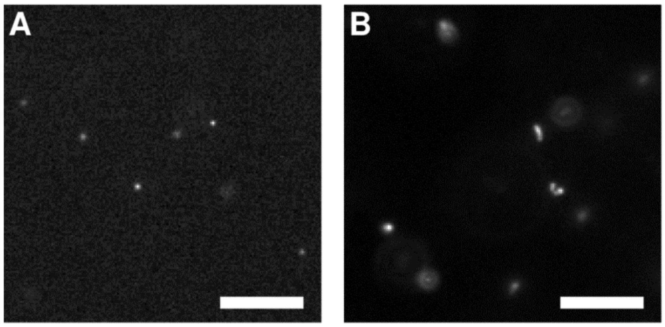

Figure 2.5. Demonstration of the tradeoff between static and dynamic error. Both A and B are images of fluorescent 100 nm particles diffusing in water. In A, the exposure time was 2 ms, while in B, the exposure time was 67 ms; the imaging conditions were otherwise identical. Noise is more pronounced in A compared to B. However, the particle images are compact and circular in A, whereas considerable motion blur is evident in B.

3. NANOPARTICLE DIFFUSION IN RESPIRATORY MUCUS FROM HUMANS WITHOUT LUNG DISEASE[1]

3.1. Introduction

Mucus lines the conducting airways, protecting the respiratory epithelium from the external environment. The respiratory mucus barrier comprises two layers: The gel layer, rich in secreted macromolecules, which is continuously cleared by ciliary beating, and the periciliary layer, consisting of macromolecules tethered to the airway surface, which facilitates ciliary activity.[15] A major role of the respiratory mucus gel is to trap inhaled particles so they can be swept from the airways by mucociliary clearance, thereby defending the lungs against pathogens and toxic materials.[13] However, it is not known what size particles are trapped, or how particle surface chemistry affects mobility, in the airway mucus gel layer of humans without respiratory disease.[46] Airway mucus is difficult to collect and analyze because individuals with healthy respiratory systems generally cannot spontaneously expectorate it, and the mucus gel layer is only a few to a few tens of micrometers thick.[13,47] Yet measuring the permeability of this mucus gel is essential for understanding how effectively it protects the lungs from continuously inhaled pathogens and environmental particulates. Studying the interaction between respiratory mucus and nanoparticles may also elucidate design criteria for inhaled therapeutic nanoparticles to treat diseases such as lung cancer; these particles must penetrate the mucosal barrier to avoid rapid clearance and achieve the pharmacokinetic profile requisite for effective therapeutic outcomes.[48] Finally, characterizing respiratory mucus from humans without pulmonary disease may provide a benchmark against which

---

[1] This chapter appears in Schuster, BS, Suk, JS, Woodworth, GF and Hanes, J (2013). Nanoparticle diffusion in respiratory mucus from humans without lung disease. *Biomaterials* 34: 3439-3446.

to compare respiratory secretions from patients with diseases that affect the airways, including asthma, chronic obstructive pulmonary disease (COPD), and cystic fibrosis (CF).

Nanoparticle diffusion has previously been measured in a variety of human mucus secretions, including cervicovaginal (CV) mucus,[49] CF sputum,[50,51] and chronic rhinosinusitis mucus.[52] Conventional, uncoated polystyrene particles have hydrophobic surfaces that adhere to hydrophobic domains on mucin fibers – the long, entangled glycoproteins responsible for the mucus gel structure.[14] We discovered that coating polystyrene nanoparticles with a dense layer of low molecular weight polyethylene glycol (PEG) minimizes particle adhesion to mucus.[49] PEG minimizes protein adhesion at biomaterial surfaces because the hydrated PEG layer resists release of water molecules and compression.[16] Using PEG-coated particles, we were able to probe the mucus microstructure.[53] We found that PEG-coated particles as large as 200 nm in diameter can penetrate sputum freshly expectorated by CF patients,[50] and PEG-coated particles as large as 500 nm can penetrate CV mucus collected from healthy women,[49] whereas comparably sized uncoated particles are immobilized by the mucus mesh. Tracking the motion of individual PEG-coated and uncoated particles in fresh, minimally diluted mucus samples offers several advantages compared to traditional approaches for studying mucus gel structure and permeability. Electron microscopy, for instance, requires fixation methods that can change the mucus structure.[14] Transport studies using only conventional, uncoated polystyrene particles cannot distinguish between adhesive and steric contributions to particle trapping. Finally, bulk diffusion measurements do not reveal transport rates at the single-particle level, and thus cannot identify particle subpopulations of interest, such as fast-moving outliers.

Mucus secretions from various moist epithelia are similar in overall properties – they are viscoelastic gels comprised of water and mucins, as well as salts, non-mucin proteins, and lipids – but their exact biochemical compositions, clearance rates, and microbiota differ with anatomical site and disease state.[13] These factors alter the mucus microstructure and permeability, and motivate the analysis of mucus from various tissues and conditions. Here, our aim was to study normal human airway mucus, which we define as minimally manipulated airway mucus from individuals without respiratory disease. As a model for normal airway mucus, we collected the mucus from endotracheal tubes of patients without respiratory comorbidities who underwent elective, non-cardiothoracic surgery, as previously described.[54] This collection method is noteworthy because it imposes no additional burden on the patient, and in contrast to bronchiolar lavage or to sputum induction using nebulized hypertonic saline, it minimizes sample dilution and salivary contamination.[54,55] We performed scanning electron microscopy to visualize the mucus samples and conducted biochemical assays to analyze their basic composition. To elucidate the physicochemical properties of nanoparticles that govern their transport rates in normal airway mucus, we measured the mobility of PEG-coated and uncoated 100, 200, and 500 nm polystyrene particles in fresh mucus samples using high-resolution fluorescence microscopy and multiple-particle tracking analysis. We further investigated the mucus gel structure and the barrier it poses to nanoparticle diffusion by comparing the bulk rheological properties of respiratory mucus, as measured using a cone-and-plate rheometer, with the microrheological properties, as probed by PEG-coated nanoparticles.

3.2. Methods

3.2.1. Mucus sample collection

Human airway mucus samples were collected in accordance with a protocol approved by the Johns Hopkins Medicine Institutional Review Board (study number NA_00038606). Samples were collected by the endotracheal (ET) tube method, as previously described.[54,56] Patients who required intubation as part of general anesthesia for elective, non-cardiothoracic surgery at the Johns Hopkins Hospital were identified. Only patients with no cardiopulmonary or respiratory comorbidities and no smoking history were included in this study. At the end of surgery, the ET tube was removed from the patient, and the distal 10 cm portion, including the balloon cuff, was cut and placed in a 50 mL centrifuge tube. The specimens were then spun at 1000 rpm (220 × g) for 30 s, yielding an average mucus volume of 0.5 mL. Mucus with visible blood contamination was not included in the analysis. Mucus samples were stored at 4 °C and analyzed within 24 hours of collection, excluding portions for the mucin and DNA assays, which were frozen at -20 °C until use. The results presented here are from male and female patients; the mean patient age was 56 years, with standard deviation 17 years.

3.2.2. Rheology of respiratory mucus

Bulk rheological properties of airway mucus were measured using a strain-controlled rheometer (RFS3; TA Instruments) with cone-and-plate geometry (cone diameter 25 mm and angle 0.1 rad). All measurements were conducted at room temperature in a humidified chamber. Oscillatory tests, performed at small strain amplitudes to minimize shear damage to the mucus samples, were used to measure the frequency-dependent elastic modulus, $G'(\omega)$, and viscous modulus, $G''(\omega)$, of the mucus.[57] (The elastic and viscous moduli, respectively, are the in-phase and out-of-phase components of stress induced in the material, divided by the magnitude of the applied strain.) After the mucus sample was loaded onto the rheometer, it was allowed to equilibrate for five minutes. Then, the linear viscoelastic region, for which the viscous and elastic moduli are independent of strain amplitude,[58] was determined by conducting strain amplitude sweeps from 0.2 to 10% strain at frequencies of 1, 6.28, and 100 rad/s. Based on the strain sweep tests, 1% strain was determined to be within the linear viscoelastic region, and was thus used for the frequency sweep test (from 0.1 to 100 rad/s).

3.2.3. Determination of mucin, DNA, and total solids content

Mucin concentration was determined based on the reaction of 2-cyanoacetamide (Sigma-Aldrich) with O-linked glycoproteins, as previously described.[51,59] Mucus aliquots were diluted 20-fold and homogenized by vortexing for at least 15 min. Then, 50 μL of this suspension was mixed with 60 μL of an alkaline solution of 2-cyanoacetamide (200 μL of 0.6 M 2-cyanoacetamide added to 1 mL of 0.15 M NaOH). The mixture was incubated at 100 °C for 30 min, after which 0.5 mL of 0.6 M borate buffer, pH 8.0, was added to it. Fluorescence intensity was measured at excitation and emission wavelengths of 340 and 420 nm, respectively. Mucin concentrations were calculated by comparing the fluorescence intensity readings to a standard curve generated using known concentrations of mucin from bovine submaxillary gland (Sigma-Aldrich).

A fluorimetric assay was also used to measure DNA concentration, based on the reaction of 3,5-diaminobenzoic acid dihydrochloride (DABA; Sigma-Aldrich) with DNA.[51] Mucus aliquots were diluted 5-fold and homogenized by vortexing for at least 15 min. Then, 30 μL of this suspension was reacted with 30 μL of 20% wt/vol DABA solution. After incubating for 1 h at 60 °C, 1 mL of 1.75 M HCl was then added to stop the reaction. The fluorescence was measured at excitation and emission wavelengths of 400 and 520 nm, respectively. DNA concentrations were calculated with reference to a standard curve generated using known concentrations of DNA from salmon testes (Sigma-Aldrich).

The total solids content of mucus was determined by freeze-drying. Mucus samples were frozen in liquid N_2 and placed in a lyophilizer (FreeZone 4.5 Plus; Labconco) for at least 12 h to extract water from the samples. The ratio of mucus mass before versus after lyophilization is the total solids content.

3.2.4. Scanning electron microscopy

Respiratory mucus samples were prepared for scanning electron microscopy (SEM) based on a protocol previously used for CV mucus and CF sputum.[51,60] Mucus samples were fixed for 1 h in 2% glutaraldehyde in 100 mM sodium cacodylate buffer, pH 7.2, containing 3 mM $CaCl_2$. The samples were then rinsed in buffer and postfixed in 1% OsO_4 in 100 mM sodium cacodylate buffer for 1 h on ice in the dark. Following a brief rinse with distilled water, samples were stained with 2% uranyl acetate for 1 h and then dehydrated through a graded series of ethanol solutions. Upon complete dehydration, samples were soaked in a 50:50 mixture of ethanol and hexamethyldisilazane (HMDS), followed by pure HMDS. Mucus samples were then dessicated under vacuum overnight. The samples were attached to aluminum stub mounts via carbon adhesive tabs (Ted Pella), and then coated with 20 nm of AuPd with a sputter coater (Desk III; Denton Vacuum). The samples were imaged with a field-emission scanning electron microscope (LEO 1530 FESEM; Zeiss) operating at 1 kV.

3.2.5. Nanoparticle preparation and characterization

Fluorescent, carboxylate-modified polystyrene spheres (PS-COOH) sized 100, 200, and 500 nm in diameter were purchased from Molecular Probes. The surface density of carboxyl groups on the particles, calculated using data provided by the manufacturer, ranged from 3 to 8 COOH/nm^2 depending on the lot. PEG-coated particles were prepared by covalently modifying the PS-COOH particles with 5 kDa methoxy-PEG-amine (Creative PEGWorks) using carbodiimide coupling chemistry.[18] Briefly, 100 µL of PS-COOH particle suspension, supplied by the manufacturer as 2% solids, were washed and resuspended to 4-fold dilution in ultrapure water in a 1.5 mL microcentrifuge tube. PEG was added to the particle suspension in excess (2-fold excess for the 100 nm particles and 5-fold excess for the 200 and 500 nm particles), based on the number of carboxyl groups on the particles. After mixing to dissolve the PEG, N-hydroxysulfosuccinimide sodium salt (sulfo-NHS; Sigma-Aldrich) was added to the tube, followed by 600 uL of 200 mM borate buffer, pH 8.2, and 1-ethyl-3-(3-dimethylaminopropyl) carbodiimide hydrochloride (EDC; Invitrogen). NHS and EDC concentrations were 10 mM and 6 mM, respectively. Particles suspensions were placed on a tube rotator for 4 hours, then centrifuged and washed with ultrapure water. Particles were resuspended in ultrapure water to the original concentration. Aliquots for particle transport experiments were diluted with ultrapure water to obtain concentrations appropriate for tracking individual particles. Particle suspensions were stored at 4 °C until use.

The surface density of PEG on PS-PEG particles prepared according to this protocol was recently measured to be 0.09 PEG/nm^2, using a nuclear magnetic resonance (NMR) method, as reported by our lab.[18] Particle size and zeta-potential were measured by dynamic light scattering and laser Doppler anemometry, respectively, using a Zetasizer Nano ZS90 (Malvern Instruments), which has a 90° scattering angle. Both size and zeta-potential were measured at 25 °C, with the particles suspended in phosphate buffered 10 mM NaCl solution, pH 7.4.

3.2.6. Multiple particle tracking in respiratory mucus

Nanoparticle transport in airway mucus was studied by multiple particle tracking (MPT). The particle suspensions were added to mucus samples at a final dilution of 4% vol/vol in custom-made microscopy chambers. After gently stirring the samples, the chambers were sealed to prevent sample dehydration, then incubated for 1.5 h. Particle motion in the mucus samples was observed at room temperature using an inverted epifluorescence microscope (Axio Observer; Zeiss) with a 100x/1.46 NA oil-immersion objective. Movies were collected for 20 s at a temporal resolution of 67 ms using an EMCCD camera (Evolve 512; Photometrics). Movies were analyzed with MetaMorph software (Molecular Devices) to extract the x and y positions of particle centroids over time. At least 100 PS-COOH and PS-PEG particles of each size were tracked for at least 50 frames in each of five mucus samples. For each trajectory, the time-averaged mean squared displacement (MSD) was calculated as a function of time scale, τ, as $\langle \Delta r^2(\tau) \rangle = \langle [x(t+\tau) - x(t)]^2 \rangle + \langle [y(t+\tau) - y(t)]^2 \rangle$. The tracking resolution, determined by tracking particles immobilized to glass with a strong adhesive,[61] was determined to be 10 nm (substantially smaller than the diameter of the particles). Based on the SEM images, airway mucus may be assumed to be isotropic (though not homogeneous), so the 2-dimensional MSD measured here by MPT equals two-thirds of the 3-dimensional MSD. The ensemble-averaged MSD (⟨MSD⟩) for all particles of a given type in a given mucus sample was calculated by taking the geometric mean of the individual particles' time-averaged MSDs. We fit the ⟨MSD⟩ data to the equation $\langle \mathrm{MSD} \rangle = k\tau^{\alpha}$ to obtain α, which is a measure of the extent of impediment to particle diffusion ($\alpha = 1$ for pure Brownian motion and $\alpha < 1$ for subdiffusion). This was accomplished by calculating the slope of $\log(\langle \mathrm{MSD} \rangle)$ vs. $\log(\tau)$ using the least-squares method. Additional information on MPT measurements is available in review articles.[61,62]

3.2.7. Particle tracking microrheology analysis

Particle tracking microrheology analysis was performed by applying the generalized Stokes-Einstein relation (GSER) to the PS-PEG particle MSD data. The GSER relates the thermal motion of particles to the viscoelastic moduli of the material environment they probe. The unilateral Laplace transform of the MSD, $\langle \Delta \tilde{r}^2(s) \rangle$, is related to the viscoelastic spectrum of the material, $\tilde{G}(s)$, according to the GSER by $\tilde{G}(s) = 2k_B T / [3\pi a s \, \langle \Delta \tilde{r}^2(s) \rangle]$. Here, k_B is Boltzmann's constant, T is the absolute temperature, a is the particle radius, and s is the complex Laplace frequency. This can be used to find the complex modulus, $G^*(\omega) = G'(\omega) + iG''(\omega)$, as detailed elsewhere.[63,64] In this way, the displacements of the particles can be used to calculate the microscopic viscoelasticity of the environment they probe. The viscoelastic response can alternatively[65] be interpreted as a complex viscosity, $\eta^*(\omega)$, whose magnitude is defined as $|\eta^*(\omega)| = |G^*(\omega)|/\omega$. Complex viscosity thus incorporates both viscous and elastic contributions. In the limiting case, for a purely viscous Newtonian liquid such as water, the complex viscosity equals the standard steady shear viscosity.

3.2.8. Viscosity of mucus interstitial fluid

The viscosity of mucus interstitial fluid was determined by centrifuging mucus samples for 1 h at 21,000 × g, removing the supernatant, and then measuring the supernatant viscosity by particle tracking microrheology (we confirmed that these supernatant viscosity measurements did not depend on probe particle size).

3.2.9. Statistical analysis

Statistical analysis (for Figure 3.6) was performed by one-way analysis of variance (ANOVA) using logarithmically transformed data. Subsequent multiple comparison tests were performed using Tukey's HSD procedure. Analysis was conducted using the Statistics Toolbox in MATLAB R2012a (MathWorks). Differences were considered to be statistically significant at a level of $P < 0.01$.

3.3. Results

3.3.1. Bulk rheology

To characterize the bulk material properties of respiratory mucus, we measured the viscoelastic moduli of mucus samples (n = 5) using a cone-and-plate rheometer. We determined from strain sweep tests that 1% strain is within the linear viscoelastic region (Figure 3.1A). We then measured the frequency-dependent viscoelastic moduli at 1% strain and found that the elastic modulus, $G'(\omega)$, exceeded the viscous modulus, $G''(\omega)$, over the 3 decades of frequency tested (Figure 3.1B). A frequency of $\omega = 1$ rad/s is traditionally used in mucus rheology studies to approximate the low shear rates of mucociliary clearance [66,67]. The ratio of the viscous to elastic modulus, $\tan(\delta) = G''(\omega)/G'(\omega)$, was 0.30 at $\omega = 1$ rad/s; this corresponds to a phase angle of $\delta = 17°$. Materials with $0 < G''/G' < 1$, or equivalently $0° < \delta < 45°$, are categorized as viscoelastic solids. The viscous and elastic moduli exhibit a weak frequency dependence, with $\log(G')$ and $\log(G'')$ both having slopes around 0.15 when plotted against $\log(\omega)$. Overall, this rheological signature is characteristic of a crosslinked gel, as expected.[67]

3.3.2. Biochemical analysis

To assess mucus sample quality and composition, we conducted basic biochemical analysis. The total solids content of airway mucus was 6.9 ± 2.8% (n = 13). The measured mucin content ranged from 8 to 22% of the total solids, corresponding to a mucin content of 0.6 to 1.4 %, while DNA comprised less than 1% of the total solids on average. The pH of the mucus samples ranged from 7 to 8.5.

3.3.3. Microstructure of respiratory mucus

We imaged airway mucus using scanning electron microscopy, which visually confirmed that the mucus samples have a meshwork architecture (Figure 3.2). In the SEM images, pores in the mucus mesh ranged from tens to hundreds of nm in diameter, with many pores smaller than 100 nm; we note, however, that SEM sample preparation likely contracts the mucus microstructure.[14] The fibers appeared to be randomly oriented, which suggests that the mucus samples are isotropic. The SEM images of normal airway mucus were similar in overall appearance to previously published images of CF sputum.[51,68]

3.3.4. Transport of particles in respiratory mucus

We compared the thermally-driven motion of PEG-coated polystyrene nanoparticles (PS-PEG) to that of conventional carboxylate-modified PS nanoparticles (PS-COOH) in fresh human respiratory mucus using multiple-particle tracking (MPT). The dense PEG layer on the PS-PEG particles was confirmed by their near-neutral surface charge, compared to the highly negative surface charge of the PS-COOH particles (Table 3.1). We have also recently quantified the PEG density using an NMR-based method.[18] The 100 nm diameter PS-COOH particles exhibited hindered trajectories in airway mucus, and the 200 and 500 nm PS-COOH particles were essentially immobilized (Figure 3.3A, C and E). In contrast, the 100 and 200 nm PS-PEG particle trajectories were more diffusive (Figure 3.3B and D). The 500 nm PS-PEG particles exhibited constrained traces (Figure 3.3F) indistinguishable from those of the 500 nm PS-COOH particles.

To quantify these differences, we calculated the mean squared displacements (MSDs) of at least 100 individual particles of each particle type in each mucus sample (n = 5). At a time scale (τ) of 1 s, the geometric ensemble-averaged MSD ($\langle MSD \rangle$) of 100 and 200 nm PS-PEG particles was 14-fold and 33-fold greater, respectively, compared to the 100 nm and 200 nm PS-COOH particles (Figure 3.4). However, the $\langle MSD \rangle$ of the 500 nm PS-PEG particles was similar to that of the 500 nm PS-COOH particles for all time scales. At a time scale of 1 s, the 100 and 200 nm PS-PEG particles were slowed only 26- and 41-fold, respectively, compared to their theoretical diffusivities in water, as calculated with the Stokes-Einstein equation. In contrast, the 100 and 200 nm uncoated particles were slowed 390- and 1600-fold, respectively, compared to their theoretical diffusivities in water. The 500 nm particles, both PS-COOH and PS-PEG, were slowed more than 500-fold compared to their theoretical diffusivities in water (Table 3.1).

To further assess the extent to which normal airway mucus hinders particle motion, we fit the ensemble-averaged MSDs to $\langle MSD \rangle = k\tau^{\alpha}$ and extracted α, the anomalous diffusion exponent. For pure Brownian motion in a viscous liquid, $\alpha = 1$; for anomalous subdiffusion in complex environments over short time scales, $\alpha < 1$, with smaller α indicating more hindered particle motion.[62] The value of α for 100 and 200 nm PS-PEG particles was 0.88 and 0.82, respectively, while for the 100 and 200 nm PS-COOH particles, it was 0.68 and 0.54, respectively (Table 3.1). The α values were only 0.59 and 0.54 for 500 nm PS-PEG and PS-COOH particles, respectively.

Fast-moving particles are of particular interest, as they are more likely to penetrate the heterogeneous mucus layer quickly enough to reduce their removal by mucociliary clearance and approach the underlying epithelium. In addition to ensemble-averaged transport rates, MPT also provides individual particle data, which can be represented in a histogram of individual particle MSDs (Figure 3.5; these results are presented at $\tau = 3$ s to facilitate comparison with the 3 s long trajectories in Figure 3.3). Particles with MSDs less than 0.1 μm^2 at a time scale of 3 s appeared immmobile in our time-lapse videos. (We note that longer tracking videos would be valuable to confirm that these particles are immobile over timescales well beyond 3 s.) The MSD value of 0.1 μm^2 at $\tau = 3$ s is approximately 500-fold lower than that of a 100 nm particle diffusing in water. If we define particles below this cutoff as immobile and above it as mobile, we find 84%, 75%, and 8% of 100, 200, and 500 nm PS-PEG particles, respectively, were mobile. The 100 nm PS-COOH particles did have a sizable mobile fraction by the above definition, over 42%, whereas only 11% of 200 nm and 5% of 500 nm PS-COOH particles were mobile.

3.3.5. Micro- vs. macroscopic rheology

To deepen our understanding of the mucus gel structure and the barrier it poses to different sizes of PEG-coated particles, we compared the macroscopic (bulk) rheological properties of respiratory mucus, as measured using a cone-and-plate rheometer, with the microscopic rheological properties, as measured by particle tracking microrheology (PTM). To facilitate this comparison, the values we report here are $|\eta^*(\omega)|$, the magnitude of the complex viscosity, at $\omega = 1$ rad/s. At the bulk level, respiratory mucus had a complex viscosity magnitude more than 13,000 times that of water. In contrast, the measured viscosity of mucus interstitial fluid was approximately 3 times that of water (Figure 3.6), in good agreement with a previous study on CF sputum.[69] The 100 and 200 nm PS-PEG particles experienced viscosities only 16- and 38-fold higher than that of the mucus interstitial fluid, respectively, and more than 250- and 100-fold lower than the bulk viscosity (Figure 3.6). In contrast, the 500 nm PS-PEG particles experienced an average viscosity more than 1000 times greater than that of the mucus interstitial fluid, and only 4-fold lower than the bulk viscosity of mucus.

3.4. Discussion

In this study, we explored the barrier properties of human respiratory mucus collected from individuals without lung disease. We found that polymeric nanoparticles as large as 200 nm, if densely coated with low molecular weight PEG, can rapidly diffuse through respiratory mucus. This finding will help guide the design of inhaled therapeutic nanoparticles – including drug, gene, and vaccine carriers – which offer the potential for increased efficacy and reduced side effects compared to traditional approaches for treating and preventing respiratory disease. To be maximally effective, inhaled chemotherapy-loaded nanoparticles for lung cancer[70] and nanoparticle-based vaccines for tuberculosis and influenza[71,72] may need to achieve broad coverage throughout the airways and avoid rapid clearance by the mucociliary escalator.[48] We recently reported that mucus-penetrating nanoparticle formulations can improve the distribution, retention, and efficacy of vaginally administered drugs.[19] Likewise, particles that can rapidly penetrate airway mucus may achieve reduced clearance and improved airway distribution, retention, and pharmacokinetic profile. The present work also enhances understanding of the barrier properties of airway mucus to inhaled environmental particles, such as viruses and particulate matter pollution, both of which are major global health risks.[73]

The findings in this study suggest that airway mucus is a selectively permeable barrier, whose barrier properties depend upon both particle size and adhesiveness. Small, PEG-coated particles exhibit enhanced transport in airway mucus compared to similarly sized uncoated particles because the dense PEG coating reduces particle adhesion to the mucus network, permitting the particles to diffuse more freely.[49,50,53] The low viscosities experienced by 100 and 200 nm PEG-coated particles indicate that these particles resist muco-adhesion and furthermore are small enough to diffuse through fluid-filled openings in the mucus network, so they are less sensitive to the bulk rheological properties of the mucus. To these particles, on average, the mucus barrier is a low-viscosity liquid. In contrast, the 500 nm particles, even with PEG coatings, experience significantly larger viscosities, approaching the mucus bulk viscosity. This is most likely because their large size relative to the mucus mesh size precludes the particles from readily percolating through the mucus gel. Particles that are large relative to the mucus mesh spacing, similarly to particles that firmly adhere to mucus, are sensitive to the elasticity of the biopolymer network and its solid-like bulk rheology.

Our finding that PEG-coated particles as large as 200 nm in diameter can diffuse in respiratory mucus appears to conflict with our visual analysis of SEM images, in which the majority of pores appeared to be smaller than 100 nm. As previously documented, this discrepancy is likely caused by alteration of the mucus network during SEM sample preparation, which entails fixation and dehydration of the mucus; quick freezing is an alternative approach, but may induce artifacts also.[14] Furthermore, polymers in solutions and gels like mucus are dynamic, which a static SEM image cannot show.[14,74] Because of this dynamic nature, a non-adhesive particle whose diameter is comparable to the average mesh size may be able to percolate through the mucus,[74,75] which might not be evident from SEM image analysis. Particle tracking allowed us to overcome these challenges and probe the microstructure of fresh, minimally perturbed airway mucus samples.

To effectively shield against adhesive hydrophobic and electrostatic interactions and minimize protein binding, PEG must be densely grafted to the particle surface. PEG tends to adopt an extended "brush" conformation if the surface density is sufficiently high that the distance between grafted PEG chains is smaller than their Flory radius (the unconstrained polymer size in a good solvent).[76,77] In contrast, the PEG adopts a "mushroom" conformation when PEG density is lower, such that adjacent chains are far enough apart to generally avoid overlap. An unconstrained 5 kDa PEG chain has a Flory radius of ~6 nm.[18] We recently reported that our 100 nm PS-PEG particles with near-neutral zeta-potential had approximately 0.09 PEG chains per nm^2 of particle surface, or one chain per ~11 nm^2; this corresponds to ~3.3 nm between the attachment point of neighboring PEG chains, which is within the brush regime for 5 kDa PEG.[18] Dense PEG brush coatings have been shown to better shield nanoparticles against interactions with biomolecules.[76]

While we found that PEG-coated particles as large as 200 nm in diameter can diffuse in respiratory mucus gel, we note that *in vivo*, the mucus gel layer sits atop the periciliary layer (PCL), which is expected to serve as a further barrier to particles. Recent evidence suggests that the PCL is not a watery liquid, as previously thought, but rather consists of a dense brush of macromolecules grafted to cilia and the epithelial surface.[15] In primary human bronchial epithelial (HBE) cell cultures, the periciliary brush has a maximum mesh size of approximately 40 nm.[15] This may provide an extra layer of protection to the airway epithelia, beyond that of the mucus gel studied here, in airway regions with an intact PCL. There may be gaps in the PCL above secretory cells,[78] so particles might be able to more readily breach the lung's protective barrier at those locations. We must also emphasize that in healthy individuals, ciliary beating constantly propels mucus out of the lungs, while continuous mucin secretion simultaneously replenishes the mucus gel layer.[13] To reach the PCL, a nanoparticle must therefore diffuse through the mucus gel layer faster than it is swept away by mucociliary activity.

We recognize that mucus collected by the endotracheal tube method may be altered compared to the mucus gel layer *in vivo*. When the patients were in the operating room, their endotracheal tubes were connected to a passive heat and moisture exchanger (Humid-Vent) to humidify the ventilated air. Still, the ventilated air may be drier than air humidified by passing through the upper respiratory tract during normal respiration. Endotracheal tube mucus could thus be dehydrated compared to mucus *in vivo*.[54] If so, the work here would set a conservative bound on the nanoparticle size capable of penetrating respiratory mucus. However, our rheological and biochemical data suggest that the endotracheal tube mucus samples were of good quality. First, in terms of rheology, we measured $\tan(\delta) = 0.30$ at ω = 1 rad/s; this is in close agreement with previously published values for respiratory mucus collected by the endotracheal tube method (0.33) and by a bronchoscopy brush method (0.28) from individuals with no respiratory disease.[54,56] Second, in terms of total solids content, we measured an average of 6.9% solids. This is in reasonable agreement with the 5.2% solids reported by Matthews et al. for "normal" mucus, which they collected from laryngectomized patients.[79] Other papers report that normal mucus is 2 to 3% solids, but those values are based on mucus collected from HBE cell cultures.[15,47] Third, with regards to biochemical composition, we measured mucin contents ranging from 8 to 22% of the total solids, which is consistent with reports that mucins account for less than 30% of the mucus solids.[13] We found that DNA was less than 1% of the total solids on average, as expected for healthy respiratory mucus, and in contrast to the elevated (approximately10-fold higher) DNA concentration in CF sputum, for instance.[13,51,79]

Previously, we characterized sputum expectorated by adult CF patients.[50] Comparing that work with the present study, PEG-coated 200 nm particles were slowed 65-fold in CF sputum and 41-fold in normal airway mucus at a timescale of 1 s, compared to their theoretical diffusivities in water. This difference may be due to the increased concentrations of DNA, actin, and other debris released by dead inflammatory cells in CF sputum.[13] In both normal mucus and CF sputum, 500 nm particles were immobilized. Although the collection methods are different, making direct comparison challenging, this finding implies that both normal and CF mucus are significant barriers to nanoparticle transport. We note that in our previous work with CF sputum, 100 nm PS-PEG particles were immobilized, which we attributed to difficulty coating these smaller, more highly curved particles with a dense PEG layer.[50] However, we have since engineered improved 100 nm particles with denser PEG coatings, as discussed.[18,49,53] We show here that these improved 100 nm PS-PEG particles can penetrate normal airway mucus, and they are also capable of penetrating CF sputum (to be published). Thus, the difference in transport of 100 nm PS-PEG particles between our previous CF paper and the present work with normal airway mucus reflects the quality of the PEG coating, not the disease state.

We found that there are profound differences between respiratory mucus and mucus collected from the female reproductive tract.[49,53] Whereas 500 nm PS-PEG particles are immobilized in airway mucus, they can effectively penetrate cervicovaginal mucus (CVM) from healthy women. This indicates that the airway mucus collected here has a significantly tighter mesh than does CVM. This may reflect the greater need for particle trapping in the airways, which are continuously exposed to the external environment. Despite its larger mesh spacing, CVM's bulk viscous and elastic moduli are roughly one order of magnitude greater than those of airway mucus.[80] This may be explained as follows: Mucins in native CVM are bundled by hydrophobic interactions,[80] and may be more bundled than are mucins in airway mucus. Increased mucin bundling in CVM would produce thicker mucin fibers, resulting in larger viscoelastic moduli and a more porous microstructure, of CVM compared to airway mucus. This finding agrees with experiments using a model actin gel, where it was found that for a fixed actin concentration, increased actin fiber bundling caused both increased mesh size and increased elastic modulus.[81] To further understand how mucus differs between different anatomical locations, the techniques used here could also be applied to characterize the rheology and permeability of mucus from other mucosal tissues, such as the GI tract.

Another difference we found in this study was that approximately 40% of 100 nm PS-COOH particles are mobile in respiratory mucus, whereas 100 nm PS-COOH particles are almost entirely immobilized in CVM.[49] This suggests that particles with hydrophobic and anionic surface regions, such as PS-COOH particles, may be less adhesive to respiratory mucus than they are to CVM. It is possible that abundant endogenous surfactants in airway mucus[82,83] may coat hydrophobic regions on mucins or on the particles, making the PS-COOH particles less adhesive to respiratory mucus. The consequences of this phenomenon on particle transport are more noticeable for smaller particles, most likely because smaller particles are less likely to form multiple contacts with the mucus gel network, and thus are less avidly adhered. One finding supporting this explanation is that, compared to untreated CF sputum, 200 nm PS-COOH particles and adhesive rod-shaped gene vectors exhibit enhanced transport in sputum treated with N-acetyl cysteine, which increases the pore size by cleaving disulfide crosslinks in the mucin mesh.[68,84] The 100 nm PS-COOH particle transport data suggests that viruses and very small environmental pollution particles that deposit in the airways may be capable of penetrating the airway mucus gel layer to some extent, increasing the threat they pose to the body. For instance, our results suggest that the influenza virus ($d \approx 100$ nm, smaller than the mucus mesh size) should be able to penetrate respiratory mucus, unless it is strongly immobilized by adhesive interactions with mucus constituents.

3.5. Conclusion

Using multiple particle tracking of non-muco-adhesive probes, we determined the microstructure of respiratory mucus collected from endotracheal tubes of humans without lung disease. We found that PEG-coated particles as large as 200 nm are capable of penetrating normal human airway mucus. Whereas respiratory mucus is a viscoelastic solid at the bulk level, small PS-PEG particles ≤ 200 nm can penetrate the mucus as if it were primarily a viscous liquid. We also established principles and methods that can be applied to design and test novel therapeutic mucus-penetrating nanoparticles for airway delivery, as well as to study the transport of respiratory viruses and environmental nanoparticles in physiologically relevant mucus samples.

Table 3.1. Particle characterization and transport summary.

Particle size[a], nm	Material	Diameter[b], nm	ζ-potential[c], mV	$D_w/\langle D_{eff}\rangle$[d]	α[e]
100	PS-COOH	92 ± 3	-50 ± 3	390	0.68
100	PS-PEG	99 ± 1	-1 ± 1	26	0.88
200	PS-COOH	188 ± 1	-54 ± 4	1600	0.54
200	PS-PEG	219 ± 3	-5 ± 1	41	0.82
500	PS-COOH	508 ± 2	-73 ± 3	980	0.54
500	PS-PEG	549 ± 6	-3 ± 1	590	0.59

[a] Provided by the manufacturer.

[b] Measured by dynamic light scattering. Error values represent standard deviation of 3 measurements.

[c] Measured in 10 mM NaCl at pH 7.4. Error values represent standard deviation of 3 measurements.

[d] D_w is the diffusivity of particles in water, as calculated from the Stokes–Einstein equation. $\langle D_{eff}\rangle$ is the effective diffusivity of particles in mucus measured at a time scale of 1 s, and it is calculated as $\langle D_{eff}\rangle = \langle MSD(\tau)\rangle/4\tau$ with $\tau = 1$ s. The ratio $D_w/\langle D_{eff}\rangle$ indicates the average factor by which the transport of particles in mucus is slowed compared to in water.

[e] Calculated by fitting $\langle MSD(\tau)\rangle$ to $\langle MSD(\tau)\rangle = k\tau^{\alpha}$ for τ between 0.2 and 3.2 s. For anomalous diffusion, $0 < \alpha < 1$. Smaller values of α indicate more hindered particle motion.

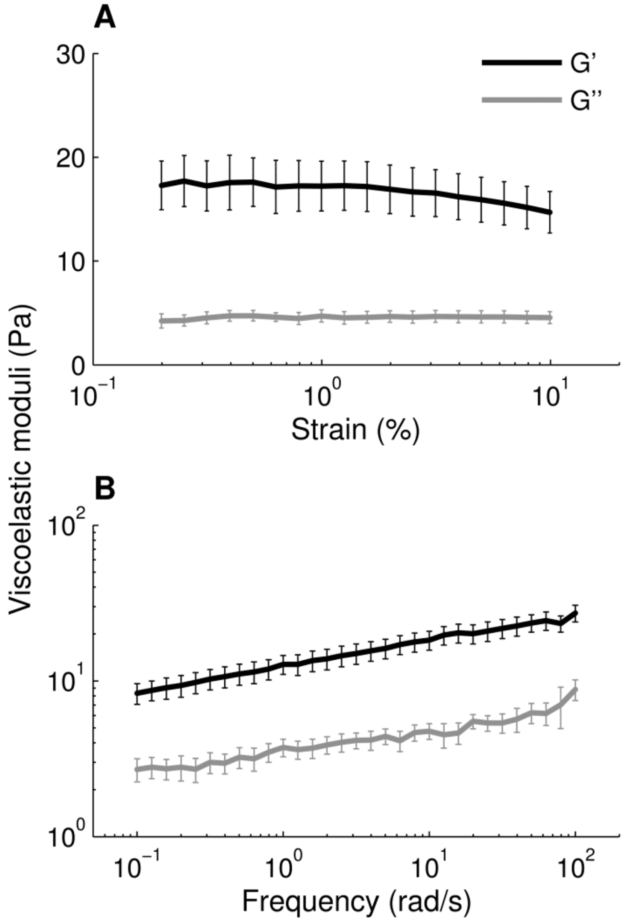

Figure 3.1. Bulk rheology of airway mucus.

(A) Strain-dependent viscous and elastic moduli from 0.2 to 10% strain at a frequency of 1 Hz (6.28 rad/s). (B) Frequency-dependent viscous and elastic moduli from 0.1 to 100 rad/s at 1% strain. Error bars represent standard error of the mean for n = 5 mucus samples.

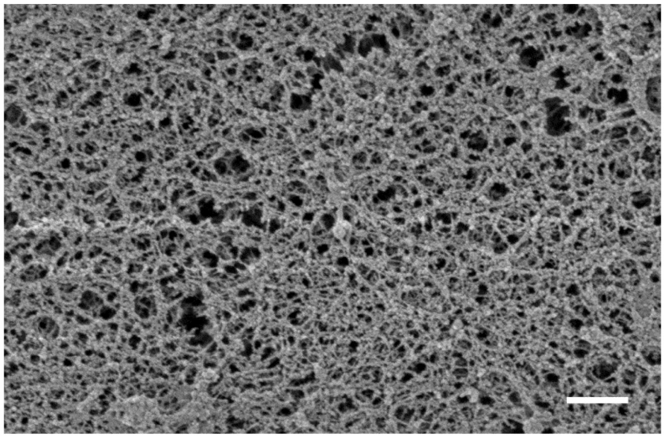

Figure 3.2. Scanning electron micrograph shows microstructure of airway mucus. Scale bar represents 500 nm. Because the specimen was fixed with glutaraldehyde and stained with heavy metals, and furthermore because the image shows multiple layers, the pore size of native mucus cannot be quantitatively measured from this image.

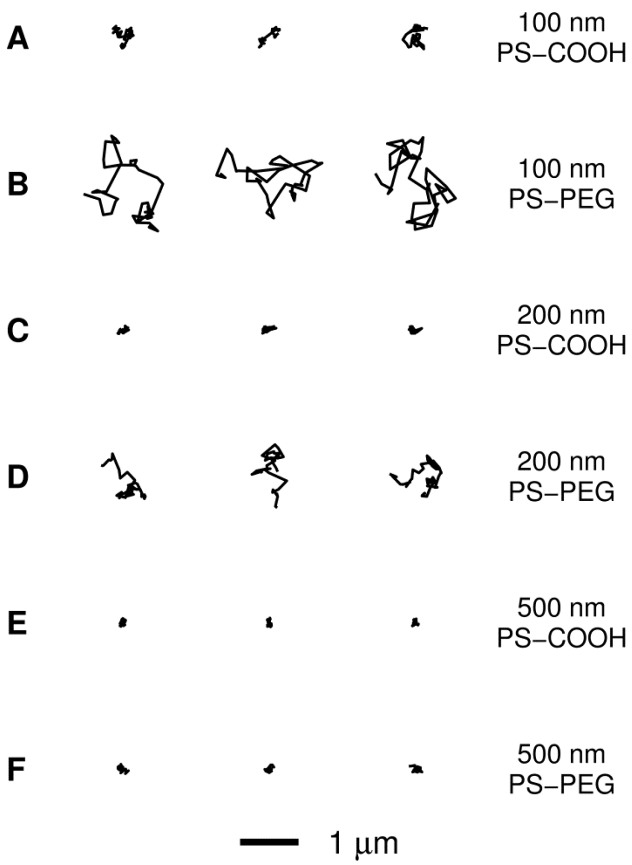

Figure 3.3. Representative trajectories of nanoparticles in airway mucus.

Trajectories show 3 s of motion. The trajectories presented are within one standard error of the mean MSD for each particle type. (A) 100 nm PS-COOH particles. (B) 100 nm PS-PEG particles. (C) 200 nm PS-COOH particles. (D) 200 nm PS-PEG particles. (E) 500 nm PS-COOH particles. (F) 500 nm PS-PEG particles.

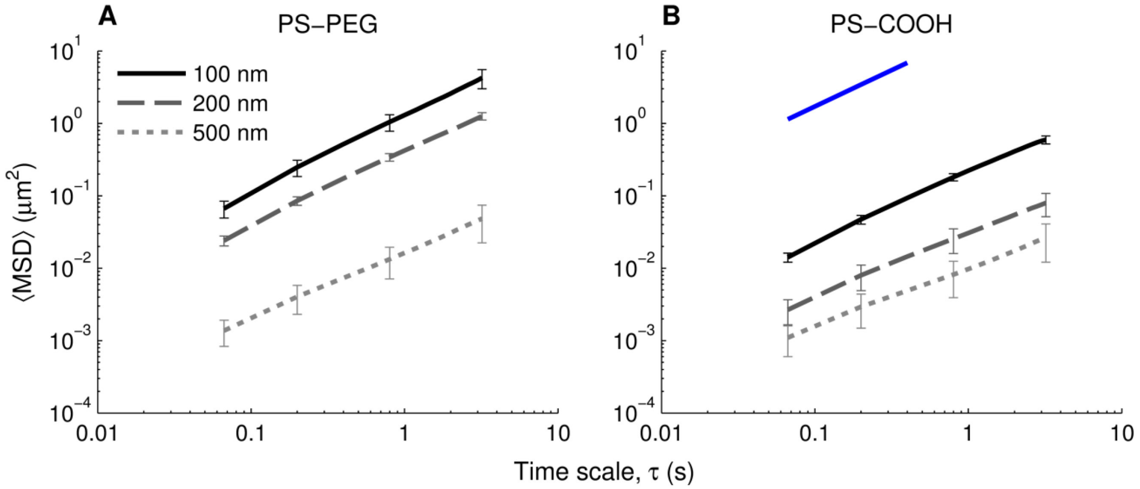

Figure 3.4. Ensemble-averaged geometric mean squared displacement (⟨MSD⟩) as a function of timescale for nanoparticles in airway mucus.

(A) 100, 200, and 500 nm PS-PEG particles. (B) 100, 200, and 500 nm PS-COOH particles. Data represents 5 mucus samples, with at least 100 particles of each particle type tracked per sample. Error bars are presented as standard error of the mean. For reference, blue line in (B) denotes the MSD of 100 nm particles in water, calculated using the Stokes-Einstein equation.

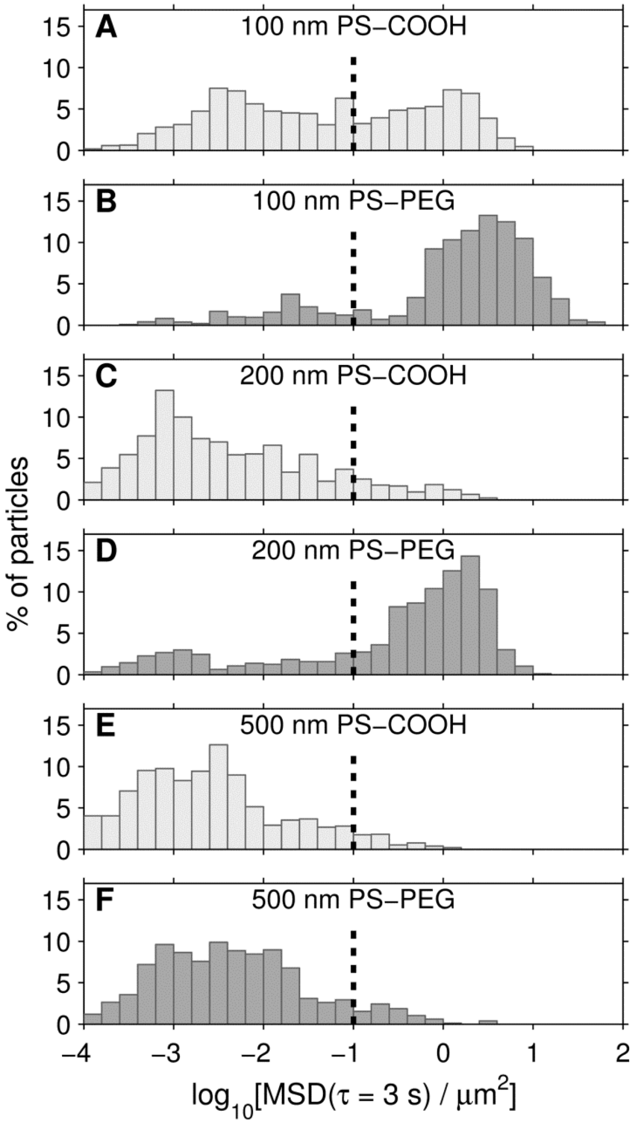

Figure 3.5. Distribution of individual particle mean squared displacements at a time scale of 3 s.

Data represents 5 mucus samples, with at least 100 particles of each type tracked per sample. (A) 100 nm PS-COOH particles. (B) 100 nm PS-PEG particles. (C) 200 nm PS-COOH particles. (D) 200 nm PS-PEG particles. (E) 500 nm PS-COOH particles. (F) 500 nm PS-PEG particles. The dashed vertical black lines indicate the threshold for immobile (left of the line) and mobile (right of the line) particles, as discussed in 3.3.4.

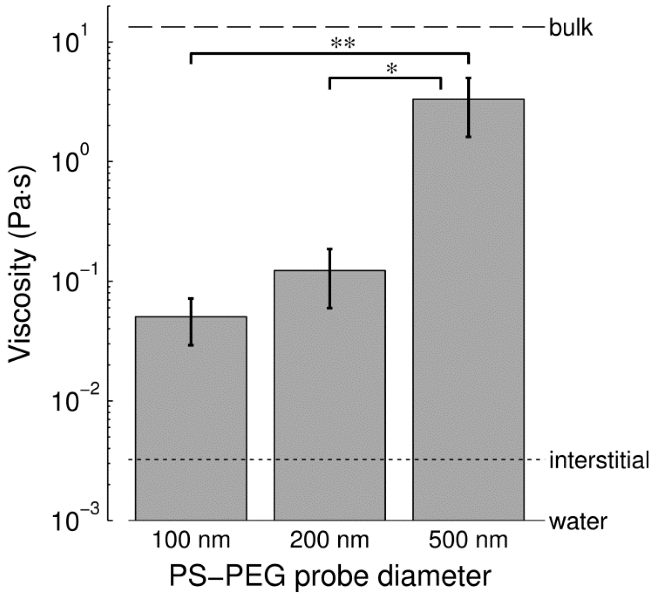

Figure 3.6. Micro- vs. macroscopic viscosity of human respiratory mucus. Viscosity reported is $|\eta(\omega)^*|$, the magnitude of the complex viscosity, at $\omega = 1$ rad/s. Complex viscosity incorporates both the viscous and elastic contributions to a material's rheological behavior. Microscopic viscosity experienced by 100, 200, and 500 nm PS-PEG probes in respiratory mucus was measured by particle tracking microrheology (PTM). Macroscopic viscosity, also called bulk viscosity (dashed horizontal line), was measured using a cone-and-plate rheometer. Mucus interstitial fluid (dotted line) was characterized by centrifuging mucus samples and measuring the supernatant's viscosity by PTM. For reference, the viscosity of water at 20 °C is also shown (solid horizontal line). Viscosity values represent n = 5 mucus samples, and error bars indicate standard error of the mean. Brackets with asterisks denote statistically significant differences (*, $P < 0.01$; **, $P < 0.005$).

4. OVERCOMING THE CYSTIC FIBROSIS SPUTUM BARRIER TO LEADING ADENO-ASSOCIATED VIRUS GENE THERAPY VECTORS[2]

4.1. Introduction

Cystic fibrosis (CF) is an autosomal recessive disorder that afflicts approximately 70,000 people worldwide.[3] In patients with CF, absence of functional cystic fibrosis transmembrane conductance regulator (CFTR), a chloride channel, impairs salt and water balance at epithelial surfaces.[6] Lung disease is the primary cause of morbidity and mortality in CF. A vicious cycle of airway obstruction, chronic infection, and inflammation causes progressive decline in lung function.[6,8] The median predicted survival age of CF patients has climbed in recent decades, but it is still only about 40 years.[6] Advances in recent decades include aerosolized antibiotics, pancreatic enzyme supplements, and improved devices and medications to help clear secretions from the lungs.

Following discovery of the *CFTR* gene in 1989, researchers envisioned treating CF by delivering the correct gene directly to patient lungs to restore CFTR function.[8] In cell culture and animal models, gene therapy has successfully mediated CFTR expression and corrected chloride current.[85,86] However, achieving clinical efficacy in humans has proven challenging.[8,87] Despite 25 clinical trials testing adenovirus (AdV), adeno-associated virus (AAV), and non-viral vectors, gene therapy has yet to produce clinically significant improvements in CF patient lung function.[8,87] These disappointing results have been blamed on immune response to the gene vectors, inefficient transduction of

---

[2] This chapter appears in Schuster, BS, Kim, AJ, Kays, JC, Kanzawa, MM, Guggino, WB, Boyle, MP, Muzyczka, N, Suk, JS and Hanes, J. Overcoming the Cystic Fibrosis Sputum Barrier to Leading Adeno-associated Virus Gene Therapy Vectors. *Molecular Therapy*. 2014; 22(8):1484-93

human airway epithelium via the apical membrane, and weak promoters to drive gene expression.[8]

Another major obstacle to pulmonary gene therapy for CF is the layer of viscoelastic airway secretions that coats the CF lung epithelium.[8,88,89] CF airway secretions are a gel comprised of entangled and cross-linked mucins, DNA, actin, and other macromolecules and cell debris.[13] This biopolymer network may trap inhaled particles by steric obstruction and specific or non-specific adhesive interactions.[17,89] Nevertheless, most CF gene therapy preclinical research has been conducted using cell culture and animal models that lack CF-like airway secretions and thus do not fully mimic the CF lung.[8] We previously found, in a proof-of-concept study, that sputum from five CF patients strongly hindered diffusion of AdV and AAV serotype 5 (AAV5).[90] Likewise, CF sputum inhibited AdV-mediated transfection in *in vitro* and *ex vivo* experiments.[91] These studies underscore that airway secretions can act as a barrier and prevent inhaled viral vectors from reaching target lung cells.

Given its clinical significance, much remains to be learned about the CF sputum barrier to AAV gene therapy. AAV2 was the first AAV serotype characterized and the only one tested in CF clinical trials, yet whether AAV2 can penetrate CF sputum is unknown. AAV is a leading viral gene delivery platform, and numerous other AAV serotypes have been investigated for their ability to transduce airway cells.[88,92] AAV5 exhibited enhanced transduction efficiency in the mouse lung compared to AAV2,[92] which motivated our prior work testing AAV5 diffusion in CF sputum.[90] A more recent study showed AAV1 outperformed AAV5 in human primary airway cells and in chimpanzees.[88] Because AAV1 has emerged as a promising candidate for future CF gene therapy clinical trials, its ability to penetrate CF sputum must also be assessed. All AAV serotypes have non-enveloped, icosahedral, ~25 nm diameter capsids,[93] so the sputum mesh will sterically obstruct all serotypes equally. However, the serotypes differ in their tropisms and binding affinities,[9,93-95] which may alter their adhesion to, and thus their diffusion through, sputum.

Here, we investigated diffusion of AAV1 and AAV2, compared to AAV5, in sputum samples from adult CF patients. Using multiple particle tracking and automated image analysis, we measured the movement of >30,000 AAV particles at single virus resolution in >20 patient samples. We observed that CF sputum hindered a large fraction of AAV particles, regardless of serotype. The sizeable patient population and number of viruses studied enabled us to examine inter- and intra- patient variability. Furthermore, we demonstrated two methods to improve AAV diffusion in CF sputum: virus capsid modification and mucolytic therapy with N-acetylcysteine. Our findings suggest strategies and future research directions for overcoming the CF sputum barrier to clinically successful inhaled gene delivery.

4.2. Materials and methods

4.2.1. Production of AAV

Recombinant AAV was prepared by the Vector Core at the University of Florida Powell Gene Therapy Center. AAV1, 2, and 5 were packaged with pTR-UF11 (single-stranded enhanced green fluorescent protein [eGFP] genome). For AAV1, the *rep2*, *cap1*, and AdV early genes were contained in the helper plasmid pKrap1A. For AAV2, the *rep2*, *cap2*, and AdV genes were contained in the helper plasmid pDG-KanR. For AAV5, the *rep2*, *cap5*, and AdV genes were contained in the helper plasmid pXYZ5.

The mutant AAV2 studied in this paper had the arginine residues at capsid positions 585 and 588 mutated to alanines. These mutations have previously been shown to reduce heparin binding.[93,96,97] The virus packaged pds-eGFP (double-stranded eGFP genome). The helper plasmids were pXX6 (containing the AdV genes) and mutant pIM45 (containing *rep2* and the mutant *cap2*).

AAV was produced as previously described.[98,99] Briefly, the vectors were produced via calcium phosphate-based co-transfection (for AAV1, 2, and 5) or triple transfection (for the AAV2 mutant) of plasmid into HEK293 cells. The transfected cells were incubated for approximately 72 hours, then harvested and lysed by freeze/thaw. The resultant cell lysates were digested with Benzonase, centrifuged to remove cellular debris, and purified by iodixanol density step gradient centrifugation followed by ion exchange chromatography. Buffer exchange and concentration were performed using centrifugal concentrators into the final stock buffer (PBS).

AAV produced by this technique is at least 99% pure, as determined by PAGE/silver stain.[100] The iodixanol density gradient centrifugation procedure separates full, genome-containing capsids from both free capsid proteins and empty capsids.[98] This was confirmed by comparing the capsid ELISA titer (PROGEN Biotechnik GmbH, Heidelberg Germany), using monoclonal antibodies that recognize only intact capsids, with the genome titer measured by DNA dot blot.

4.2.2. Fluorescent labeling of AAV

For virus tracking, AAV was labeled with the amine-reactive fluorescent dye Alexa Fluor 647 carboxylic acid, succinimidyl ester (AF647; Life Technologies, Carlsbad, CA). The autofluorescence of CF sputum is minimized at long-wavelength excitation, so using a deep red fluorophore such as AF647 allowed us to more easily distinguish the AAV particles. The labeling protocol was based on methods reported in the AAV literature.[101] AF647 was reconstituted in DMSO and added, along with borate buffer (pH 8.3), to AAV. The final reaction volume was 150 μL and contained approximately 10^{11} virus particles, 15% (v/v) DMSO, 100 mM borate buffer, and 100 μM AF647. The reaction was placed on a lab rotator at 4 °C in the dark. After two hours, unreacted dye molecules were removed by buffer exchange into PBS using a standard separation technique, gel filtration chromatography,[101] whereby unreacted dye was retained in the gel filtration media while labeled virus eluted from the column. The gel filtration media we used was Sephadex G-50 (illustra ProbeQuant G-50 Micro Columns; GE Healthcare, Little Chalfont, UK). Labeled virus was stored in 5 μL aliquots at -80 °C.

4.2.3. Quantitative real-time PCR

Titers of AAV and AF647-labeled AAV were measured using quantitative real-time PCR on a MyiQ2 thermal cycler (Bio-Rad, Hercules, CA) using SsoAdvanced SYBR Green Supermix (Bio-Rad). Primers against the CMV/chicken beta actin promoter in the AAV genomes were purchased from Eurofins MWG Operon (Huntsville, AL) with the following sequences: forward primer, 5’-TCCCATAGTAACGCCAATAGG-3’, reverse primer, 5’-CTTGGCATATGATACACTTGATG-3’.[99] Equal numbers of viruses were then used to compare the infectivity of AAV2 and AAV2-AF647 in cell culture.

4.2.4. Cell transduction experiments and flow cytometry

AAV transduction experiments were conducted using a human bronchial epithelial cell line, BEAS-2B. The cells were grown in DMEM/F12 (Life Technologies) supplemented with 10% fetal bovine serum (Life Technologies) and antibiotics (100 U/mL penicillin and 100 µg/mL streptomycin; Quality Biological, Gaithersburg, MD). Cells were incubated at 37°C in a 5% CO_2 atmosphere. For the transduction experiments, cells were seeded at a density of 40,000 cells/well in 24-well plates. After seeding, cells were allowed to grow for 24 h before adding AAV.

For comparing the infectivity of AAV2 with AF647-labeled AAV2, virus was added to the cells at a multiplicity of infection (MOI) of 2×10^3 vgc/cell. GFP expression was measured by flow cytometry 48 h after adding the virus.

We conducted heparin competition experiments to check the relative heparin binding strengths of AAV2 and the AAV2 mutant. In these studies, prior to the addition of virus, the regular media was replaced with media into which had been dissolved heparin sodium salt (from porcine intestinal mucosa; Sigma-Aldrich, St. Louis, MO) at concentrations of 10, 25, or 100 µg/mL. An MOI of 10^5 vgc/cell was used throughout, to achieve significant GFP expression for all serotypes, including the AAV2 mutant, which generally has lower transduction efficiency than wild-type AAV2 *in vitro*.[93] The media was removed 3 h after adding the virus and replaced with fresh media without heparin. GFP expression was measured by flow cytometry 48 h after adding the virus.

To determine if NAC affected AAV1 transduction, we conducted experiments in which, immediately prior to adding virus, the regular cell culture media was replaced by media containing NAC at a concentration of 5 mM. AAV1 was then added at an MOI of 2×10^4 vgc/cell. GFP expression was measured by flow cytometry 48 h after adding the virus.

Flow cytometry was conducted with an Accuri C6 flow cytometer (BD Biosciences, San Jose, CA) using the 488 nm laser. GFP fluorescence was detected in the FL1 channel with a 533/30 nm band-pass filter. For each well on a 24-well plate, 10,000 cells were counted.

4.2.5. CF sputum sample collection

Expectorated sputum samples were collected from patients at the adult CF clinics at Johns Hopkins (n = 23) and the University of Alabama at Birmingham (n = 3). Samples from Hopkins were stored at 4 °C and analyzed the day after collection. Samples from Alabama were shipped overnight, on ice, to Hopkins and also analyzed the day after sample collection. Samples were collected under written informed consent, in accordance with Institutional Review Board approval and following Declaration of Helsinki protocols.

Patients involved in this study received no mucolytics other than Pulmozyme® (rhDNase, which cleaves DNA in sputum) as part of their treatment regimen. 19% of patients received Pulmozyme® between 2 and 6 hours prior to when their sputum sample was collected, 50% of patients last received Pulmozyme® the day before sample collection or earlier, and 31% of patients were not taking Pulmozyme®.

4.2.6. Preparing PS-PEG and PS-PEG-AF647 nanoparticles

PEG-coated polystyrene particles (PS-PEG) were prepared as detailed previously.[17] Briefly, fluorescent carboxylate-modified polystyrene spheres (PS-COOH), 100 nm and 500 nm in diameter, were purchased from Molecular Probes or Bangs Labs. To coat the PS-COOH particles with PEG, 5 kDa methoxy-PEG-amine (Creative PEGWorks, Winston-Salem, NC) was covalently coupled to carboxyl groups on the PS-COOH particles using 1-ethyl-3-(3-dimethylaminopropyl) carbodiimide hydrochloride (EDC) and N-hydroxysulfosuccinimide sodium salt (sulfo-NHS; Sigma-Aldrich) in borate buffer (pH 8.3). After reacting for 4 h, the resulting PS-PEG particles were centrifuged and washed in ultrapure water. Our lab recently measured the surface density of PEG on PS-PEG particles prepared according to this protocol to be 0.09 PEG/nm^2, which suggests the PEG layer has a dense brush conformation ideal for resisting protein adhesion.[18] We did not use AAV-sized polymeric particles in this paper because commercially available 20 nm PS-COOH particles are more challenging to PEGylate sufficiently to block adhesion to mucus, probably due to the small radius of curvature, and they also have lower fluorescence intensity and consequently are more difficult to track, compared to 100 nm or larger PS-COOH particles.

To prepare 100 nm PS-PEG particles labeled with AF647 (PS-PEG-AF647), a modified version of this protocol was used. First, the carboxyl groups on the PS-COOH particles were activated by reacting PS-COOH particles, NHS, and EDC in 50 mM MES buffer (pH 6.0) for 1 h. Next, the particles were centrifuged and resuspended in 100 mM borate buffer (pH 8.3), to which 5 kDa carboxyl-PEG-amine (JenKem Technology USA, Allen, TX) was added at a 5-fold molar excess to the number of carboxyl groups on the PS-COOH particles. This mixture was allowed to react for 2 h, to couple the amine groups on the PEG with the activated carboxyl groups on the particles. Then, the particles were centrifuged and resuspended in fresh borate buffer, to which was added NHS, EDC, and Alexa Fluor 647 cadaverine, disodium salt (Life Technologies). The dye was added at a 1:1 molar ratio to the number of carboxyl groups on the PS-COOH particles (the maximum number of PEG chains that could have attached). This mixture reacted overnight, coupling the amine on the AF647-cadaverine with the carboxyl group on the free end of the PEG chains. Finally, the PS-PEG-AF647 particles were centrifuged and washed in ultrapure water until the supernatant was free of visible dye.

PS-COOH, PS-PEG, and PS-PEG-AF647 particles were stored at 4 °C. For particle tracking experiments, the particles were diluted with ultrapure water to concentrations ideal for tracking individual particles.

4.2.7. Particle size measurements

AAV and nanoparticle size were measured by dynamic light scattering using a Zetasizer Nano ZS (Malvern Instruments, Malvern, UK), which uses a 633 nm laser and has a 173° scattering angle. Measurements were conducted at 25 °C. AAV was suspended in PBS (pH 7.4), while the nanoparticles were suspended in PBS diluted to have 10 mM NaCl concentration.

4.2.8. Scanning electron microscopy

Sputum was prepared for electron microscopy following an established protocol, as described previously.[17] Briefly, sputum samples were fixed in 2% glutaraldehyde, postfixed in 1% OsO_4, and then stained with 2% uranyl acetate. The specimens were then dehydrated through a graded series of ethanol solutions, followed by immersion in hexamethyldisilazane, and then desiccated under vacuum overnight. The samples were attached to aluminum stub mounts, sputter coated with 20 nm of AuPd, and imaged with a field-emission scanning electron microscope (LEO 1530 FESEM; Zeiss, Jena, Germany).

4.2.9. Particle tracking: sample preparation and microscopy

Movement of viruses and nanoparticles in sputum was measured by multiple particle tracking. The sample preparation procedure was designed to minimize manipulation of the sputum and maintain its microarchitecture. Sputum aliquots (~30 µL each) were withdrawn from the sputum sample using a Wiretrol (Drummond Scientific Company, Broomall, PA) and dispensed into custom microscopy chambers. Aliquots were withdrawn from the same approximate location in the sputum sample to minimize the effects of intra-sample heterogeneity.

To each sputum aliquot was added 0.5 µL of one serotype of AF647-labeled AAV, plus polymeric nanoparticles as controls: either 0.5 µL of green fluorescent 500 nm PS-PEG particles, 0.5 µL of red fluorescent 100 nm PS-PEG particles, or 0.5 µL each of the 100 nm and 500 nm PS-PEG particles. Thus, in total, no more than 1.5 µL of virus and nanoparticle suspensions were added to ~30 µL of sputum, so the sputum aliquots were diluted 5% v/v or less. In our current and previously published work, we found that dilutions of this magnitude did not alter the ability of sputum to sterically and adhesively trap particles.[50,84]

After adding the particles, the sputum aliquots were gently stirred with a pipette tip, and then the chambers were sealed with a coverslip to prevent sample dehydration. After incubating the chambers for 1 h, they were imaged at room temperature using an inverted epifluorescence microscope (Axio Observer; Zeiss) located on a vibration isolation table and employing a 100x/1.46 NA oil-immersion objective. Care was taken to focus the objective at least 2 μm above the coverslip surface to minimize edge effects. Movies of virus and nanoparticle motion in the sputum samples were recorded at a frame rate of 15 Hz, for 150 or 300 frames, using an EM-CCD camera (Evolve 512; Photometrics, Tuscon, AZ). For each sputum sample, five to ten movies of each virus serotype or nanoparticle type were collected.

To determine the effect of the mucolytic drug NAC on AAV transport in CF sputum, a solution of NAC (neutralized to a pH of 7) was mixed into sputum to a final concentration of 5 mM. For the untreated control, a comparable volume of PBS was added to sputum. NAC-treated and control samples were then incubated at 37°C for 30 min. AAV1-AF647 was then added to the samples in custom microscopy chambers, the slides were incubated for 1 h at 37°C, and imaging was performed using the procedure above. In this experiment, the sputum samples were again diluted 5% (v/v) or less. Finally, to determine the effect of AF647 labeling on particle transport, we prepared sputum aliquots with 100 nm PS-PEG, 100 nm PS-PEG-AF647, and 100 nm PS-COOH particles.

4.2.10. Particle tracking analysis

Movies were analyzed using automated particle tracking software custom-written in MATLAB (MathWorks, Natick, MA), based on the algorithm of Crocker and Grier,[2] to determine the x and y positions of particles over time. Images were first processed by convolving them with a spatial bandpass filter to reduce noise and non-uniform background. Local maxima of pixel intensity were identified as candidate particle positions. These positions were refined by calculating the intensity-weighted centroid of the bright spots, to yield sub-pixel resolution. By examining particle brightness, size, and eccentricity, true particles were retained and spurious ones (noise) discarded. Trajectories were constructed by linking particle positions identified in subsequent frames via a nearest neighbor method. The time-averaged mean squared displacement (MSD) of each trajectory was calculated as $MSD(\tau) = \langle[x(t + \tau) - x(t)]^2\rangle + \langle[y(t + \tau) - y(t)]^2\rangle$, where τ is the time scale, and the angled brackets denote the average over many starting times t. Scanning electron microscopy (Figure 4.6) suggests that sputum is isotropic, so the 2-dimensional MSD measured here equals two-thirds of the three-dimensional MSD. We presented our results at a time scale of 1 s; trajectories shorter than 1 s are not useful in this context and were thus discarded. There is a possibility that we discarded some rapid particles that were in focus for less than 1 s, but our visual observations suggest that is an infrequent occurrence.

Tracking resolution was estimated based on a published method.[38] First, the signal-to-noise ratio (SNR) was calculated from the experimental movies (particle tracking movies of AAV and nanoparticles in sputum). These were compared to a standard curve of static error as a function of SNR, to estimate the static error in the experimental movies. The standard curve was generated by affixing particles to a glass slide and tracking them under different illumination intensities; the apparent motion of these fixed particles is due to static error. For 100 nm PS-PEG particles in sputum, the tracking resolution was approximately 25 nm. For AAV, the tracking resolution was approximately 75 nm, since the viruses are dim and their positions cannot be estimated as accurately. The MSDs of fast particles and viruses – those of greatest clinical interest, because they are most likely to penetrate CF sputum – are well above the noise floor at a times scale of 1 s.

4.2.11. Statistical analysis

Student's *t*-tests and ANOVA were conducted in MATLAB (MathWorks). Linear mixed effects models were constructed using the lme4 package[102] in the statistical language R to examine the relationship between AAV2 capsid and MSD (at a time scale of 1 s) in sputum. In these models, MSD was the dependent variable, and AAV2 capsid (mutated or wild-type) was set as a fixed effect. The random effects were patient sample number, as well as by-patient random slopes for the effect of AAV capsid. Residual plots did not show major deviations from homoscedasticity or normality. The p value was calculated by a likelihood ratio test of the full model, which includes AAV capsid type, against the null model, which excludes AAV capsid type. Linear mixed-effects models were also used to compare the extent of intra- and inter- sample variability; here, MSD of 100 nm PS-PEG particles was the dependent variable, and both patient and sputum aliquot number were set as random effects.

4.3. Results

4.3.1. Characterization of fluorescently labeled AAV

We labeled the AAV capsid with a deep red fluorescent dye, Alexa Fluor 647 (AF647), to track the movement of AAV in freshly collected human CF sputum. To assess whether attaching this exogenous dye molecule would affect our subsequent studies, we examined the consequences of dye labeling on AAV infectivity and on particle transport in CF sputum.

First, we examined whether AF647 labeling altered AAV infectivity. We infected BEAS-2B bronchial epithelial cells with AAV2 or with AF647-labeled AAV2 (AAV2-AF647) at the same MOI. The virus carried a GFP reporter gene, which allowed us to assess transduction efficiency by fluorescence microscopy and flow cytometry (Figure 4.1a-d). We found no statistically significant difference in gene expression by the cells infected with AAV2 as compared to with AAV2-AF647 (two-sided *t*-test, p = 0.25). Next, we examined whether attaching AF647 affected particle diffusion in CF sputum. Since we could not image unlabeled AAV, we addressed this question using polystyrene (PS) nanoparticles internally labeled with a fluorescent dye, and which were densely coated with polyethylene glycol (PEG) to minimize adhesion to sputum (PS-PEG).[17,50,103] We measured the transport in CF sputum of 100 nm PS-PEG particles as compared to 100 nm PS-PEG particles further labeled with AF647 on the particle surface (PS-PEG-AF647). A histogram of the mean squared displacement (MSD) of PS-PEG particles in CF sputum (Figure 4.1e) was nearly identical to that of PS-PEG-AF647 (Figure 4.1f).

Finally, using dynamic light scattering, we confirmed that dye labeling did not affect the size of AAV or PS-PEG particles (Table 4.1). Together, these studies strongly suggest that labeling AAV with dye did not alter its biological activity or diffusivity.

4.3.2. Transport of AAV serotypes 1, 2, and 5 in CF sputum

We studied the diffusion of AAV serotypes 1, 2, and 5, as well as polymeric nanoparticles for comparison, in 10 CF sputum samples. Using particle tracking and automated image analysis, we analyzed the trajectories of tens of thousands of viruses and nanoparticles. Histograms of individual particle MSDs at a time scale of 1 s, averaged over the 10 patient samples with each sample equally weighted, are shown in Figure 4.2 and Figure 4.7. In 20 ºC water, a 25 nm diameter AAV particle would have a two-dimensional MSD of 69 μm^2 at 1 s, according to Stokes-Einstein theory.[2,39] In comparison, all three AAV serotypes were greatly slowed in CF sputum (Figure 4.2b-d). Approximately 50% of the AAV particles moved less than 1/1,000th their theoretical MSD in water, with MSD < 0.069 μm^2 (or $\log_{10}$MSD < -1.2) at 1 s.

We found that transport rates of individual particles in sputum ranged as much as five orders of magnitude (Figures 4.2 and 4.3), compared to approximately three orders of magnitude for AAV in water (Figure 4.8), which reflects the heterogeneous nature of CF sputum.[104] Fast-moving particles are of particular interest, since they have the greatest likelihood of penetrating the sputum layer. All AAV serotypes tested had a subpopulation of fast-moving particles, which we define as those with MSD ≥ 1 μm^2 (or $\log_{10}$MSD ≥ 0) at 1 s. Using this definition for fast-moving particles, 15%, 8%, and 6% of AAV1, AAV2, and AAV5, respectively, diffused rapidly in CF sputum (Figure 4.2b-d). The

MSDs of these fast particles typically increased linearly with time, so if we extrapolate, a freely diffusing particle that has an MSD (measured by two-dimensional particle tracking) of 1 μm^2 at 1 s could penetrate a 10 µm sputum layer (considering only motion in the z-direction) in 200 s. Likewise, the same particle could penetrate a 40 µm sputum layer in about 50 min. In other words, the small but important subpopulation of fast-moving particles would be able to traverse physiologically relevant distances[13] in under an hour, and may be more likely to penetrate the airway secretions and reach epithelial cells *in vivo* prior to being removed by mucociliary clearance. Measurements of mucociliary clearance rates in CF patients vary widely; the percentage of inhaled particles cleared from CF lungs within an hour ranged from about 15 to 60% in various studies.[105]

Overall, only approximately 5-15% of AAV particles were diffusive, while the majority of particles were greatly hindered or immobilized in sputum. For comparison, we also measured the diffusion of polymeric nanoparticles in sputum. Our lab has previously shown that small polymeric nanoparticles, if densely coated with PEG to render their surfaces hydrophilic and resistant to mucus adhesion, diffuse faster in sputum than do comparably sized adhesive particles. However, particles larger than the mesh size of the sputum, even if PEG-coated, are sterically immobilized.[17,50] Here, we found that in contrast to AAV, nearly 40% of the adhesion-resistant 100 nm PS-PEG particles diffused rapidly (Figure 4.2a). Meanwhile, only 3% of the 100 nm uncoated carboxylate polystyrene particles (PS-COOH), and only 1% of the 500 nm PS-PEG particles, diffused rapidly in sputum (Figure 4.7b,c), which agrees with our previous findings.[50]

4.3.3. Patient-to-patient variation in AAV transport

We found that AAV and 100 nm PS-PEG particle mobility varied substantially from patient to patient. Figure 4.3a shows boxplots of particle MSDs (at a time scale of 1 s) for sputum samples from 10 CF patients; Figure 3b shows representative trajectories of particles in three of those samples. On one end of the spectrum is patient 1, in whose sputum sample the majority of AAV and 100 nm PS-PEG particles were immobilized, as illustrated by their highly constrained trajectories. Towards the other end of the spectrum is patient 9, in whose sputum sample larger fractions of AAV and 100 nm PS-PEG particles were diffusive, as can be seen from their Brownian trajectories (Figure 3b). Particle transport in sample 1 was significantly different from that in sample 9 (and also significantly different from that in samples 4, 8, and 10; $p < 0.01$ by two-way ANOVA followed by Tukey's HSD test). The three AAV serotypes tested had similar transport rates within most of the samples. However, in patients 5 and 7, different serotypes exhibited divergent transport behavior. Those sputum samples may have had different binding affinities for different AAV serotypes, but intra-sample variability likely also contributed to the variation.

To assess the extent of inter- vs. intra- sample variability, we tracked 100 nm PS-PEG particles in the same sputum aliquots in which we tracked the various AAV serotypes. This provided us with transport data of one particle type in multiple sputum aliquots from each of nine CF sputum samples (Figure 4.9). From this 100 nm PS-PEG particle transport data, we found that the variance between samples of log10MSD was 1.00, which was 50 times the variance within samples, 0.02 (linear mixed-effects model[102] fit by maximum likelihood). This strongly suggests that the variation among different samples can largely be attributed to patient-to-patient differences, rather than to intra-sputum sample heterogeneity.

We investigated whether patients' pulmonary function test results (summarized in Table 2; higher scores indicate better lung health) could explain the patient-to-patient variation in AAV transport, but we did not find strong correlations. For instance, we found that median $\log_{10}$MSD at 1 s of AAV2 increased marginally with forced expiratory volume ($R^2 = 0.33$) and forced vital capacity ($R^2 = 0.12$). Similarly, we found only weak correlations between AAV transport rates and the measured solids content (percent dry weight[17]) of sputum samples (e.g., $R^2 = 0.105$ for AAV2).

Finally, we note that patients involved in this study received no mucolytics other than Pulmozyme®. Furthermore, particle transport was not faster in sputum from patients who received Pulmozyme® between 2 and 6 hours prior to when their sputum sample was collected (patients 2 and 5 in Figure 4.3), as compared to those who last took Pulmozyme® the day before sample collection (patients 1, 3, 7, and 9), and as compared to those not on Pulmozyme® (patients 4, 6, 8 and 10 in Figure 4.3). This agrees with our prior finding that Pulmozyme® treatment of sputum *ex vivo* did not affect particle transport.[68,84] Thus, Pulmozyme® treatment status does not appear to be responsible for the patient-to-patient variation in particle transport observed here.

4.3.4. Effect of AAV2 capsid mutation

Adhesion can immobilize particles in sputum, so we next investigated whether modifying the viral capsid to reduce adhesion could improve AAV transport. AAV2 binds to heparan sulfate proteoglycan and heparin.[93] This may pose a challenge for sputum penetration because heparan sulfate is abundant in human tissues and elevated in the CF lung,[106] and has also been identified in sputum from patients with bronchiectasis,[107] a key feature of CF.[6] Thus, we hypothesized that a mutant AAV2, whose capsid was mutated at positions 585 and 588 to reduce heparin binding, as previously described,[93,96,97] would diffuse faster than AAV2 in sputum.

First, to confirm that the AAV2 mutant indeed had reduced binding affinity for heparin, we conducted an *in vitro* heparin competition assay (Figure 4.4a). We added AAV2 or the AAV2 mutant to BEAS-2B bronchial epithelial cells bathed in media with increasing concentrations of dissolved heparin. We assessed transduction efficiency by measuring AAV-mediated GFP expression using flow cytometry. Indeed, heparin inhibited AAV2 transduction significantly more strongly than it inhibited the AAV2 mutant (*t*-test; $p < 0.01$) for each of the three heparin concentrations tested. To check the validity of our assay, we confirmed that heparin did not inhibit BEAS-2B transduction by AAV1 or AAV5, as expected (Figure 4.10).

To study the effect of the capsid mutation on diffusion in sputum, we tracked AAV2 and the AAV2 mutant in sputum samples from 17 patients (Figure 4.4b). We found that the capsid mutation did affect AAV transport ($\chi^2 = 6.86$, $p = 0.0088$), increasing the median MSD at a time scale of 1 s by a factor of 2.2 ± 1.3. In four of the sputum samples, the median MSD of the AAV2 mutant was more than five times that of AAV2. Furthermore, in two sputum samples, there was more than an order of magnitude increase. However, since steric obstruction and adhesion to other sputum components besides heparan can also contribute to hindering AAV motion, we did not observe the largest improvements specifically in samples where AAV2 diffusion was poor. Overall, the data suggest that engineering the AAV2 capsid to reduce its adhesion to heparin can improve AAV2 transport in sputum.

4.3.5. Effect of N-acetylcysteine treatment

Previously, our group reported that pretreatment of CF sputum with the mucolytic drug N-acetylcysteine (NAC) resulted in improved transport of PS-PEG particles and non-viral gene carriers through the sputum.[68,84] NAC, which is FDA-approved for various routes of administration, including inhalation, breaks disulfide bonds that crosslink mucins into polymers and thereby reduces sputum viscoelasticity.[13,89] Here, we investigated whether pretreatment of sputum with NAC would also enhance AAV diffusion.

We measured AAV1 diffusion in untreated CF sputum compared to sputum pretreated with 5 mM NAC. We chose this concentration based on our earlier finding that millimolar concentrations of NAC enhanced PS-PEG particle transport in sputum, whereas concentrations one order of magnitude lower were much less effective.[68] NAC solution prescribed for inhalation (Mucomyst®) contains a concentration of 1.2 M, or 20%, NAC. Following a single treatment of NAC delivered by an LC Star jet nebulizer, the NAC concentration in the upper airways (generations 1-10) can reach a maximum concentration of about 50 mM, with the concentration exceeding 10 mM for more than 1 hour. Lower doses are achieved in the small airways (C. Ehre, personal communication, 2014). We found that 5 mM NAC can have a large effect on AAV1 transport (Figure 5a,b; we note that the sputum samples used in the NAC study were different from the samples used in Figures 4.2 and 4.3, and thus the percentage of fast AAV1 particles differs between Figures 4.2b and 4.5a). On average, more than 47% of the AAV1 particles diffused rapidly in NAC-treated sputum, compared to only 5% in untreated sputum. Again, we observed substantial sample-to-sample variation. In three of the five sputum samples tested, NAC improved AAV transport by one order of magnitude, whereas in two samples, NAC had little effect.

For NAC to be viable as an adjuvant for CF gene therapy, AAV must maintain its ability to transduce airway epithelial cells in the presence of NAC. We therefore assessed AAV1 transduction of BEAS-2B cells with and without 5 mM NAC in the cell culture media (Figure 4.5c). We found that NAC only slightly reduced transduction (by 10%; one-sided *t*-test, p = 0.027). Together, our experiments indicate that NAC can increase AAV1 penetration through sputum at concentrations that do not dramatically affect the virus's ability to transduce cells in culture. We expect similar results for other AAV serotypes, as NAC works in a non-specific manner by disrupting mucin crosslinking.

4.4. Discussion

Here, we report that CF sputum strongly hindered the transport of clinically and preclinically tested AAV serotypes, including AAV1, 2, and 5. We estimate that only 5-15% of AAV particles can penetrate a physiologically relevant distance in sputum fast enough to avoid clearance. This finding suggests that the CF sputum barrier likely contributed to the disappointing results of AAV2 clinical trials, by preventing most of the inhaled gene vectors from reaching airway epithelial cells. The inability of AAV to rapidly penetrate sputum necessitates strategies to overcome this barrier. We discovered that modulating the adhesive interactions and steric obstruction of AAV in sputum could improve virus transport, which suggests that it may be possible to overcome the CF sputum barrier to AAV gene therapy. Our discoveries were enabled by using multiple particle tracking and automated image analysis to examine tens of thousands of virus particles in >20 patient samples.

Adhesion is likely the primary mechanism by which sputum hinders AAV diffusion. There was a substantially smaller fraction of fast-moving AAV than of 100 nm PS-PEG particles – even though AAV is approximately four times smaller in diameter (~25 nm). This most likely occurred because AAV adheres to the network of biomolecules present in sputum, whereas the PEG-coated particles resist adhesion because of their adhesion-resistant surfaces.[17,50] Viruses may bind to sputum components non-specifically, such as by electrostatic interactions.[108] AAV may also adhere to sputum by specific binding interactions. AAV2 binds specifically to heparan sulfate proteoglycan,[93] which is abundant in the CF lung.[106] AAV5 binds to α2,3 N-linked sialic acids,[94] while AAV1 binds to both α2,3 and α2,6 N-linked sialic acids.[95] Mucins are rich in sialic acids, though predominantly of the O-linked variety.[95] One study demonstrated that AAV5 did bind to purified mucin,[109] though other studies showed that AAV1 and AAV5 did not bind strongly to purified mucin.[95,110] Mucins from different sources and disease states may vary in their glycosylation, and this could explain the contradictory reports. Secondary receptors have also been identified for AAV2 and AAV5.[9] Finally, antibodies may trap AAV in sputum.[89] Because of their small size, antibodies diffuse relatively unimpeded in human mucus, but the antibody Fc region forms transient, low-affinity bonds with mucus.[111-113] As antibodies accumulate on the surface of a virus, multivalent antibody interactions with the mucus mesh can trap the virus.[111-113]

Neutralizing antibodies against AAV2 have been found in approximately 30% of adults with CF.[114,115] Antibodies against AAV serotypes 1, 5, 6, 7, and 8 have also been found in humans, though typically with lower prevalence compared to AAV2.[115,116]

Physical obstruction by the sputum biopolymer meshwork can also trap particles. In a subset of patient samples, we found that the 100 nm PS-PEG particles, which resist adhesion to sputum, were mostly immobilized. This suggests that those samples' average pore size was less than 100 nm. Physical obstruction by the sputum meshwork likely contributed greatly to hindering AAV in those samples. Small pores also contribute to adhesive trapping, by increasing the probability of multivalent binding interactions between AAV and sputum.[17] Sputum samples can have a wide range of pore sizes,[84] so even samples with larger average pore sizes likely have some pores small enough to impede AAV motion.

We showed that modulating adhesion and physical obstruction may improve AAV diffusion in sputum. We tested a mutant AAV2, engineered at two capsid positions to have reduced heparin binding, and found that it diffused significantly faster in sputum than did AAV2. We attribute the faster transport of the mutant to reduced adhesion to heparan sulfate in sputum. A critical consideration is whether the AAV2 capsid modification will reduce transduction of polarized airway epithelial cells. Recent research shows that heparan sulfate is not essential for AAV2 transduction of airway cells,[117] so the AAV2 mutant may permit improved sputum penetration without compromising the vector's ability to transduce airway epithelial cells *in vivo*. Our work provides proof of concept that capsid modification may be an effective strategy for improving AAV diffusion in sputum, and it motivates further research to design a gene vector that can rapidly penetrate sputum, but is excellent at transducing lung cells *in vivo*. This may be a challenging task in general, given that the binding domains of cell surface receptors necessary for AAV transduction may also be present in sputum. A high-throughput screen of many AAV mutants may be the best approach to address this challenge.

We also found that physically altering sputum using the mucolytic drug N-acetylcysteine, which breaks intermolecular disulfide crosslinks and depolymerizes mucins, could markedly improve AAV transport in CF sputum. For some patients, this may be a relatively simple and feasible approach for improving gene vector penetration in sputum. NAC improved AAV transport by one order of magnitude in three of five sputum samples. The two sputum samples that showed little change with NAC treatment might have had high mucin content, as we previously found that the effectiveness of NAC treatment was inversely correlated with the mucin concentration – and hence the concentration of disulfide bonds – in the sputum sample.[84] In a recent review, the CF Foundation consensus panel found insufficient evidence that NAC improved CF patients' lung function, so could not recommend for or against its routine use; in contrast, the panel did recommend use of recombinant human DNase (dornase alfa, proprietary name Pulmozyme®), which acts as a mucolytic by degrading DNA in CF sputum and significantly improves pulmonary outcomes.[118] For the purpose of improving nanoparticle transport in sputum, however, our group previously found that DNase treatment alone was ineffective, while NAC treatment was effective.[84,104] Even if it is not routinely used for CF treatment, NAC could be useful as an adjuvant for AAV gene therapy. We did observe a small (~10%) reduction in AAV-mediated transduction of BEAS-2B cells when 5 mM NAC was added to the cell culture media. This reduction is small considering that NAC treatment may permit ten-fold more AAV to penetrate sputum. Furthermore, we expect that this reduction will be even smaller in the airways, where mucins will compete for NAC, as compared to our cell culture experiments, where the culture media did not contain mucin.

Although many of the AAV particles were immobilized in sputum, we found that a fraction of them were mobile, with substantial variation among patients. These data suggest that sputum may be a greater barrier to AAV gene delivery in some patients than in others. We observed a wide range in particle transport among patient samples, in agreement with other studies,[26] from essentially all particles immobilized to many particles diffusive. We reason that a complex interplay between patients' lung health, microbial colonization, mucin biochemistry, and airway hydration determines the physicochemical properties of their sputum, and thereby governs the extent to which their sputum sterically and adhesively impedes particle diffusion. It would be clinically useful to understand the molecular origins of these differences and identify sputum biomarkers predictive of AAV transport, but given the complex biochemistry of sputum, such an undertaking was beyond the scope of our current investigation.

We have also shown that labeling AAV with Alexa Fluor dye does not affect the virus infectivity or transport in CF sputum. Still, there are limitations to our experimental approach. The labeled viruses typically have low fluorescence intensity, and lower signal-to-noise ratio results in worse tracking resolution. More broadly, our approach of tracking viruses in expectorated sputum samples may not fully mimic the *in vivo* situation. First, the sputum that patients are able to cough out may differ somewhat in composition from the secretions coating their airways. Second, airway secretions *in vivo* sit above the cell-associated periciliary layer,[15] which may pose an additional barrier to gene delivery. However, recent work shows that the small size of AAV may facilitate penetration through the periciliary layer as well.[119] Third, while we studied the barrier properties of sputum, we did not directly assess how sputum affects AAV transduction.[91,120] One alternative experimental approach to address this issue would be to layer human CF sputum on top of cultured cells, then add AAV above the sputum, and assess how the sputum barrier affects transduction. We have found this to be challenging in practice because the CF sputum samples tend to infect the cell cultures with bacteria, and furthermore, it is difficult to add sputum at a physiologically accurate thickness (on the order of tens of μm). Fourth, we conducted the particle tracking experiments in static sputum samples, whereas the CF lung is a dynamic environment with at least some ciliary activity. In future studies, it would be valuable to study the transport of promising gene vectors in both human CF sputum and in the secreted mucus layer on primary airway epithelial cells cultured at the air-liquid interface (ALI). The former material more closely mimics the secretions lining the diseased CF lung, while the latter approach would permit us to study gene vector mobility in a dynamic environment with beating cilia. ALI cultures would enable us to experimentally compare the rate at which gene vectors can diffuse through mucus with the rate at which they are swept away by mucociliary clearance.

4.5. Conclusion

In summary, this work quantitatively demonstrated that CF sputum is a significant barrier to AAV gene therapy, and showed that capsid modification and the mucolytic adjuvant NAC enhanced AAV diffusion in sputum. In recent years, researchers have made promising advances in overcoming various roadblocks to AAV gene therapy, including engineering the AAV capsid to increase lung transduction,[121] optimizing the viral genome to enhance CFTR expression,[87] and minimizing immune response to AAV.[8] Our findings emphasize that CF sputum is another roadblock to CF gene therapy, and we provide guidance on how to overcome the sputum barrier to achieve improved clinical outcomes.

Table 4.1. Hydrodynamic diameter (nm) of unlabeled vs. Alexa Fluor-labeled AAV and PS-PEG particles.

	unlabeled[a]	**labeled**[a,b]
AAV1	20 ± 1	19 ± 1
AAV2	30 ± 1	30 ± 1
AAV5	21 ± 1	19 ± 1
AAV2 mutant	28 ± 0.2	28 ± 1
PS-PEG	128 ± 5	125 ± 1

Abbreviations: AAV, adeno-associated virus; PS-PEG, polystyrene particles coated with polyethylene glycol

[a] Measured by dynamic light scattering (DLS) using a Malvern Zetasizer Nano ZS. Data represents the mean of n = 3 measurements. Error values represent standard deviation.

[b] For these measurements, AAV was labeled with Alexa Fluor 555, rather than Alexa Fluor 647 (AF647), which was the dye used for the particle tracking experiments. The DLS instrument uses a 633 nm laser, so compounds such as AF647 that strongly absorb 633 nm light interfere with the size measurement and are incompatible with the instrument (see Malvern manual).

Table 4.2. Patient demographics for Figures 4.2 and 4.3.

Age	31 ± 8
Sex (no. of patients)	
M	8
F	2
FEV_1 (% of predicted value)[a]	62 ± 27
FVC (% of predicted value)[b]	83 ± 23
CFTR genotype (no. of patients)	
F508del homozygous	7
Other	2
Unknown	1

[a] FEV_1 is forced expiratory volume in one second.

[b] FVC is forced vital capacity.

FEV_1 and FVC are reported as percent of predicted value for a typical individual.

Predicted value is a function of age, sex, and height.

Age, FEV_1, and FVC values are mean ± SD.

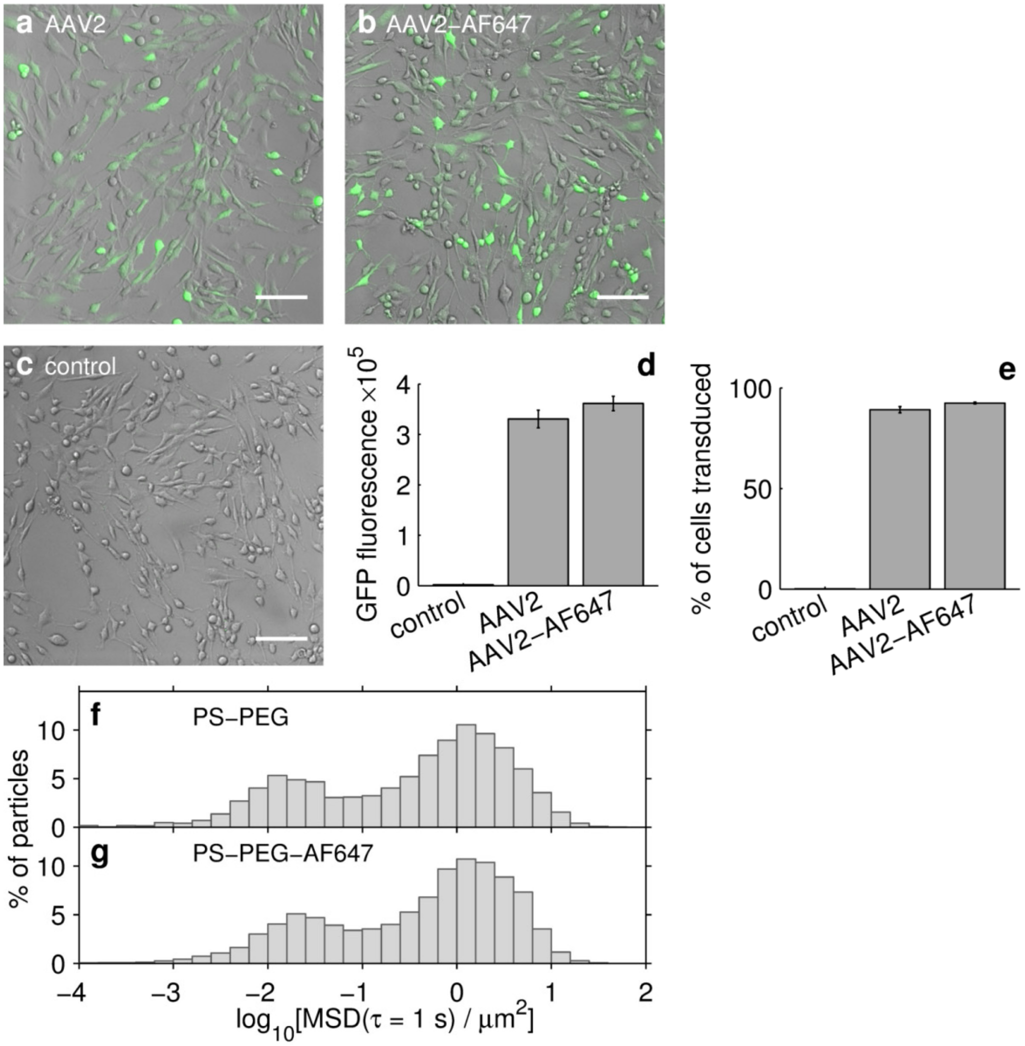

Figure 4.1. Effect of AlexaFluor 647 (AF647) dye labeling on AAV transduction in BEAS-2B cells, and on nanoparticle transport in cystic fibrosis (CF) sputum.
(a-d) BEAS-2B cells transduced (a) with AAV2 or (b) with AF647-labeled AAV2 (AAV2-AF647) are compared to (c) untreated control cells. The AAV packaged a GFP reporter gene; green indicates GFP expression. Scale bars represent 100 μm. (d-e) Flow cytometry comparing GFP expression in BEAS-2B cells transduced with AAV2 vs. AAV2-AF647. Results shown are (d) mean cell fluorescence, in arbitrary units, and (e) percent of cells transduced. Error bars denote standard error of the mean (n = 3). The

difference in transduction between AAV2 and AAV2-AF647 is not statistically significant. (f-g) Multiple particle tracking in CF sputum samples of (f) 100 nm PS-PEG particles vs. (g) 100 nm PS-PEG particles labeled with AF647 (PS-PEG-AF647). Graphs show distribution of individual particles' mean squared displacement (MSD) at a time scale of 1 s. Data represents 6 sputum samples, with on average >1500 particles of each type tracked per sample.

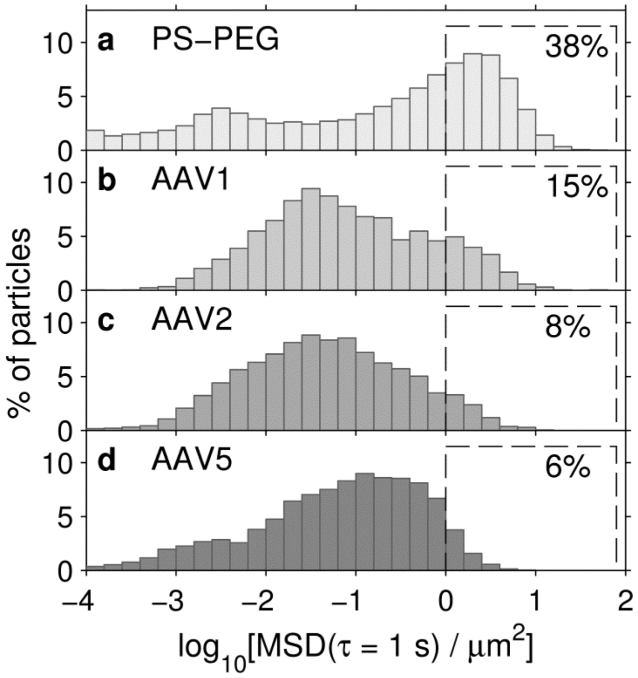

Figure 4.2. Transport in CF sputum samples of AAV1, AAV2, and AAV5, compared to 100 nm PS-PEG control particles.

Distribution of individual particle MSD values at a time scale of 1 s for (a) 100 nm PS-PEG particles, (b) AAV1, (c) AAV2, and (d) AAV5. Data represents the average of 10 sputum samples, with each sample equally weighted, and with on average >500 particles of each type tracked per sample. Percentage of particles that move rapidly, defined as $\log_{10}$MSD ≥ 0 at a time scale of 1 s, is shown for each particle type (dashed boxes).

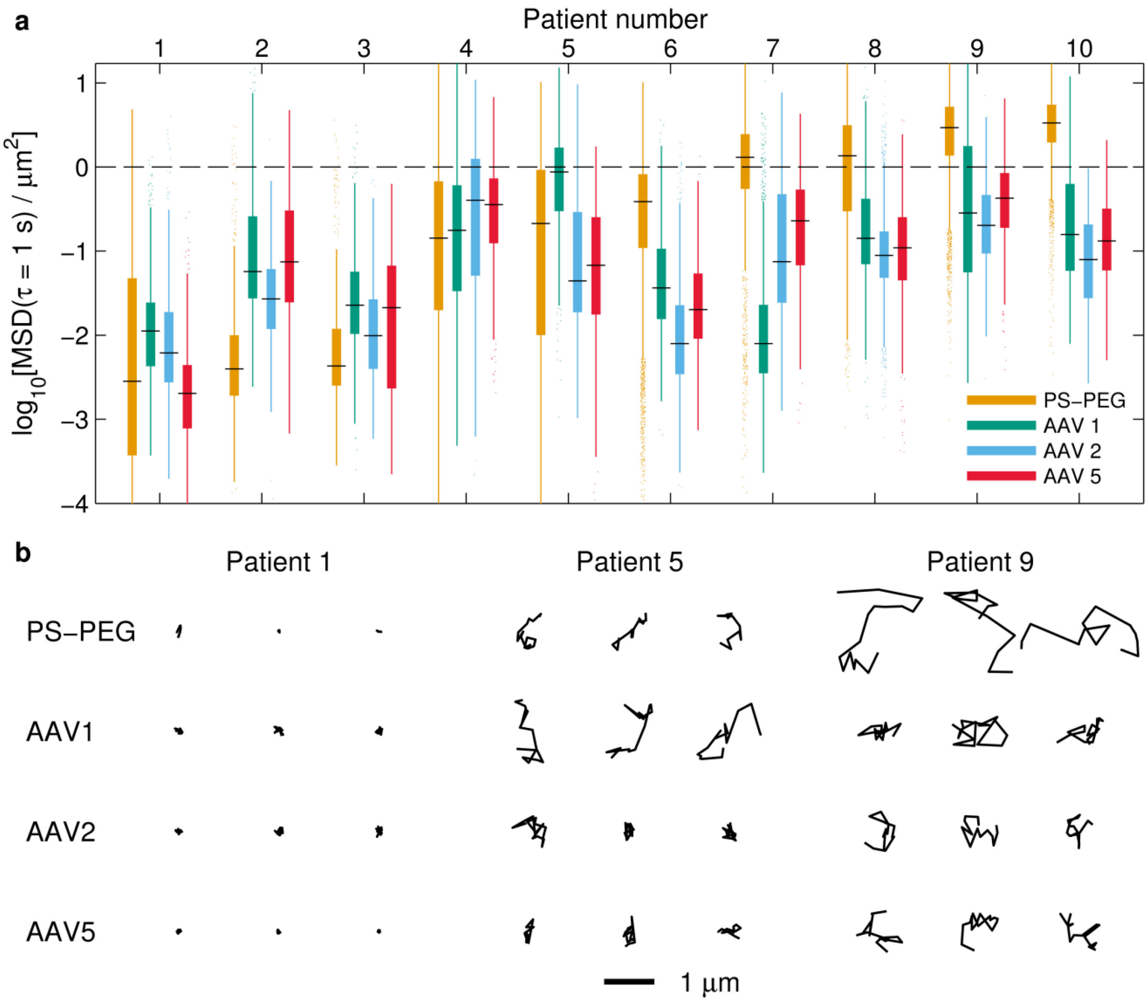

Figure 4.3. Patient-to-patient variation in AAV transport.

(a) Box-and-whisker plots of MSD values (at a time scale of 1 s) of AAV1, AAV2, AAV5, and 100 nm PS-PEG control particles in sputum samples from 10 CF patients. Maximum whisker length is 1.5 times the interquartile range; outliers are shown as dots. Patients are numbered in ascending order according to the median MSD of 100 nm PS-PEG particles in their sputum sample. The dashed line at $\log_{10}\mathrm{MSD} = 0$ is a visual aid to emphasize fast-moving particles, which we define as $\log_{10}\mathrm{MSD} \geq 0$ at a time scale of 1 s. (b) Representative trajectories of AAV1, AAV2, AAV5, and 100 nm PS-PEG control nanoparticles in sputum samples from 3 of the aforementioned 10 CF patients. Trajectories show 1 s of motion. The MSDs of the trajectories presented are within the middle 50 percentile for the given patient sample and particle or virus type.

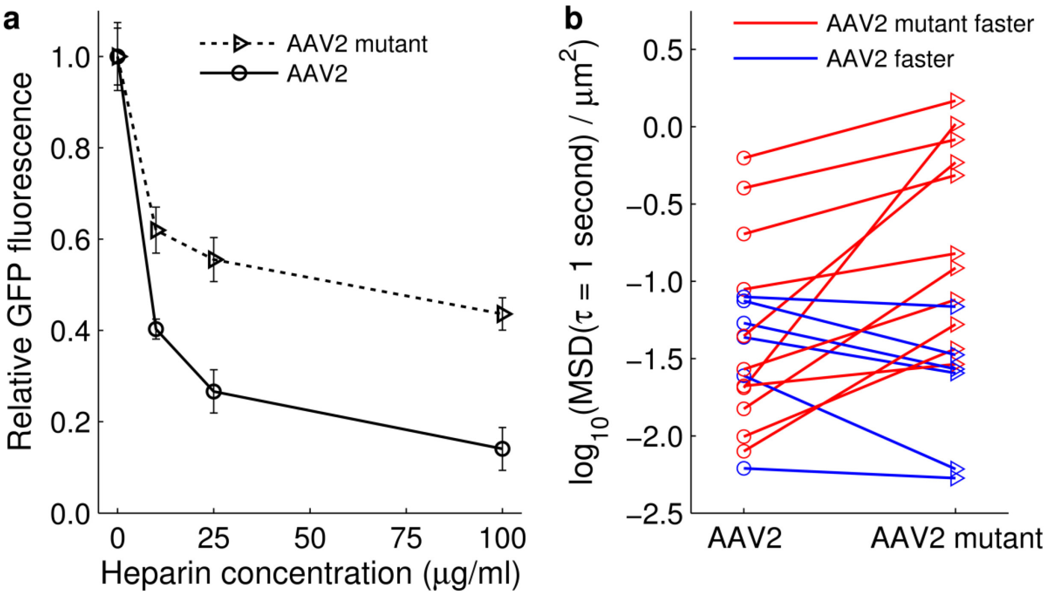

Figure 4.4. Effect of mutation in AAV2 heparin-binding domain.

a) Effect of soluble heparin on transduction of BEAS-2B cells by AAV2 vs. AAV2 mutant, which was engineered to reduce heparin binding. GFP expression by transduced cells was measured by flow cytometry. Values shown are mean cell fluorescence, relative to GFP expression in the absence of soluble heparin, for the respective AAV serotype. Error bars indicate standard error of the mean ($n \geq 3$). Difference is statistically significant ($p < 0.01$) at 10, 25, and 100 μg/mL. (b) Transport in 17 CF sputum samples of AAV2 vs. AAV2 mutant. Each marker represents the median MSD at a timescale of 1 s in one patient sample. Lines connect pairs of data from the same patient's sample. Difference is statistically significant ($p < 0.01$). See methods section for details on statistics.

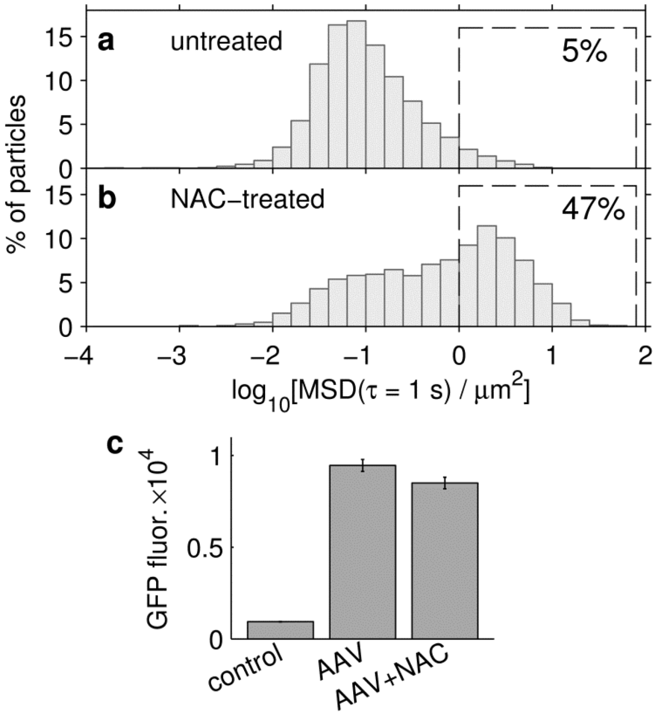

Figure 4.5. Effect of mucolytic agent N-acetylcysteine (NAC) on AAV1 transport in CF sputum, and on AAV1 transduction in BEAS-2B cells.

(a-b) Multiple particle tracking of AAV1 in CF sputum samples either (a) untreated or (b) pre-treated with 5 mM NAC. Graphs show distribution of individual particles' MSDs at a time scale of 1 s. Data represents 5 sputum samples, with on average >900 AAV particles tracked per sample. Percentage of particles that move rapidly, defined as $\log_{10}$MSD ≥ 0 at a time scale of 1 s, is shown for both conditions (dashed boxes). The sputum samples used for the NAC study were different than the sputum samples used for Figures 4.2 and 4.3, and thus the percentage of fast AAV1 particles differs between Figures 4.2b and 4.5a. (c) Effect of 5 mM NAC in the cell culture media on AAV1 transduction of BEAS-2B cells. Results show mean cell GFP fluorescence, measured by flow cytometry, in arbitrary units. Error bars represent standard error of the mean (p = 0.027, n = 8).

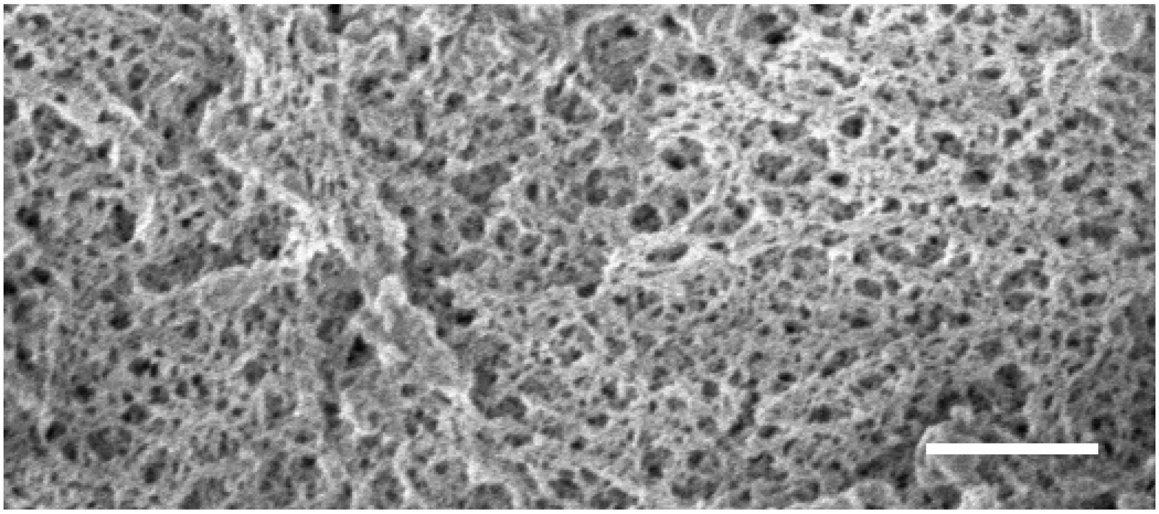

Figure 4.6. (Supplementary) Scanning electron micrograph of CF sputum.

Scale bar is 1 um.

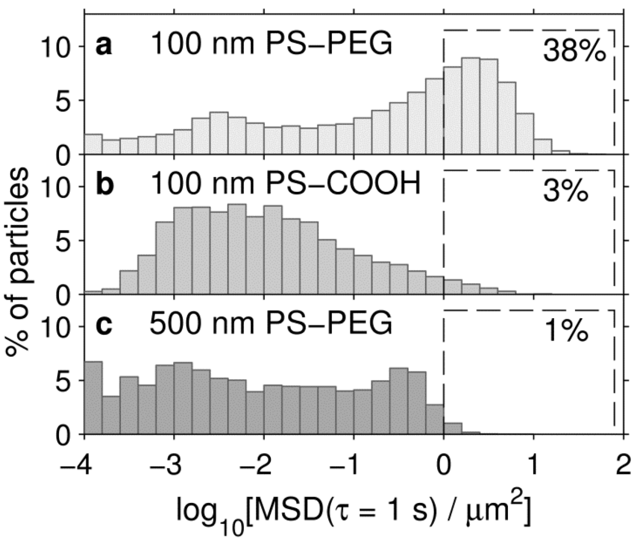

Figure 4.7. (Supplementary) Transport of polymeric nanoparticles in CF sputum. Distribution of individual particle mean squared displacements at a time scale of 1 s for (a) 100 nm PS-PEG, (b) 100 nm PS-COOH, and (c) 500 nm PS-PEG. Data is from the same 10 sputum samples as shown in Fig 2. Data represents the average of the 10 sputum samples, with each sample equally weighted. Percentage of particles that move rapidly, defined as $\log_{10}\mathrm{MSD} \geq 0$ at a time scale of 1 s, is shown for each particle type (dashed boxes).

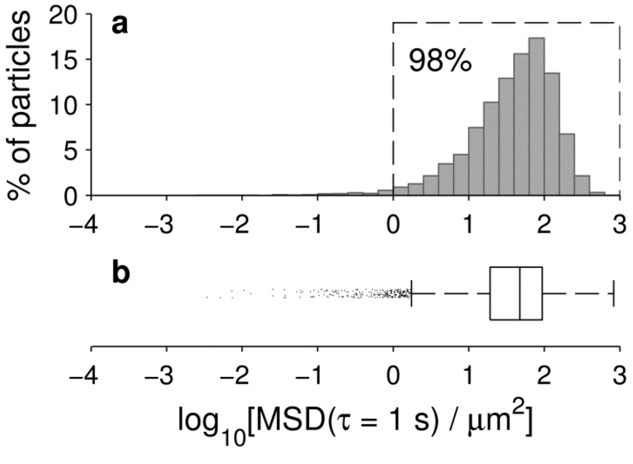

Figure 4.8. (Supplementary) Diffusion of AAV in water.

(a) Distribution of individual particle MSD values at a time scale of 1 s for AAV diffusing in water. This data was generated by simulating the random walks[39] of 10,000 particles of diameter 25 nm in 20 ºC water, with each trajectory 1 s long. Percentage of particles that move rapidly, defined as $\log_{10}$MSD ≥ 0 at a time scale of 1 s, is shown (dashed boxes). (b) The same data, shown as a box-and-whisker plot. Maximum whisker length is 1.5 times the interquartile range; outliers are shown as dots.

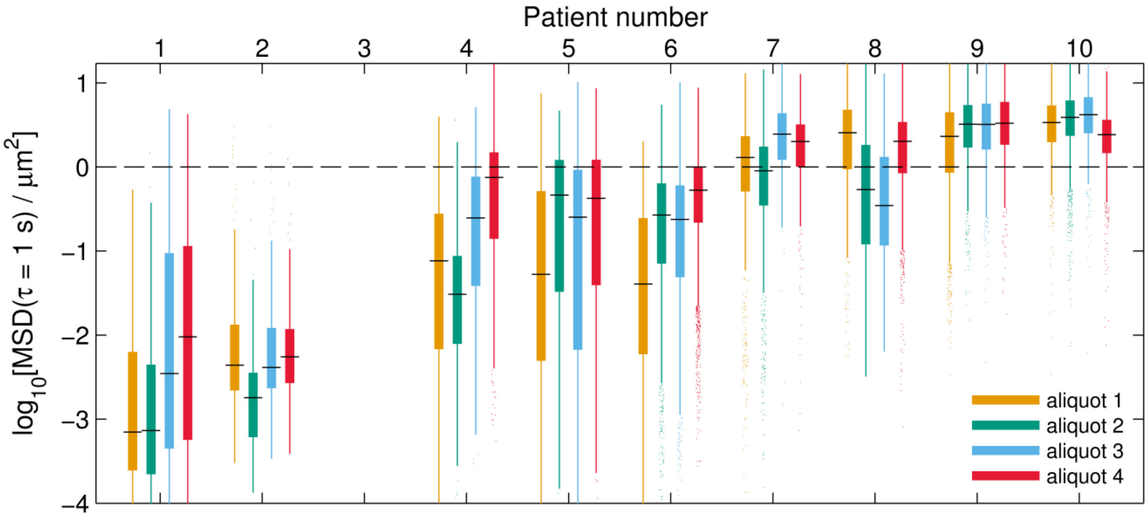

Figure 4.9. (Supplementary) Intra- and inter- sputum sample heterogeneity. Box-and-whisker plots of MSD values (at a time scale of 1 s) of 100 nm PS-PEG particles in four aliquots from each of nine CF patient sputum samples. These are the same patient samples as in Figure 4.3. We were unable to collect the data for patient 3. Maximum whisker length is 1.5 times the interquartile range; outliers are shown as dots. The dashed line at $\log_{10}$MSD = 0 is a visual aid to emphasize fast-moving particles, which we define as $\log_{10}\text{MSD} \geq 0$ at a time scale of 1 s. The 100 nm PS-PEG data shown in Figure 4.3 is the aggregate of the data from the four aliquots from each sample shown here.

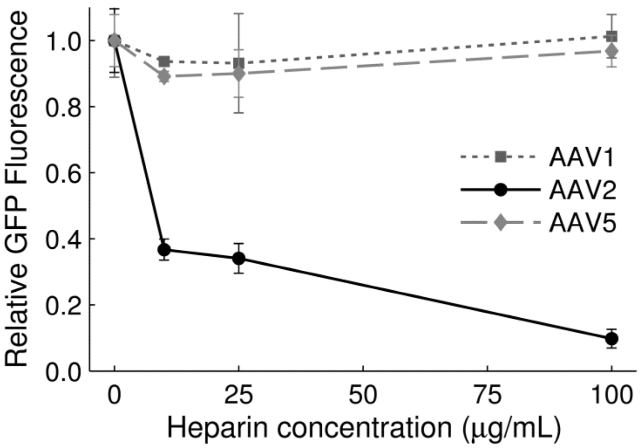

Figure 4.10. (Supplementary) Heparin-binding assay.

Effect of soluble heparin on transduction of BEAS-2B cells by AAV1, AAV2, and AAV5. GFP expression was measured by flow cytometry. Values shown are relative to GFP expression in the absence of soluble heparin for the respective AAV serotype. Error bars indicate standard error of the mean (n = 3).

5. CONCLUSION AND FUTURE OUTLOOK

5.1. Conclusion

In this dissertation, we used nanoparticles to probe the microstructure of human respiratory mucus and CF sputum, and we determined design criteria for nanomedicine capable of overcoming the lung mucus barrier. We discovered that 200 nm particles and smaller can efficiently penetrate lung mucus if the particles have minimally-adhesive surfaces. For polymeric nanoparticles, we achieved this by densely coating the particle surface with polyethylene glycol, a hydrophilic polymer widely used in medical and household products. Furthermore, we discovered that CF sputum is a tenacious barrier to AAV gene vectors, and this barrier likely contributed to the disappointing results of the six CF clinical trials that used AAV2. We found that modifying the virus surface to reduce adhesion improved its transport, as did chemically modulating the mucus structure itself. These findings lay the groundwork for further studies on diffusion of novel nanoparticles and viral vectors in lung mucus. Such studies will be critical to the development of efficacious nanomedicines for cystic fibrosis and other lung diseases.

5.2. Next steps

One strength of this work is that we used freshly collected human mucus samples, rather than reconstituted mucins, frozen specimens, or (non-human) animal mucus. This allowed us to more closely mimic the *in vivo* mucus barrier. However, our experimental system did not incorporate the effects of the pericilary layer or ciliary activity on drug and gene delivery to the lungs. This would be worthwhile to study via complementary techniques, such as tracking particles on mucus-secreting human primary cells cultured at the air-liquid interface.

In the CF sputum studies, intra-sample variation poses a challenge when comparing transport rates of multiple AAV serotypes or particle types tracked in different sputum aliquots. One way to address this challenge is to test large numbers of patient samples, as in Chapter 4. In designing future experiments, a rigorous assessment of power and sample size would be valuable. Another approach would be to label particles with different colors of fluorophores so they can be imaged in the same field of view. We used this approach for polystyrene particles, but for AAV we were only able to image the virus when it was labeled with dark red dye, as autofluorescence overwhelmed the signal when green or red fluorescent dyes were used. New labeling protocols may yet permit AAV to be brightly labeled in various colors. Finally, more careful sputum sample collection or experimental techniques may reduce aliquot-to-aliquot variation.

The results in this thesis suggest that in future CF clinical trials, patients should try to clear their lungs of sputum to the greatest extent possible prior to delivery of the gene vector. This may involve hypertonic saline, mucolytics, and chest physical therapy, all of which are routinely used in CF care. On a related note, another valuable lab study would be to follow patients over time and track gene vector motion in the patients' sputum at multiple time points. This could identify if there are times (e.g., seasonal or following treatment of an exacerbation) when a patient's sputum would be most permissive to gene vector diffusion. Other adjuvants that may enhance AAV penetration in sputum are also worth exploring. For instance, pre-treatment of sputum with sialidase (neuraminidase), which catalyzes hydrolysis of terminal sialic acids, may enhance the transport of AAV1 and AAV5, which bind to sialic acids.

5.3. Future outlook

5.3.1. Advanced microscopy techniques for particle tracking

Recent years have seen exciting innovations in light microscopy, many of which can be harnessed for improved particle tracking. Examples include microscope configurations that reduce background fluorescence and technologies that enable tracking in three dimensions (3D). Although these techniques often require custom instrumentation, some are already commercially available.

Light sheet fluorescence microscopy, also called selective plane illumination microscopy, has been attracting increasing interest recently as a technique to achieve reduced background fluorescence when imaging deep in large biological specimens.[122] This technique requires two objective lenses oriented orthogonally to each other. One objective is used to form a thin light sheet, which illuminates only a narrow plane of the specimen, and thus background fluorescence is reduced. The other objective, perpendicular to the light sheet, is used for detection. Light sheet microscopy can thus achieve optical sectioning, similar to confocal microscopy, but with less photobleaching and faster acquisition rates. A number of recent papers report improved signal-to-noise ratio, and good spatial and temporal resolution, using light sheet microscopy-based particle tracking.[123-126]

Typically, particles are only tracked in the two lateral dimensions (x and y). A range of approaches now exist for also localizing particles in the axial (z) dimension to obtain 3D trajectories, which are useful for studying anisotropic motion.[31,127] One approach is to collect z-stacks with confocal microscopy, but even with a spinning disk confocal microscope, the temporal resolution is insufficient for tracking fast particles. A second approach is to track a single particle at a time, keeping it in focus as it moves by adjusting the height of the stage or the objective lens using a feedback system.[127-129] A third class of approaches exploits changes in the particle image as the particle goes in and out of focus: A fluorescent particle in focus appears as a compact Gaussian spot, whereas diffraction rings become visible when the particle lies more than a few hundred nanometers from the focal plane. The particle image thus encodes information about the particle position in z. Even with a standard microscope, this information may be used to approximate the height of the particle.[2,37] To obtain better precision in z, a number of microscope configurations have been invented to engineer the point spread function so that the particle image varies strongly, and in a predictable way, as the particle distance from the focal plane varies. This can be accomplished by placing additional optical elements, such as a cylindrical lens, in the light path.[130-132] Alternatively, the microscope can be configured to image multiple planes of the specimen at once, from which the particle position in z can be calculated.[133-135]

5.3.2. Future use of particle tracking in drug and gene delivery research

The approaches used in this thesis are broadly applicable to drug and gene delivery research. Nanoparticles hold great promise as vectors for efficacious drug and gene delivery, but they encounter numerous barriers in the body prior to reaching their delivery targets. Particle tracking is a powerful technique for characterizing the behavior of nanoparticles and how effectively they overcome extracellular and cellular barriers. Thus, future applications of particle tracking in drug and gene delivery research are nearly as broad as the field of nanomedicine itself. Looking ahead, we envision the implementation of high-throughput particle tracking studies to test libraries of nanoparticle formulations in biological samples of interest, such as blood, mucus, or tissue. Such a screening technique will allow for rapid identification of nanoparticle formulations that are likely to exhibit favorable *in vivo* delivery and warrant further development. Intravital particle tracking, which is just starting to become possible thanks to advances in imaging techniques, may also revolutionize drug and gene delivery research. The ability to directly observe the journey of a nanoparticle *in vivo* will provide invaluable insight for predicting therapeutic efficacy.

APPENDIX: AUTOMATED PARTICLE TRACKING CODE IN MATLAB

This particle tracking code uses the algorithm of Crocker and Grier,[2] which was originally written in the IDL language. Some functions were based on earlier MATLAB versions by Daniel Blair, Eric Dufresne, and Maria Kilfoil. The code consists of one main script, where the user inputs a few required parameters, and function files that the user does not need to modify. Explanatory comments in the code are colored green.

Two user-input parameters are especially important. They are as follows:

1. maxdisp: The largest distance (in pixels) that a particle could travel from one frame to the next. It must be less than the mean spacing between particles. This value can be estimated by scrolling through the movie and observing the frame-to-frame jumps.
2. lobject: The diameter of the particles in pixels. This number should be just large enough to capture the whole particle.

The algorithm is described in greater detail in Chapter 2. In brief, the code does the following:

1. Load movie.
2. Discard bad regions of movie (such as debris or aggregates) if necessary.
3. Process image using bandpass filter.
4. Identify local maxima, which are initial estimates of candidate particle positions.
5. Refine position estimates by calculating the particles’ intensity-weighted centroids.
6. Discard spurious particles, and keep real ones, based on their size, brightness, and eccentricity.
7. Link x and y positions over time into trajectories.
8. Calculate MSDs.

Main program

```
clear; clc; close all;

% Purpose: Front-end/interface for automated particle tracking. User sets
% parameters and runs code from here. This file calls functions to input the
% movies, process them, and output the results.
%
% The tracking algorithm implemented here is from Crocker and Grier
% (J Coll Interf Sci, 1996). Some parts of the code were adapted from Blair
% and Dufresne and from Kilfoil.
%
% Benjamin Schuster, JHU, 2012-2014.

%%%%%%%%%%%%%%%%%%%%%%%%%%%%%%%%%%%%%%%%%%%%%%%%%%%%%%%%%%%%%%%%%%%%%%%%
% User input
%%%%%%%%%%%%%%%%%%%%%%%%%%%%%%%%%%%%%%%%%%%%%%%%%%%%%%%%%%%%%%%%%%%%%%%%

% User input - directory and movie extension
dir = 'C:\Users\Benjamin\Desktop\MPT in agarose';
ext = '.tif'; % for grayscale .tif videos from fluorescence microscopy
% ext = '.mov'; % for 8-bit RGB avi files from transmitted light microscopy

% User input - parameters for each group of movies (ex, different particle types)
% The code can be run on 1 or multiple groups of movies. Simplest to just
% do one group at a time.
numGroups = 1;
groupinfo(1).group = '20130802 s2 500'; %base name of movies in group
groupinfo(1).spacer = ' '; %space or other character between group name and movie number
groupinfo(1).nMovies = 2; %# of movies in group; movies must be labeled sequentially starting at 1
groupinfo(1).lobject = 9; %approx size of particle in pixels - must be odd, preferably >= 7
groupinfo(1).maxdisp = 4; %max displacement of particle from one frame to next
groupinfo(1).startframe = [1 5]; %first frame to track. one # per movie, separated by commas or spaces.
groupinfo(1).stopframe = [50 100]; %last frame to track. one # per movie, separated by commas or spaces.

% User input - camera frame rate.
% Note: The code assumes all the movies being processed at a time are at
% the same frame rate.
fpers_user = 25; %Hz

% User input - tracking parameters
% Recommendation: Set min_frames low (ex 10) for now, and during post-processing
% you can set it higher if desired
memory_nframes = 3; %number of consecutive frames a particle can go out of view and be tracked
% as the same particle
min_frames = 15; % eliminate trajectories with fewer than this number of frames

% User input - microscope conversion factor
scope_conv = 0.2457; %um/pixel, for Hanes Lab AxioObserver 100x objective

%%%%%%%%%%%%%%%%%%%%%%%%%%%%%%%%%%%%%%%%%%%%%%%%%%%%%%%%%%%%%%%%%%%%%%%%
% Optional user input
%%%%%%%%%%%%%%%%%%%%%%%%%%%%%%%%%%%%%%%%%%%%%%%%%%%%%%%%%%%%%%%%%%%%%%%%

% Bandpass filter parameters
```

```
lnoise = 1; %almost always keep this at 1

% Thresholding/particle discrimination method
% method = 1 for method of Crocker and Grier, using particle "mass,"
%  radius, and eccentricity. Slower but more sensitive method. Set for
%  each movie. Recommended.
% method = 2 for simple thresholding method, from Blair and Dufresne's
%  MATLAB tracking code. Faster, but less flexible and sensitive.
% method = 3 for time-saving method : set the parameters for the first movie
%  using the Crocker-Grier approach, then use those settings for all the
%  movies in a group.
particleDiscriminationMethod = 1;

% If particleDiscriminationMethod is 1 or 3, require particle candidates to
% be in upper cut_percentile percentile of brightness. This should be
% large enough that you don't exclude any true particles. But too large
% and you waste time calculating centroids of noise spots. In my experience,
% 0.05 is more than large enough for most movies. Even 0.01 fine for many
% movies. (Note: Crocker and Grier paper used 0.3).
cut_percentile = 0.03;

% format of output movie
%movieprofile = 'MPEG-4'; %Compressed MPEG-4 file (Windows 7 only) - small file, lower quality
movieprofile = 'Uncompressed AVI'; %Uncompressed AVI file - large file, high quality

% display output movie
movie_display = 1; % display the output movie as it's written. Note: may capture screensaver if it turns on!
% movie_display = 0; % does not display the output movies as it's written. But it's still saved to disk.

%%%%%%%%%%%%%%%%%%%%%%%%%%%%%%%%%%%%%%%%%%%%%%%%%%%%%%%%%%%%%%%%%%%%%
% User should not adjust code beyond here.
%%%%%%%%%%%%%%%%%%%%%%%%%%%%%%%%%%%%%%%%%%%%%%%%%%%%%%%%%%%%%%%%%%%%%

% display current time
disp(['Starting time: ' datestr(now)])

%%%%%%%%%%%%%%%%%%%%%%%%%%%%%%%%%%%%%%%%%%%%%%%%%%%%%%%%%%%%%%%%%%%%%
% Load movie info
%%%%%%%%%%%%%%%%%%%%%%%%%%%%%%%%%%%%%%%%%%%%%%%%%%%%%%%%%%%%%%%%%%%%%

% data structures for storing info used in processing the movies
maxNumMovies = 0;
for gp = 1:numGroups
    if groupinfo(gp).nMovies > maxNumMovies
        maxNumMovies = groupinfo(gp).nMovies;
    end
end
filenames = cell(numGroups,maxNumMovies);
movieInfos = cell(numGroups,maxNumMovies);
numRgns2Exclude = zeros(numGroups,maxNumMovies);
roiVerticesX = cell(numGroups,maxNumMovies);
roiVerticesY = cell(numGroups,maxNumMovies);
InvertedMasks = cell(numGroups,maxNumMovies);
thresholds = zeros(numGroups,maxNumMovies);
poly_verts = cell(numGroups,maxNumMovies);
eccen_cuts = zeros(numGroups,maxNumMovies);
```

```
% Load movie info, select regions to exclude, and choose threshold
% Reason for having a separate loop for this, rather than combining with
% the main feature finding and tracking loop: If there are any problems
% with loading or removing bad regions from one of the later movies in a
% group, you indentify that problem before doing all the tracking on the
% earlier movies.
for gp = 1:numGroups

    group = groupinfo(gp).group;
    spacer = groupinfo(gp).spacer;
    numMovies = groupinfo(gp).nMovies;
    lobject = groupinfo(gp).lobject;

    for mvnum = 1:numMovies

        startf =  groupinfo(gp).startframe(mvnum);
        stopf = groupinfo(gp).stopframe(mvnum);

        %load movie info
        [filename,movieInfo,fpers] = loadMovieInfo_dissertation(dir,group,spacer,mvnum,ext,fpers_user);
        filenames{gp,mvnum} = filename;
        movieInfos{gp,mvnum} = movieInfo;

        %choose regions to exclude, such as cells or aggregated particles that cause erroneous tracking
        [nRgn2Exclude,xVert,yVert,invertedMask,im1,im1bp] = ...
              regions2exclude_dissertation(movieInfo,filename,lnoise,lobject,ext,startf,stopf);
        numRgns2Exclude(gp,mvnum) = nRgn2Exclude;
        roiVerticesX{gp,mvnum} = xVert;
        roiVerticesY{gp,mvnum} = yVert;
        InvertedMasks{gp,mvnum} = invertedMask;

        %threshhold
        % In method 1 and 3, thresholding is a preliminary step, further refinement later
        % In method 2, this is how to select background from noise
        if particleDiscriminationMethod == 1 || particleDiscriminationMethod == 3
            s = sort(im1bp(:),'descend');  % thresholding based on first frame; could change to last frame
            [dim1,dim2] = size(im1bp);
            cut_index = round(dim1*dim2*cut_percentile);
            thresholds(gp,mvnum) = s(cut_index);
        elseif particleDiscriminationMethod == 2
            thresholds(gp,mvnum) =
simplethresh_dissertation(filename,nRgn2Exclude,xVert,yVert,im1,im1bp);
        end

    end
end
disp('Movie information successfully loaded.')
close all

% setting for one of the output figures
scrnsize = get(0,'ScreenSize');
figpos1 = [100 100 1000 500];
if (figpos1(1)+figpos1(3))>scrnsize(3) || (figpos1(2)+figpos1(4))>scrnsize(4)
    figpos1 = [0 0 .5*scrnsize(3) .5*scrnsize(4)];
end
```

```
%%%%%%%%%%%%%%%%%%%%%%%%%%%%%%%%%%%%%%%%%%%%%%%%%%%%%%%%%%%%%%%%%%%%%%
% Do particle detection and tracking
%%%%%%%%%%%%%%%%%%%%%%%%%%%%%%%%%%%%%%%%%%%%%%%%%%%%%%%%%%%%%%%%%%%%%%

lastline = zeros(numGroups,maxNumMovies);
for gp = 1:numGroups % loop over the groups
    group = groupinfo(gp).group;
    numMovies = groupinfo(gp).nMovies;

    %particle identification and tracking parameters
    lobject = groupinfo(gp).lobject;
    pkfindsz = lobject;
    cntrdsz = lobject;
    %Blair and Dufresne recommended cntrdsz = lobject+2, but this could cause
    %a problem where the brightest pixel is at the edge, not the center, of
    %the ROI for calculating the centroid when there are two particles close
    %together or if there are diffraction rings.
    maxdisp = groupinfo(gp).maxdisp;

    %structring element for imdilate, used in pkfnd
    SE = strel('disk', ceil(pkfindsz/2)); % input into strel is radius of structuring element.
    %SE = strel('disk', ceil(pkfindsz/2),0) % the 0 gives you an exact disk
    %rather than an approximation, but it makes imdilate a bit slower

    %cell arrays for storing the data
    SNRCell = cell(numMovies,1); % for storing signal-to-noise ratio
    TrajGroupCell = cell(numMovies,1); % for storing all trajectories from 1 group of movies
    TrajStart0GroupCell = cell(numMovies,1); % as above, but trajectory position
    % starts at 0 (i.e. displacements relative to initial position)

    for mvnum = 1:numMovies % loop over all the movies in a group
        filename = filenames{gp,mvnum};
        display([filename ' - analyzing'])
        movieInfo = movieInfos{gp,mvnum};
        thresh = thresholds(gp,mvnum);

        %first and last frames of the movie to analyze
        startf =  groupinfo(gp).startframe(mvnum);
        stopf = groupinfo(gp).stopframe(mvnum);
        num_images = stopf-startf+1;

        if strcmp(ext,'.mov')
            movieobj = VideoReader(filename);
        end

        cntAllcell = cell(num_images,1); %for storing particle centroids and data (brightness etc.)

        noisemean = zeros(1,num_images);
        noisestd = zeros(1,num_images);
        signal = zeros(1,num_images);

        % Locate particles
        tic %start timing
        for i = startf:stopf % loop over desired frames in a movie
```

```
      %Load in one frame.
      if strcmp(ext,'.tif')
        im = imread(filename, 'tif', i, 'Info', movieInfo); %Info speeds imread for multi-image tiff
      elseif strcmp(ext,'.mov')
        moviecdata = read(movieobj,i);
        im = 256*3 - sum(moviecdata,3);
      end
      im = double(im); % im needs to be a double for convolution in bpass

      %Spatial bandpass filter smooths the image and subtracts the background off
      imbp = bpass_dissertation(im,lnoise,lobject);

      %Remove excluded regions, if any
      imbp = imbp.*InvertedMasks{gp,mvnum};

      %Identify the candidate particle locations to pixel-level accuracy.
      [pk,noisemean(i-startf+1),noisestd(i-startf+1)]=pkfnd_dissertation(im,imbp,thresh,SE);

      % Refine location estimate by calculating particle centroid.
      cnt = cntrd_dissertation(imbp,pk,cntrdsz);
      % Each row in cnt stores the data on one particle (spot).
      % cnt has 5 columns. They are: 1. x-coordinates, 2. y-coordinates,
      % 3. brightnesses, 4. square of radius of gyration, 5. eccentricity

      % In 6th column, add frame number with respect to the first frame
      % tracked. I.e., if we're tracking frames 10 and onwards, frame 10
      % is the first frame tracked and will be recorded here with a
      % "frame stamp" of 1. So frame_stamp = trueframe#-startf+1
      if numel(cnt) > 0
        cntAllcell{i-startf+1} = [cnt (i-startf+1)*ones(size(cnt,1),1)];
      end

      mo = mod(i,25);
      if mo == 0
        disp(['centroid finding - completed frame ' num2str(i)])
      end

    end
    cntAll = cell2mat(cntAllcell);
    toc %finish timing the centroid finding

    % discriminate true particles from noise
    if particleDiscriminationMethod == 1
      [pos,eccen_cuts(gp,mvnum)] =
particleDiscrimination_dissertation(num_images,cntAll,im,filename,lobject);
    elseif particleDiscriminationMethod == 2
      pos=cntAll;
    elseif particleDiscriminationMethod == 3
      if gp == 1 && mvnum == 1
        [pos,brightness_cut,eccen_cut] = ...
              batchParticleDiscrimination_dissertation(num_images,cntAll,im,filename,lobject);
      else
        rows2keep = cntAll(:,3) >= brightness_cut;
        cntAllKeep = cntAll(rows2keep,:);
        rows2keep = cntAllKeep(:,5) <= eccen_cut;
        disp([num2str(size(cntAllKeep,1)) ' spots kept'])
```

```
        pos = cntAllKeep(rows2keep,:);
    end
end

% Calculating approximate signal-to-noise ratio (Savin and Doyle,
% Biophys J, 2005)
disp('Calculating approximate signal-to-noise ratio')
for i = startf:stopf
    pix = round(pos(pos(:,6) == (i-startf+1),1:2)); % bright pixels
    %Load in one frame
    if strcmp(ext,'.tif')
        im = imread(filename, 'tif',i, 'Info', movieInfo); %Info speeds imread for multi-image tiff
    elseif strcmp(ext,'.mov')
        moviecdata = read(movieobj,i);
        im = 256*3 - sum(moviecdata,3);
    end
    im = double(im);
    idx = sub2ind(size(im), pix(:,2), pix(:,1));
    signal(i-startf+1) = mean(im(idx));
end
SNR = (signal-noisemean)./noisestd; %note, there are other definitions of SNR
figure
plot(startf:stopf,SNR)
xlabel('frame number')
ylabel('signal/noise')
title('Approximate signal-to-noise raio')
set(gca,'YLim',[0 1.1*max(SNR)])
SNRCell{mvnum} = [startf:stopf; SNR]';

% Check for pixel bias, i.e. check for sub-pixel feature location.
% Histograms of the x and y-positions modulo 1 should be flat IF you
% have enough particles and they are not single pixel biased.
f = figure('name','Check for pixel bias. Histograms should be flat if you have sub-pixel localization.');
set(f,'Position',figpos1)
subplot(1,2,1)
hist(mod(pos(:,1),1),20)
ylabel('count')
xlabel('x coordinates modulo 1')
subplot(1,2,2)
hist(mod(pos(:,2),1),20)
ylabel('count')
xlabel('y coordinates modulo 1')
print(f,[filename(1:end-4) ' - pixel bias check.jpg'],'-djpeg')

% Trajectory linking step: connect the list of particle positions into trajectories
tic % begin timing
Traj = mytracker_dissertation(pos,maxdisp,memory_nframes,min_frames);
num_particles = max(Traj(:,1));
disp([num2str(num_particles) ' trajectories'])
toc % end timing

% Compute trajectories with respect to initial position
TrajStart0 = zeros(size(Traj,1),4);
X = NaN(num_images,num_particles); %this will be used for making the trajectory movie
Y = NaN(num_images,num_particles); %this will be used for making the trajectory movie
for j = 1:num_particles
```

```
        rows = find(Traj(:,1)==j);
        frms = Traj(rows,2); %not frms-startf+1, because of how frame numbers are are counted in Traj
        x = Traj(rows,3);
        y = Traj(rows,4);

        X(frms,j) = x;
        Y(frms,j) = y;

        x2 = x - x(1);
        y2 = y - y(1);
        TrajStart0(rows,1) = j;
        TrajStart0(rows,2) = 1:length(x);
        TrajStart0(rows,3) = x2;
        TrajStart0(rows,4) = y2;
    end
    Traj(:,2) = Traj(:,2) + (startf-1); % now that the caclculations are
    % done, add this back so in Traj frame number is absolute, not relative
    % to the first frame tracked. Leave TrajStart0 as is.
    TrajGroupCell{mvnum} = Traj;
    TrajStart0GroupCell{mvnum} = TrajStart0;
    if mvnum == 1
        lastline(gp,mvnum) = size(Traj,1);
    else
        lastline(gp,mvnum) = lastline(gp,mvnum-1) + size(Traj,1);
    end

    % Make movie with trajectories overlayed
    xVert = roiVerticesX{gp,mvnum};
    yVert = roiVerticesY{gp,mvnum};
    nRgn2Exclude = numRgns2Exclude(gp,mvnum);
    tic
    makeTrajectoryMovie_dissertation(filename,ext,movieprofile,
          ...fpers,movie_display,movieInfo,X,Y,xVert,yVert,nRgn2Exclude,startf,stopf);
    toc
    disp(['Movie ' filename ' done'])

end
TrajGroup = cell2mat(TrajGroupCell);
TrajStart0Group = cell2mat(TrajStart0GroupCell);

% calculate the MSD
[TrajProc,Timescale,num_particles,frames] = process_MPT_data_dissertation(TrajStart0Group,fpers);
[MSD,MSDx,MSDy,d_shortest_t,num_displacements] = ...
          calculate_MSD_dissertation(TrajProc,Timescale,num_particles,frames,scope_conv);

%plot the number of displacements as a function of time scale
figure
plot(Timescale,sum(num_displacements,2))
xlabel('time (s)')
ylabel('number of displacements')

% calculate the ensemble MSD - note ensemble averaging isn't
% recommended when there are distinct categories of particles, e.g.
% immobile and mobile, in the same data set
frm_max = size(MSD,1);
meanMSD = zeros(frm_max,1);
```

```
    meanMSDx = zeros(frm_max,1);
    meanMSDy = zeros(frm_max,1);
    for f = 1:frm_max
        meanMSD(f) = mean(MSD(f,~isnan(MSD(f,:)))); % arithmetic mean
        meanMSDx(f) = mean(MSDx(f,~isnan(MSDx(f,:))));
        meanMSDy(f) = mean(MSDy(f,~isnan(MSDy(f,:))));
    end

    % plot the MSD vs. time scale
    f1 = figure;
    set(f1,'Position',figpos1)
    subplot(1,2,1)
    loglog(Timescale,meanMSDx,Timescale,meanMSDy,Timescale,meanMSD);
    legend('MSDx','MSDy','MSD','location','northwest')
    title('ensemble-average MSD (arithmetic mean) - log axes')
    xlabel('Timescale (s)')
    ylabel('<MSD> (\mum^2)')
    subplot(1,2,2)
    plot(Timescale,meanMSDx,Timescale,meanMSDy,Timescale,meanMSD);
    legend('MSDx','MSDy','MSD','location','northwest')
    title('ensemble-average MSD (arithmetic mean) - linear axes')
    xlabel('Timescale (s)')
    ylabel('<MSD> (\mum^2)')
    print(f1,[dir '\' group ' - MSD plot.jpg'],'-djpeg')

    %check that maxdisp is large enough
    f2 = figure;
    hist(d_shortest_t,20)
    xlabel('displacement at shortest time scale (1 frame)')
    ylabel('count')
    title(['Check that maxdisp = ' num2str(maxdisp) ' is large enough'])
    print(f2,[dir '\' group ' - maxdisp check.jpg'],'-djpeg')


%%%%%%%%%%%%%%%%%%%%%%%%%%%%%%%%%%%%%%%%%%%%%%%%%%%
    % export data to Excel - one file for trajectories, another for MSDs
%%%%%%%%%%%%%%%%%%%%%%%%%%%%%%%%%%%%%%%%%%%%%%%%%%%

    group = groupinfo(gp).group;
    spacer = groupinfo(gp).spacer;
    display(['Exporting data to Excel for ' group])

    tic %begin timing hohw long it takes to output the data
    outputfile = [dir '\' group ' - ' num2str(mvnum) ' movies auto tracked - Trajectories.xlsx'];
    xlswrite(outputfile,TrajStart0Group,'Sheet1','A1')
    % Sheet 1 contains the trajectories, one row for each particle position.
    % The columns are 1. particle number 2. frame number
    % 3. x-coordinates, 4. y-coordinates. Here the x and y coordinates are
    % given in pixel units, with respect to the initial particle position.
    TrackingSettings{1,1} = 'tracker driver version';
    TrackingSettings{1,2} = mfilename;
    TrackingSettings{2,1} = 'min_frames';
    TrackingSettings{2,2} = min_frames;
    TrackingSettings{3,1} = 'memory_nframes';
    TrackingSettings{3,2} = memory_nframes;
    TrackingSettings{4,1} = 'maxdisp';
```

```
    TrackingSettings{4,2} = maxdisp;
    TrackingSettings{5,1} = 'lobject';
    TrackingSettings{5,2} = lobject;
    TrackingSettings{6,1} = 'pkfindsz';
    TrackingSettings{6,2} = pkfindsz;
    TrackingSettings{7,1} = 'cntrdsz';
    TrackingSettings{7,2} = cntrdsz;
    TrackingSettings(9,1:2) = {'filename';'last line of trajectories'};
    TrackingSettings(10:(9+numMovies),1) = filenames(gp,:)';
    TrackingSettings(10:(9+numMovies),2) = mat2cell(lastline(gp,:)',ones(numMovies,1));
    xlswrite(outputfile,TrackingSettings,'Sheet2','A1')
    % Sheet 2 contains the tracking settings
    xlswrite(outputfile,TrajGroup,'Sheet3','A1')
    % Sheet 3 contains the trajectories, one row for each particle position.
    % The columns are 1. particle number 2. frame number
    % 3. x-coordinates, 4. y-coordinates, 5. brightnesses, 6. square of
    % radius of gyration, 7. eccentricity. Here the x and y coordinates are
    % in absolute pixel numbers (not with respect to the initial particle
    % position)

    % The next file contains
    % In Sheet 1: Column with timescale (units: s), column with ensemble MSD,
    % blank column, then columns with individual particles MSDs (MSD units: um^2).
    % In Sheet 2: The signal-to-noise ratio for each frame analyzed
    outputfile = [dir '\' group ' - ' num2str(mvnum) ' movies auto tracked - MSD.xlsx'];
    xlswrite(outputfile,[Timescale' meanMSD NaN(length(Timescale),1) MSD],'Sheet1','A1')
    xlswrite(outputfile,cell2mat(SNRCell),'Sheet2','A1')
    toc

end

%display current time
disp(['Ending time: ' datestr(now)])
```

Function for loading videos

```
function [filename,movieInfo,fpers] = loadMovieInfo_dissertation(dir,group,spacer,mvnum,ext,fpers_user)

% Loads the movie information and calculates the frame rate, then checks that
% it agrees with the user-input frame rate.
%
% Benjamin Schuster, JHU, 2012-2014

filename = [dir '\' group spacer num2str(mvnum) ext];
display([filename ' - loading movie information'])

if strcmp(ext,'.tif')

    movieInfo = imfinfo(filename);

    if isfield(movieInfo,'DateTime')
        %frame rate calculation - calculate from movie info
        time1 = str2double(movieInfo(1).DateTime((end-5):end));
        time2 = str2double(movieInfo(2).DateTime((end-5):end));
```

```
        exposureTime = time2 - time1;
        if isnan(exposureTime) %get NaN if hour just changed, so try again
            time1 = str2double(movieInfo(5).DateTime((end-5):end));
            time2 = str2double(movieInfo(6).DateTime((end-5):end));
            exposureTime = time2 - time1;
        end
        fpers = round(1/exposureTime);
        if fpers_user == fpers
            disp(['Calculated and input frame rates agree: ' num2str(fpers) ' Hz'])
        else
            disp(['Frame rate calculated (rounded to whole number): ' num2str(fpers) ' Hz'])
            disp(['Frame rate entered by user: ' num2str(fpers_user) ' Hz'])
            disp('Frame rate discrepancy! Will use calculated frame rate. Please check movie.')
        end
    else
        disp('Cannot calculate frame rate from movie. Will use user-input value.')
        fpers = fpers_user;
    end

elseif strcmp(ext,'.mov')

    movieInfo = VideoReader(filename);

    % nFrames = movieobj.NumberOfFrames;
    % vidHeight = movieobj.Height;
    % vidWidth = movieobj.Width;
    fpers = movieInfo.FrameRate;

end
```

Function for selecting regions of a video to discard

```
function [nRgn2Exclude,xVert,yVert,invertedMask,im1,im1bp] = ...
    regions2exclude_dissertation(movieInfo,filename,lnoise,lobject,ext,startf,stopf)

% This function allows you to avoid tracking certain undesired areas,
% such as debris or aggregates, that can cause erroneous tracking.

% Benjamin Schuster, JHU, 2012-2014

display([filename ' - user input'])

scrnsize = get(0,'ScreenSize');
figpos1 = [200 200 1200 700];
if (figpos1(1)+figpos1(3))>scrnsize(3) || (figpos1(2)+figpos1(4))>scrnsize(4)
    figpos1 = [0 0 .75*scrnsize(3) .75*scrnsize(4)];
end

w = movieInfo(1).Width; %width is number of columns
h = movieInfo(1).Height; %height is number of rows
im = zeros(h,w,4);
imbp = zeros(h,w,4);

%show 4 frames of the movie, raw and bandpassed
```

```
if strcmp(ext,'.mov')
    movieobj = VideoReader(filename);
end
imnums = floor(linspace(startf,stopf,4));
for i = 1:4
    if strcmp(ext,'.tif')
        im(:,:,i) = double(imread(filename, imnums(i),'Info', movieInfo));
    elseif strcmp(ext,'.mov')
        moviecdata = read(movieobj,imnums(i));
        im(:,:,i) = 256*3 - sum(moviecdata,3);
    end
    imbp(:,:,i) = bpass_dissertation(im(:,:,i),lnoise,lobject);
end
fig = figure('name',[filename ': selected raw and bandpassed images']);
set(fig,'Position', figpos1)
ax1 = axes('position',[.04 .55 .2 .35],'units','normalized');
ax2 = axes('position',[.28 .55 .2 .35],'units','normalized');
ax3 = axes('position',[.52 .55 .2 .35],'units','normalized');
ax4 = axes('position',[.76 .55 .2 .35],'units','normalized');
ax5 = axes('position',[.04 .1 .2 .35],'units','normalized');
ax6 = axes('position',[.28 .1 .2 .35],'units','normalized');
ax7 = axes('position',[.52 .1 .2 .35],'units','normalized');
ax8 = axes('position',[.76 .1 .2 .35],'units','normalized');
imagesc(im(:,:,1),'Parent',ax1);
title(['frame ' num2str(imnums(1))],'Parent',ax1)
imagesc(im(:,:,2),'Parent',ax2);
title(['frame ' num2str(imnums(2))],'Parent',ax2)
imagesc(im(:,:,3),'Parent',ax3);
title(['frame ' num2str(imnums(3))],'Parent',ax3)
imagesc(im(:,:,4),'Parent',ax4);
title(['frame ' num2str(imnums(4))],'Parent',ax4)
imagesc(imbp(:,:,1),'Parent',ax5);
title(['bandpass filtered frame ' num2str(imnums(1))],'Parent',ax5)
imagesc(imbp(:,:,2),'Parent',ax6);
title(['bandpass filtered frame ' num2str(imnums(2))],'Parent',ax6)
imagesc(imbp(:,:,3),'Parent',ax7);
title(['bandpass filtered frame ' num2str(imnums(3))],'Parent',ax7)
imagesc(imbp(:,:,4),'Parent',ax8);
title(['bandpass filtered frame ' num2str(imnums(4))],'Parent',ax8)
colormap('gray')

%select regions to exclude, if any
nRgn2Exclude = [];
while isempty(nRgn2Exclude)
    try
        nRgn2Exclude=input('If you wish to exclude regions of the movie, enter the number of regions, else
type 0: ');
    catch ME
        disp(ME.message)
    end
end

im1 = im(:,:,1);
im1bp = imbp(:,:,1);

xVert = cell(1,nRgn2Exclude);
```

```
yVert = cell(1,nRgn2Exclude);

if nRgn2Exclude>0
    ROImask = zeros(h,w,nRgn2Exclude);
    for m=1:nRgn2Exclude;
        close all
        figure('name',[filename ': frame 1'])
        imagesc(im1)
        colormap('gray')
        title('Choose one region to exclude')
        hold on
        for r = 1:m-1
            plot(xVert{r},yVert{r},'r')
        end
        display('Use the polygon tool to create an ROI which you do not want tracked, then double click in
that region.')
        [ROImask(:,:,m),xVert{m},yVert{m}] = roipoly;
    end
    % put all ROI masks into 1 matrix; don't double count overlapping masks
    rgns2remove = sum(ROImask,3)>0;
else
    rgns2remove  = zeros(h,w);
end
close all

invertedMask = 1-rgns2remove ; %inverted mask - these are the pixels to keep
im1bp = im1bp.*invertedMask;
```

Function for discriminating true particles from noise

```
function  [pos,eccen_cut] = particleDiscrimination_dissertation(num_images,cntAll,im,filename,lobject)

% This function is used to discriminate true particles from noise based on
% the particle size, brigthtness (mass), and eccentricity.
%
% Benjamin Schuster, JHU, 2012-2014

close all;

colors = jet(num_images);

scrnsize = get(0,'ScreenSize');

happy = 0;
while happy == 0

    disp([num2str(size(cntAll,1)) ' spots identified'])

    %plot radius vs brightness
    f1 = figure(1);
    set(f1,'Position',[100 (scrnsize(4)-600) 675 500])
    hold on
    for i = 1:num_images,
        rows = find(cntAll(:,6) == i);
        plot(cntAll(rows,3),cntAll(rows,4),'.','color',colors(i,:),'MarkerSize',6)
```

```
end
title('Select true particles')
xlabel('brightness')
ylabel('radius of gyration squared')

% choose points in (brigthness,radius) plane by drawing a polygon
% around them.
disp('Draw a polygon on Figure 1 around the points you would like to keep.')
h = impoly;
poly_vert = getPosition(h);

% determine which points are within the polygon
rows2keep = inpolygon(cntAll(:,3),cntAll(:,4),poly_vert(:,1),poly_vert(:,2));
% only keep those particles
cntAllKeep = cntAll(rows2keep,:);

disp([num2str(size(cntAllKeep,1)) ' spots kept'])

% show the particles identified in the last image
f2 = figure(2);
set(f2,'Position',[100 (scrnsize(4)-600) 675 500])
imagesc(im),colormap('gray')
hold on
lastcnt = cntAllKeep((cntAllKeep(:,6)==num_images),:);

theta = linspace(0,2*pi,50); %thanks to Kilfoil lab's code for this
for c = 1:size(lastcnt,1)
    cx = lastcnt(c,1) + lobject/2*cos(theta);
    cy = lastcnt(c,2) + lobject/2*sin(theta);
    plot(cx,cy,'r-','linewidth',1)
end
title('Particles identified in last frame of movie')
axis square

%plot particle eccentricity vs brightness
f3 = figure(3);
set(f3,'Position',[800 (scrnsize(4)-600) 675 500])
hold on
for i = 1:num_images,
    rows = find(cntAllKeep(:,6) == i);
    plot(cntAllKeep(rows,3),cntAllKeep(rows,5),'.','color',colors(i,:))
end
title('Use eccentricity to exclude noise')
xlabel('brightness')
ylabel('eccentricity')
disp('Draw a polygon on Figure 3 around the points you would like to keep.')

h=impoly;
poly_vert = getPosition(h);
rows2keep = inpolygon(cntAllKeep(:,3),cntAllKeep(:,5),poly_vert(:,1),poly_vert(:,2));
eccen_cut = NaN;

cntAllKeep = cntAllKeep(rows2keep,:);
disp([num2str(size(cntAllKeep,1)) ' spots kept'])

% show the particles identified in the last image
```

```
    f4 = figure(4);
    set(f4,'Position',[800 (scrnsize(4)-600) 675 500])
    imagesc(im),colormap('gray')
    hold on
    lastcnt = cntAllKeep((cntAllKeep(:,6)==num_images),:);
    for c = 1:size(lastcnt,1)
        cx = lastcnt(c,1) + lobject/2*cos(theta);
        cy = lastcnt(c,2) + lobject/2*sin(theta);
        plot(cx,cy,'g-','linewidth',1)
    end
    title('Particles identified in last frame of movie')
    axis square
    title('Particles identified in last frame of movie')

    happy = input('Satisfied with particle discrimination? 1 for yes, 0 for no: ');
    while ~(happy == 0 || happy == 1)
        happy = input('Improper entry. Satisfied with particle discrimination? 1 for yes, 0 for no: ');
    end

    if happy == 0
        close all
    else
        print(f1,[filename(1:end-4) ' - particle detection.jpg'],'-djpeg')
        print(f3,[filename(1:end-4) ' - particle detection2.jpg'],'-djpeg')
    end
end

pos=cntAllKeep;
```

Function for discriminating true particles from noise for a batch of movies

```
function  [pos,brightness_cut,eccen_cut] = ...
    batchParticleDiscrimination_dissertation(num_images,cntAll,im,filename,lobject)

% This function is used to discriminate true particles from noise based on
% the particle size, brigthtness (mass), and eccentricity.
%
% Benjamin Schuster, JHU, 2012

close all;

colors = jet(num_images);

scrnsize = get(0,'ScreenSize');

happy = 0;
while happy == 0

    disp([num2str(size(cntAll,1)) ' spots identified'])

    %plot radius vs brightness
    f1 = figure(1);
    set(f1,'Position',[100 (scrnsize(4)-600) 675 500])
    hold on
    for i = 1:num_images,
```

```
    rows = find(cntAll(:,6) == i);
    plot(cntAll(rows,3),cntAll(rows,4),'.','color',colors(i,:),'MarkerSize',6)
end
title('Select true particles')
xlabel('brightness')
ylabel('radius of gyration squared')

brightness_cut = input('Enter brightness cutoff. Particles with brightness < cutoff will be discarded: ');
rows2keep = cntAll(:,3) >= brightness_cut;
cntAllKeep = cntAll(rows2keep,:);

disp([num2str(size(cntAllKeep,1)) ' spots kept'])

% show the particles identified in the last image
f2 = figure(2);
set(f2,'Position',[100 (scrnsize(4)-600) 675 500])
imagesc(im),colormap('gray')
hold on
lastcnt = cntAllKeep((cntAllKeep(:,6)==num_images),:);

%  plot(lastcnt(:,1),lastcnt(:,2),'ro','MarkerSize',6); %faster
theta = linspace(0,2*pi,50); %thanks to Kilfoil lab's code for this
for c = 1:size(lastcnt,1)
    cx = lastcnt(c,1) + lobject/2*cos(theta);
    cy = lastcnt(c,2) + lobject/2*sin(theta);
    plot(cx,cy,'r-','linewidth',1)
end
title('Particles identified in last frame of movie')
axis square

%plot particle eccentricity vs brightness
f3 = figure(3);
set(f3,'Position',[800 (scrnsize(4)-600) 675 500])
hold on
for i = 1:num_images,
    rows = find(cntAllKeep(:,6) == i);
    plot(cntAllKeep(rows,3),cntAllKeep(rows,5),'.','color',colors(i,:))
end
title('Use eccentricity to exclude noise')
xlabel('brightness')
ylabel('eccentricity')

eccen_cut = input('Enter eccentricity cutoff. Particles with value larger than cutoff will be discarded: ');
if ~(eccen_cut > 0 && eccen_cut <= 1)
    eccen_cut = 0.3;
    disp('Improper entry. Default to eccentricity cutoff of 0.3');
end
rows2keep = cntAllKeep(:,5) <= eccen_cut;
cntAllKeep = cntAllKeep(rows2keep,:);
disp([num2str(size(cntAllKeep,1)) ' spots kept'])

% show the particles identified in the last image
f4 = figure(4);
set(f4,'Position',[800 (scrnsize(4)-600) 675 500])
imagesc(im),colormap('gray')
hold on
```

```
    lastcnt = cntAllKeep((cntAllKeep(:,6)==num_images),:);
    for c = 1:size(lastcnt,1)
        cx = lastcnt(c,1) + lobject/2*cos(theta);
        cy = lastcnt(c,2) + lobject/2*sin(theta);
        plot(cx,cy,'g-','linewidth',1)
    end
    title('Particles identified in last frame of movie')
    axis square
    title('Particles identified in last frame of movie')

    happy = input('Satisfied with particle discrimination? 1 for yes, 0 for no: ');
    while ~(happy == 0 || happy == 1)
        happy = input('Improper entry. 1 for yes, 0 for no: ');
    end

    if happy == 0
        close all
    else
        print(f1,[filename(1:end-4) ' - particle detection.jpg'],'-djpeg')
        print(f3,[filename(1:end-4) ' - particle detection2.jpg'],'-djpeg')

    end
end
pos=cntAllKeep;
```

Function for selecting a threshold to separate foreground and background

```
function threshold = simplethresh_dissertation(filename,nRgn2Exclude,xVert,yVert,im1,im1bp)

% Method for discriminating particles from background noise, using simple
% thresholding.
%
% Benjamin Schuster, JHU, 2012-2014

scrnsize = get(0,'ScreenSize');
figpos1 = [50 550 1500 425];
figpos2 = [50 50 1500 425];
if (figpos1(1)+figpos1(3))>scrnsize(3) || (figpos1(2)+figpos1(4))>scrnsize(4)
    figpos1 = [0 0 .75*scrnsize(3) .4*scrnsize(4)];
    figpos2 = [0 0 .75*scrnsize(3) .4*scrnsize(4)];
end
opengl('software') %helps with the graphical output; otherwise axis labels appear upside-down

%Plot 1, different views to help see appropriate threshold
figure('name',[filename ': Choose tracking threshold based on bandpassed images'])
set(gcf,'Position', figpos1)
ax1 = axes('position',[.04 .1 .2 .8],'units','normalized');
ax2 = axes('position',[.28 .1 .2 .8],'units','normalized');
ax3 = axes('position',[.52 .1 .2 .8],'units','normalized');
ax4 = axes('position',[.76 .1 .2 .8],'units','normalized');
%subplot 1
imagesc(im1,'Parent',ax1),%colormap(ax1,'gray')
title(['frame 1 raw, overlayed with ' num2str(nRgn2Exclude) ' regions to exclude'],'Parent',ax1)
hold(ax1,'on')
for r = 1:nRgn2Exclude
```

```
    plot(xVert{r},yVert{r},'color','r','Parent',ax1)
end
%subplot 2
imagesc(im1bp,'Parent',ax2),%colormap(ax2,'gray')
title(['frame 1 bandpassed, ' num2str(nRgn2Exclude) ' regions excluded'],'Parent',ax2)
hold(ax2,'on')
for r = 1:nRgn2Exclude
    plot(xVert{r},yVert{r},'color','r','Parent',ax2)
end
%subplot 3
mesh(im1bp,'Parent',ax3),%colormap(ax3,'jet') %then all 3 become jet ???
set(ax3,'YDir','reverse','View',[0 65])
title('frame 1 surface plot','Parent',ax3)
%subplot 4
mesh(im1bp,'Parent',ax4)
set(ax4,'YDir','reverse','View',[0 0])
title('frame 1 surface plot, view 2','Parent',ax4)

%Plot 2, shows default threshold, found by Otsu's method
figure('name',[filename ': Default threshold'])
set(gcf,'Position', figpos2)
ax1 = axes('position',[.05 .1 .27 .8],'units','normalized');
ax2 = axes('position',[.37 .1 .27 .8],'units','normalized');
ax3 = axes('position',[.69 .1 .27 .8],'units','normalized');
%subplot 1
imagesc(im1,'Parent',ax1),%colormap(ax1,'gray')
title(['frame 1 raw, overlayed with ' num2str(nRgn2Exclude) ' regions to exclude'],'Parent',ax1)
hold(ax1,'on')
for r = 1:nRgn2Exclude
    plot(xVert{r},yVert{r},'color','r','Parent',ax1)
end
title('raw image','Parent',ax1)
%subplot 2
mesh(im1bp,'Parent',ax2)
set(ax2,'YDir','reverse','View',[0 0])
bb = mat2gray(im1bp);
levelbb = graythresh(bb); % MATLAB's image threshold using Otsu's method
level = levelbb*(max(im1bp(:)) - min(im1bp(:))) + min(im1bp(:));
set(ax2,'Zlim',[0 level]);
title('frame 1 surface plot, zoom','Parent',ax2)
%subplot 3
BW = im2bw(bb,levelbb);
imagesc(BW,'Parent',ax3)
colormap(ax1,'gray')
title('thresholded image','Parent',ax3)

disp(['default threshold: ' num2str(level)])

% Give user option to accept calculated threshold, or manually choose
% threshold instead
userinput = input('Enter 1 to keep default, 0 to input manual threshold: ');
while ~(userinput == 0 || userinput == 1)
    userinput = input('Improper entry. Enter 1 to manually input threshold, 0 to keep default: ');
end
accept = 0;
while accept == 0
```

```
    if userinput == 0
        threshold = input('Enter threshhold: ');
        figure
        imagesc(im1bp>threshold)
        title('Thresholded image')
        colormap('gray')
        accept = input('Enter 1 to accept manual threshold, 0 to change it: ');
    elseif userinput == 1
        threshold = level;
        accept = 1;
    end
end

close all
```

Function for bandpass filtering an image

```
function imbp = bpass_dissertation(im,lnoise,lobject)
%
% Bandpas filter
%
% Filters the input image using a real-space bandpass filter. Reduces pixel
% noise and long-wavelenth image variations, while retaining features of
% the desired size.
%
% inputs: im: Original image (must be floating-point data type), with bright
%             spots against a dark background.
%         lnoise: Lengthscale of noise in pixels, usually set as 1. Can set
%                 to 0 to omit Gaussian smoothing.
%         lobject: Length in pixels, slightly larger than size of particle
%                  image; must be odd.
% output: imbp: Bandpass filtered image
%
% This code is based upon Blair and Dufresne's bpass.m in MATLAB, which was
% adapted from Crocker and Grier's bpass.pro in IDL.
%
% Modified by Benjamin Schuster, JHU, 2012-2014.
%
% Helpful explanation from the original authors:
% "Performs a bandpass by convolving with an appropriate kernel.  You can
% think of this as a two part process.  First, a lowpassed image is
% produced by convolving the original with a Gaussian.  Next, a second
% lowpassed image is produced by convolving the original with a boxcar
% function. By subtracting the boxcar version from the Gaussian version, we
% are using the boxcar version to perform a highpass. Performing a lowpass
% and a highpass results in a bandpassed image."

if mod(lobject,2) == 0
    disp('lobject must be odd');
    return;
end

w = (lobject-1)/2;
x = -w:w;
```

```
%Gaussian kernel
if lnoise == 0
    gk = 0;
else
    normalize = @(x) x/sum(x);
    gaussian_kernel = normalize(exp(-(x/(2*lnoise)).^2));
    gk = gaussian_kernel'*gaussian_kernel;
end
% If lobject is 9 or more, you capture almost 100% of the Gaussian.
% If lobject is small, you start truncating the Gaussian kernel.
% It should be OK down to lobject = 7 .

%boxcar kernel
bk = ones(lobject,lobject)/lobject^2; %boxcar kernel

%Convolve the image with the kernel. (We can apply the Gaussian and boxcar
%kernels in one step because of the distributive property of convolutions.)
imbp = conv2(im,gk-bk,'same');

% Zero out the values at the edges of the image, since they're not useful.
imbp(1:w,:) = 0;
imbp((end - w + 1):end,:) = 0;
imbp(:,1:w) = 0;
imbp(:,(end - w + 1):end) = 0;

% Zero out negative pixels, since negative pixels shift the centroid peak.
imbp(imbp < 0) = 0;
```

Function for identifying local maxima in an image

```
function [pk,noisemean,noisestd]=pkfnd_dissertation(im,imbp,th,SE)
%
% Peak finder
%
% Finds local maxima in an image with pixel resolution. This provides a
% first approximation of particle locations, which will subsequently be
% refined. The code does this by by performing grayscale dilation on the
% image and then finding the union of the dilated image with the original
% image. Note, this only keeps one (the brightest) maxima within the radius
% of the structuring element used to do the image dilation. Only local
% maxima above a specified brigthness threshold are retained.
% Secondarily, this function also calculates the background
% noise in the image, which is used to estimate the signal-to-noise ratio.
%
% inputs: im: Original image (must be floating-point data type)
%         imbp: Bandpass-filtered image
%         th: Threshold value - minimum brightness of a local maximum pixel
%             from a true particle; dimmer particles are just noise and
%             will be discarded
%         SE: Structuring element for imdilate
% output: pk: An array containing coordinates of the identified local
%             maxima (peaks). pk(:,1) stores the x coordinates and
%             pk(:,2) the y coordinates of the local maxima.
%         noisemean: Average pixel value of the background in image im.
%         noisestd: Standard deviation of the background in image im.
```

```
%
% The peak finding algorithm is based on Crocker and Grier (1996). The
% noise calculation is based on Savin and Doyle (2005).
%
% Benjamin Schuster, JHU, 2012-2014.
%
% Note: imdilate() uses the MATLAB Image Processing Toolbox. Alternative
% approaches are available to find the local maxima without using
% imdilate().

% Conversion from floating point to uint16 makes imdilate() 2x faster, and
% shouldn't hurt the results. But for this to work right, we need to scale
% imbp to use the full range of values available; otherwise, we will lose
% pixel-to-pixel differences due rounding, especially for images with
% low contrast.
maximbp = max(imbp(:));
imbpsc = uint16((2^16-1)*imbp/maximbp); %scale to use full 16-bit range of uint16
imdil = imdilate(imbpsc,SE); %grayscale image dilation with structuring element SE
pk = [];
% Local maxima are the union of the image and its dilation. Only keep local
% maxima above the previously determined brightness threshold.
[pk(:,2), pk(:,1)] = find(imdil == imbpsc & imdil > (2^16-1)*th/maximbp);
% pk(:,1) stores the x coordinates (im columns), pk(:,2) the y coordinates
% (im rows) of the local maxima

%%% Slower method
% imdil = imdilate(imbp,SE);
% pk = [];
% [pk(:,2),pk(:,1)]=find(imdil == imbp & imdil>th);

%%% To plot the identified particle locations on top of the image:
% figure, imagesc(im), hold on, plot(pk(:,1),pk(:,2),'k.')
%%% And to plot the identified local maxima on the dilated image:
% figure, imagesc(imdil), hold on, plot(pk(:,1),pk(:,2),'k.')

% The following code is used for calculating the background noise, which we
% will use to estimate the signal-to-noise ratio.
% Only keep the dimmer 50% of pixels for making the noise mask. Other
% cutoff values could be used, such as mean or a different percentile.
NoiseMask = imdil < median(imdil(:));
NoiseRegW0 = NoiseMask.*im; % regions we'll use to calculate noise are nonzero
NoisePix = nonzeros(NoiseRegW0); % discard zeros; calculate noise from remaining pixels
noisestd = std(NoisePix);
noisemean = mean(NoisePix);
```

Function for calculating intensity-weighted centroids (centers) of particles

```
function cntrds = cntrd_dissertation(im,pk,sz,interactive)
%
% This function calculates centroids of candidate particles. It takes the
% local maxima pixels identified previously and computes refined estimates
% of the particle centers. This permits sub-pixel resolution if the
% images are of sufficient quality.
%
% inputs: im: Original image (must be floating-point data type)
```

```
%        pk: Array of local maxima (peaks) in the image, output from pkfnd
%        sz: Diameter of ROI over which to calculate the centroid. Should
%            be large enough to capture the whole particle of interest,
%            but not others.
%        interactive: Optional plot, only displays if "interactive" is set
%            to 1. Displays the location of the brightest pixel and the
%            centroid on the ROI
%
% output:  cntrds, a n_pks x 5 array containing the centroid
%         locations and particle measurements
%          cntrds(:,1) contains the x-coordinates
%          cntrds(:,2) contains the y-coordinates
%          cntrds(:,3) contains the particles' brightness
%          cntrds(:,4) contains the square of the radius of gyration
%          cntrds(:,5) contains the eccentricity
%
% This code is based upon Blair and Dufresne's cntrd.m in MATLAB, which was
% adapted from Crocker and Grier's IDL code. Eccentricity calculation
% is based on MATLAB code from the Kilfoil lab. Note, this function does
% not contain all the features of Crocker and Grier's IDL centroid code.
%
% Modified by Benjamin Schuster, JHU, 2012-2014.

if nargin==3
   interactive=0;
end

if mod(sz,2) == 0
   disp('sz must be odd');
   return;
end

if isempty(pk)
   disp('No positions were input into cntrd. Check your pkfnd threshold.')
   cntrds=[];
   return;
end

mdpt = (sz+1)/2;
w = (sz-1)/2;
r = sz/2;

% create mask - window around candidate particle location over which to
% calculate the centroid
c_array = meshgrid(1:sz,1:sz)-mdpt; %same values within a column
r_array = c_array'; %same values within a row
dst2 = r_array.^2+c_array.^2;
msk = double(dst2 <= r^2); % Crocker and Grier paper uses <= w^2

% masks for eccentricity calculation, adapted from Maria Kilfoil's code
thetas = atan2(r_array,c_array);
cmsk = cos(2*thetas).*msk;
smsk = sin(2*thetas).*msk;

n_pks = size(pk,1);
cntrds = zeros(n_pks,5);
```

```
if interactive == 1
    figure
end

%loop through all of the candidate positions
maxiters = 5;
for i=1:n_pks
    %select neighborhood around each candidate location, and apply the mask
    roi = msk.*im((pk(i,2)-w:pk(i,2)+w),(pk(i,1)-w:pk(i,1)+w));
    %calculate the total brightness
    tot_brightness = sum(roi(:));
    %calculate the weighted average x location
    xavg = sum(sum(roi.*c_array))/tot_brightness;
    %calculate the weighted average y location
    yavg = sum(sum(roi.*r_array))/tot_brightness;

    % If the calculated centroid is more than half a pixel in either
    % direction from the center of the brightest pixel, recalculate the
    % centroid using the previous estimate. Repeat if necessary, but not
    % for more than maxiters iterations.
    iters = 0;
    while (abs(xavg) > 0.5 || abs(yavg) > 0.5) && iters < maxiters
        iters = iters + 1;

        if abs(xavg) > 0.5
            pk(i,1) = pk(i,1) + round(xavg);
        end

        if abs(yavg) > 0.5
            pk(i,2) = pk(i,2) + round(yavg);
        end

        roi = msk.*im((pk(i,2)-w:pk(i,2)+w),(pk(i,1)-w:pk(i,1)+w));
        tot_brightness = sum(roi(:));
        xavg = sum(sum(roi.*c_array))/tot_brightness;
        yavg = sum(sum(roi.*r_array))/tot_brightness;
    end

    %store the refined centroid locations and particle brighness data
    cntrds(i,1) = pk(i,1) + xavg;
    cntrds(i,2) = pk(i,2) + yavg;
    cntrds(i,3) = tot_brightness;

    %calculate the radius of gyration^2
    cntrds(i,4) = sum(sum(roi.*dst2))/tot_brightness;

    %calculate the eccentricity
    numer1 = sum(sum(roi.*cmsk));
    numer2 = sum(sum(roi.*smsk));
    denom = tot_brightness - roi(mdpt,mdpt);
    cntrds(i,5) = sqrt(numer1^2 + numer2^2)/denom; %eccentricity

    % Optional plot, only displays if "interactive" is set to 1. Displays
    % the location of the brightest pixel and the centroid on the ROI.
    if interactive==1
```

```
        imagesc(roi)
        colormap('jet')
        axis image
        hold on
        plot(mdpt+xavg,mdpt+yavg,'mx')
        plot(mdpt+xavg,mdpt+yavg,'mo')
        plot(mdpt,mdpt,'k.')
        title(['brightness ',num2str(tot_brightness),', size ', ...
            num2str(sqrt(cntrds(i,4))), ' eccentricity ', ...
            num2str(cntrds(i,5))])
        pause
    end
end
```

Function for linking particle locations into trajectories

```
function B = mytracker_dissertation(pos,maxdisp,memory_nframes,min_frames)

% Takes the list of particle positions (centroids) and links them into
% trajectories.
%
% inputs:
% pos: the first dimn columns are the dimn particle cordinates; the last
%      (dimn+1) column is frame #
% maxdisp: maximum displacement a particle could go from one frame to next
% memory_nframes: is # of consecutive frames a particle can go out of view
%  and be tracked as the same particle; 0 if no memory
% min_frames: eliminate trajectories with fewer than this number of frames
%
% output:
% list of trajectories
%
% Benjamin Schuster, JHU, 2012-2014

dimn = 2; %dimensionality of the particle coordinate data
maxdispSq = maxdisp^2;

[r,c] = size(pos);
PosConn = zeros(r,c+1); %the added column is for storing the trajectory #
PosConn(:,1:dimn+4) = pos;

% check the input time vector
t = pos(:,dimn+4);
dt = t(2:end) - t(1:end-1); %indicates where the frame number changes
if dt == 0
    disp('Error - All positions are at the same time')
    return
elseif sum(dt<0) ~= 0
    disp('Error - The time vector is not in order')
    return
elseif sum(dt>1) ~= 0
    disp('Error - Some frames have no particles detected')
    return
end
```

```
indices = [find(dt > 0); length(t)]; %index of last row of pos data for every frame
num_frames = length(indices);
indices = [0; indices];

%lost_p{i} is list of particles whose last known location occurs in frame i,
%then particle is missing from frame i + 1
lost_p = cell(num_frames-1,1);
for i = 1:num_frames-1
    M = indices(i+1)-indices(i);
    %Initialize lost_p{i} to list all the particles in frame i; later we'll
    %remove those that have been assigned to a trajectory.
    lost_p{i} = (1:M)';
end

PosConn(1:indices(2),end) = 1:indices(2); %all the particles in first frame are assinged new trajectory ID #
pcount = indices(2); %number of trajectories so far
disp('Starting tracking routine');
for i = 2:num_frames %loop over the frames
    if i == 2
        mxmem = 0;
    elseif i < memory_nframes + 2 %memory (# of skipped frames) must be adjusted for the first few frames
        mxmem = i - 2;
    else
        mxmem = memory_nframes;
    end

    N = indices(i+1)-indices(i); %# of particles detected in frame i
    indices_current = (indices(i)+1):indices(i+1);
    pos_current = PosConn(indices_current,1:dimn);

    not_assigned_n = 1:N; %list of particles in frame i not yet assigned to a particle in frame i-1
    colID = 1:N;

    for h = 0:mxmem %look to frames i-1 through i-1-mxmem to "connect the dots" in frame i
        if ~isempty(not_assigned_n) && ~isempty(lost_p{i-1-h})

            M = indices(i-h)-indices(i-1-h); %# of spots detected in frame i-1-h
            indices_prev = (indices(i-1-h)+1):indices(i-h);
            pos_prev = PosConn(indices_prev,:);

%           %%% This is slow when there are a lot of particles!!
%           %matrix of all possible "bond lengths" squared
%           DeltaSq = NaN*ones(M,N); %NaN remains for particles that have already been assigned
%           for m = lost_p{i-1-h}'  %m down the rows
%               for n = not_assigned_n %n across the columns
%                   DeltaSq(m,n) = sum((pos_current(n,1:dimn) - pos_prev(m,1:dimn)).^2);
%               end
%           end

            % This is faster. But note we're still doing lots of extra
            % computations (calculating "bond lengths" that are much
            % larger than maxdispSq, such as from particles on opposite
            % sides of the image field).
            pos_current2 = NaN(size(pos_current));
            pos_current2(not_assigned_n,:) = pos_current(not_assigned_n,:);
            pos_prev2 = NaN(size(pos_prev));
```

```
pos_prev2(lost_p{i-1-h},:) = pos_prev(lost_p{i-1-h},:);

DeltaX = zeros(M,N,dimn);
for dd = 1:dimn %loop over the x, y (and z if applicable) coordinates
    for n = 1:N %n across the columns
        DeltaX(:,n,dd) = pos_current2(n,dd) - pos_prev2(:,dd);
    end
end
DeltaSq = sum(DeltaX.^2,3);

%bonds shorter than the user-specified maximum
EligibleBonds = DeltaSq < maxdispSq;
row_sum = sum(EligibleBonds);
col_sum = sum(EligibleBonds,2);

rowID = (1:M)';
for n = not_assigned_n %loop over not yet assigned particles in frame i
    %note: not_assigned_n changes within this loop. MATLAB
    %still loops over all elements that are in not_assigned_n when
    %the loop begins.

    %conn_m gives spots in frame i-1 that spot n in frame i could be connected to
    conn_m = rowID(EligibleBonds(:,n)); %uses logical indexing

    % if row_sum(n) == 0 %no eligible bonds - don't do anything
    if row_sum(n) == 1 && col_sum(conn_m) == 1 %trivial bond case
        %give spot n the trajectory ID of spot m
        PosConn(indices(i)+n,end)= pos_prev(conn_m,end);
        %remove n from list of not assigned particles in frame i
        not_assigned_n(not_assigned_n == n) = [];
        %remove m from list of not assigned particles in frame i-1-h
        lost_p{i-1-h}(lost_p{i-1-h} == conn_m) = [];
    elseif row_sum(n) > 0 %non-trivial bonds
        %Identify the subnetwork
        subnetwork = cell(1,2);
        new_ms = conn_m;
        new_ns = n;
        while ~isempty(new_ns) %new_ms will be empty if new_ms is
            subnetwork{1} = [subnetwork{1}; new_ms]; %spots from frame i-1 in subnetwork
            subnetwork{2} = [subnetwork{2}, new_ns]; %spots from frame i in subnetwork

            EligibleBonds(:,new_ns) = 0; %to prevent working on the same particle twice
            row_sum(new_ns) = -1; %to prevent working on the same particle twice
            new_ns = [];
            for k = 1:length(new_ms)
                new_ns = [new_ns, colID(EligibleBonds(new_ms(k),:))];
            end
            new_ns = unique(new_ns);

            EligibleBonds(new_ms,:) = 0; %to prevent working on the same particle twice
            %col_sum(new_ms) = -1; %not necessary
            new_ms = [];
            for k = 1:length(new_ns)
                new_ms = [new_ms; rowID(EligibleBonds(:,new_ns(k)))];
            end
            new_ms = unique(new_ms);
```

```
end

%Warning about combinatorics if subnetwork is large
len_sntwk_m = length(subnetwork{1});
len_sntwk_n = length(subnetwork{2});
if len_sntwk_m > 10 || len_sntwk_n > 10
   disp('Excessive combinatorics. Exiting now.')
   disp('Check parameters (especially max displacement).')
   return
elseif len_sntwk_m > 7 || len_sntwk_n > 7
   disp('Difficult combinatorics.')
end

%Determine the optimal set of bonds for the subnetwork
if len_sntwk_m <= len_sntwk_n
   %list of possible perutations of the n's in subnetwork
   P = perms(subnetwork{2});
   %account for unequal # of spots in subnetwork in the 2 frames
   P2 = unique(P(:,1:len_sntwk_m),'rows');
   BondLenSq = zeros(size(P2));
   for j = 1:size(P2,1)
      idx = sub2ind([M N],subnetwork{1}', P2(j,:));
      bondlensq_1perm = DeltaSq(idx);
      if bondlensq_1perm<maxdispSq
         BondLenSq(j,:) = bondlensq_1perm;
      else
         % rule out permutations with any bond length >= max displacement
         BondLenSq(j,:) = NaN;
         % better to use penalty than NaN?
      end
   end
   sumbonds = sum(BondLenSq,2);
   [minsum,best_perm_id] = min(sumbonds);
   bestn = P2(best_perm_id,:);
   bestm = subnetwork{1};
else %len_sntwk_m > len_sntwk_n
   P = perms(subnetwork{1});
   P2 = unique(P(:,1:len_sntwk_n),'rows');
   BondLenSq = zeros(size(P2));
   for j = 1:size(P2,1)
      idx = sub2ind([M N],P2(j,:),subnetwork{2});
      bondlensq_1perm = DeltaSq(idx);
      if bondlensq_1perm<maxdispSq
         BondLenSq(j,:) = bondlensq_1perm;
      else
         BondLenSq(j,:) = NaN;
      end
   end
   sumbonds = sum(BondLenSq,2);
   [minsum,best_perm_id] = min(sumbonds);
   bestm = P2(best_perm_id,:);
   bestn = subnetwork{2};
end
PosConn(indices(i)+bestn,end)= pos_prev(bestm,end);

% keep record of which particles have been assigned
```

```
                for j = 1:length(bestn) %note bestm and bestn will have equal lengths
                    not_assigned_n(not_assigned_n == bestn(j)) = [];
                    lost_p{i-1-h}(lost_p{i-1-h} == bestm(j)) = [];
                end

            end
        end %end of loop over n

    end
end %end of loop over previous frames (memory)

%particles that are still unassigned become start of new trajectories
for k = 1:length(not_assigned_n)
    pcount = pcount + 1;
    PosConn(indices(i)+not_assigned_n(k),end) = pcount;
end

%update user on tracking progress
if mod(i,25)==0
    disp(['tracking - finished ' num2str(i) ' frames'])
end

end

S = sortrows(PosConn,size(PosConn,2)); %sort by trajectory number
S2 = [S(:,dimn+5) S(:,dimn+4) S(:,1:dimn+3)]; %reorder the columns
% now the columns are (left to right): particle number, frame number, spatial
% coordinates, particle brightness, radius of gyration, and eccentricity
num_particles = S2(end,1);

%find # of frames for each particle
frames = zeros(1,num_particles);
for i=1:num_particles
    frames(i)=sum(S2(:,1)==i);
end

% %remove particles (trajectories) with fewer than min_frames
% much slower!
% tic
% for k=num_particles:-1:1
%     if frames(k)<min_frames
%         rows=sum(frames(1:k));
%         S2=[S2(1:(rows-frames(k)),:);S2((rows+1):end,:)];
%     end
% end
% toc

%much faster!
particles2keep = find(frames >= min_frames);
S2 = S2(ismember(S2(:,1),particles2keep),:);

%re-number the particles
j=1;
S3 = S2;
S3(1,1) = 1;
gaps = [];
```

```
for i=2:length(S2)
    dt = S2(i,2)-S2(i-1,2);
    if S2(i,1)~=S2(i-1,1);
        j=j+1;
    elseif dt ~= 1
        gaps = [gaps; (i-1) dt]; %record index and length of gaps/skipped frames
    end
    S3(i,1)=j;
end
num_particles=j; % # of particles

Bcell = cell(2*size(gaps,1)+1,1);
gaps(end+1,:) = [size(S3,1) NaN];
Bcell{1} = S3(1:gaps(1,1),:);
for k=1:size(gaps,1)-1
    Binsertion = [];
    %     v = zeros(1,dimn+2);
    v = NaN*ones(1,dimn+5); % for skipped frames, set the position coordinates to NaN
    v(1) = 0;
    v(2) = 1;
    for j = 1:gaps(k,2)-1
        Binsertion = [Binsertion; S3(gaps(k,1),:) + v];
        v(2) = v(2) + 1;
    end
    Bcell{2*k} = Binsertion;
    Bcell{2*k+1} = S3(gaps(k,1)+1:gaps(k+1,1),:);
end
B = cell2mat(Bcell);

disp('tracking done');
```

Function for formatting the trajectory data

```
function [B,Timescale,particles,frames] = process_MPT_data_dissertation(B,frame_rate)

% Formats the raw MPT data file
%
% Benjamin Schuster, JHU, 2012-2014

max_frame=max(B(:,2)); %determine largest # of frames from column 2 of the input file

%create timescale vector
Timescale=(1:max_frame-1)/frame_rate;

%Rewrite 1st column of matrix so paricles are numbered sequentially,
%starting from 1. Necessary to calculate MSD from multiple movies in a group.
j=0;
for i=1:length(B);
    if B(i,2)==1;
        j=j+1;
    end
    B(i,1)=j;
end
particles=j; % # of particles
```

```
%find # of frames for each particle
frames = zeros(1,particles);
for i=1:particles
    frames(i)=sum(B(:,1)==i);
end
```

Function for calculating the mean squared displacement (MSD)

```
function [MSD,MSDx,MSDy,d_shortest_t,num_displacements] = ...
    calculate_MSD_dissertation(B,Timescale,particles,frames,conv)

% Input: Particle trajectories (tracked in 2 dimensions)
% Output: Retuns an array whose columns are each particle's MSD
%
% Benjamin Schuster, JHU, 2012

MSDx=nan(length(Timescale),particles);
MSDy=nan(length(Timescale),particles);
MSD=nan(length(Timescale),particles);

num_displacements = zeros(length(Timescale),particles);

d_shortest_t = [];

for j=1:particles %loop over particles
    %create a temporary matrix containing 1 particle worth of data
    C=B((1:frames(j))+sum(frames(1:j-1)),:);

    %calculate MSD for each time scale
    for k=1:frames(j)-1;
        xdisps = C(1+k:end,3)-C(1:end-k,3);
        xdisps = xdisps(~isnan(xdisps));
        count = length(xdisps);
        ydisps = C(1+k:end,4)-C(1:end-k,4);
        ydisps = ydisps(~isnan(ydisps));
        if k == 1
             d_shortest_t = [d_shortest_t; sqrt(xdisps.^2 + ydisps.^2)];
        end
        num_displacements(k,j) = count;
        MSDx(k,j) = conv^2*sum((xdisps).^2)/count; %if no NaNs, count =(frames(j)-k); %um^2
        MSDy(k,j) = conv^2*sum((ydisps).^2)/count; %um^2
        MSD(k,j) = MSDx(k,j)+MSDy(k,j); %um^2
    end
end
```

Function for creating particle tracking movie with trajectories overlaid

```
function makeTrajectoryMovie_dissertation(filename,ext,movieprofile,fpers,...
    movie_display,movieInfo,X,Y,xVert,yVert,nRgn2Exclude,startf,stopf)

% After tracking is completed, make movie with trajectories overlayed.
%
% Benjamin Schuster, JHU, 2012-2014
```

```
%
% Note: There is a problem with how MATLAB saves the output movies, which
% makes it appear that the trajectories are displaced one pixel down and
% right compared to where they should be - i.e. the identified particle
% centroid appears to be one pixel off in x and y from the brightest
% pixel in the particle. This is not a problem with the centroid
% calculation, nor is this problem present in the output movie displayed
% when the code is running - it is just an issue with how the movie is saved
% using getframe() and writevideo().

if movie_display == 1
    disp('Starting video writing. Do not resize or move figure window while movie is being written!')
else
    disp('Starting video writing.');
end

movieobj = VideoWriter([filename(1:(end-length(ext))) ' - tracked movie'],movieprofile);
movieobj.FrameRate = fpers;
open(movieobj);

m = movieInfo(1).Height;
n = movieInfo(1).Width;

f = figure('Units','pixels','Position',[150 150 n m],'visible','off','renderer','zbuffer');
ax1 = axes('Parent',f,'Position',[0 0 1 1],'units','normalized');
set(ax1,'XLim',[0 n],'YLim',[0 m],'YDir','reverse','visible','off');
if strcmp(ext,'.mov')
    movieobjin = VideoReader(filename);
end

for i = startf:stopf %only make a movie of the frames that were tracked
    cla(ax1)

    if strcmp(ext,'.tif')
        im = double(imread(filename, i, 'Info', movieInfo)); %Info speeds imread for multi-image tiff
    elseif strcmp(ext,'.mov')
        moviecdata = read(movieobjin,i);
        im = 256*3 - sum(moviecdata,3);
    end

    imagesc('Parent',ax1,'CData',im,'AlphaData',1)
    colormap(ax1,'gray')
    hold(ax1,'on')
    for r = 1:nRgn2Exclude
        plot(xVert{r},yVert{r},'color','r','Parent',ax1)
    end

    shiftedi=i-startf+1;

    RestX = X(shiftedi:end,:);
    FinishedTracksID = all(isnan(RestX),1);

    NotFinishedTracksX = [X(1:shiftedi,~FinishedTracksID); NaN(1,sum(~FinishedTracksID))];
    NotFinishedTracksY = [Y(1:shiftedi,~FinishedTracksID); NaN(1,sum(~FinishedTracksID))];
    FinishedTracksX = [X(1:shiftedi,FinishedTracksID); NaN(1,sum(FinishedTracksID))];
    FinishedTracksY = [Y(1:shiftedi,FinishedTracksID); NaN(1,sum(FinishedTracksID))];
```

```
    % since vectors are faster to plot than arrays
    NotFinishedTracksX2 = reshape(NotFinishedTracksX,numel(NotFinishedTracksX),1);
    NotFinishedTracksY2 = reshape(NotFinishedTracksY,numel(NotFinishedTracksY),1);
    FinishedTracksX2 = reshape(FinishedTracksX,numel(FinishedTracksX),1);
    FinishedTracksY2 = reshape(FinishedTracksY,numel(FinishedTracksY),1);

    line(NotFinishedTracksX2,NotFinishedTracksY2,'color','b'); % line() is faster than plot()
    line(FinishedTracksX2,FinishedTracksY2,'color','w');

    if movie_display == 1
        frm = getframe(f);
    else %if movie_display == 0
        frm = im2frame(zbuffer_cdata(gcf));
    end

    writeVideo(movieobj,frm);
    if mod(i,25)==0
        disp(['video writing - frame ' num2str(i) ' done'])
    end

end
close(movieobj);
```

References

1. Sung, JC, Pulliam, BL and Edwards, DA (2007). Nanoparticles for drug delivery to the lungs. *Trends Biotechnol* **25**: 563-570.

2. Crocker, JC and Grier, DG (1996). Methods of digital video microscopy for colloidal studies. *J Colloid Interface Sci* **179**: 298-310.

3. Sosnay, PR, Siklosi, KR, Van Goor, F, Kaniecki, K, Yu, H, Sharma, N *et al.* (2013). Defining the disease liability of variants in the cystic fibrosis transmembrane conductance regulator gene. *Nat Genet* **45**: 1160-1167.

4. Rowe, SM, Miller, S and Sorscher, EJ (2005). Cystic fibrosis. *N Engl J Med* **352**: 1992-2001.

5. Boyle, MP (2007). Adult cystic fibrosis. *JAMA* **298**: 1787-1793.

6. O'Sullivan, BP and Freedman, SD (2009). Cystic fibrosis. *Lancet* **373**: 1891-1904.

7. Davis, PB (2006). Cystic fibrosis since 1938. *Am J Respir Crit Care Med* **173**: 475-482.

8. Griesenbach, U and Alton, EW (2012). Progress in gene and cell therapy for cystic fibrosis lung disease. *Curr Pharm Des* **18**: 642-662.

9. Asokan, A, Schaffer, DV and Samulski, RJ (2012). The AAV vector toolkit: poised at the clinical crossroads. *Mol Ther* **20**: 699-708.

10. Dolovich, MB and Dhand, R (2011). Aerosol drug delivery: developments in device design and clinical use. *Lancet* **377**: 1032-1045.

11. Langer, R (1998). Drug delivery and targeting. *Nature* **392**: 5-10.

12. Kim, BY, Rutka, JT and Chan, WC (2010). Nanomedicine. *N Engl J Med* **363**: 2434-2443.

13. Fahy, JV and Dickey, BF (2010). Airway mucus function and dysfunction. *New England Journal of Medicine* **363**: 2233-2247.

14. Cone, RA (2009). Barrier properties of mucus. *Adv Drug Deliv Rev* **61**: 75-85.

15. Button, B, Cai, LH, Ehre, C, Kesimer, M, Hill, DB, Sheehan, JK *et al.* (2012). A periciliary brush promotes the lung health by separating the mucus layer from airway epithelia. *Science* **337**: 937-941.

16. Valentine, MT, Perlman, ZE, Gardel, ML, Shin, JH, Matsudaira, P, Mitchison, TJ *et al.* (2004). Colloid surface chemistry critically affects multiple particle tracking measurements of biomaterials. *Biophys J* **86**: 4004-4014.

17. Schuster, BS, Suk, JS, Woodworth, GF and Hanes, J (2013). Nanoparticle diffusion in respiratory mucus from humans without lung disease. *Biomaterials* **34**: 3439-3446.

18. Nance, EA, Woodworth, GF, Sailor, KA, Shih, TY, Xu, Q, Swaminathan, G *et al.* (2012). A dense poly(ethylene glycol) coating improves penetration of large polymeric nanoparticles within brain tissue. *Sci Transl Med* **4**: 149ra119.

19. Ensign, LM, Tang, BC, Wang, Y-Y, Tse, TA, Hoen, T, Cone, R *et al.* (2012). Mucus-penetrating nanoparticles for vaginal drug delivery protect against herpes simplex virus. *Sci Transl Med* **4**: 138ra179.

20. Suh, J, Wirtz, D and Hanes, J (2003). Efficient active transport of gene nanocarriers to the cell nucleus. *Proc Natl Acad Sci U S A* **100**: 3878-3882.

21. Seisenberger, G, Ried, MU, Endress, T, Buning, H, Hallek, M and Brauchle, C (2001). Real-time single-molecule imaging of the infection pathway of an adeno-associated virus. *Science* **294**: 1929-1932.

22. Braeckmans, K, Buyens, K, Bouquet, W, Vervaet, C, Joye, P, De Vos, F *et al.* (2010). Sizing nanomatter in biological fluids by fluorescence single particle tracking. *Nano Lett* **10**: 4435-4442.

23. Gelles, J, Schnapp, BJ and Sheetz, MP (1988). Tracking kinesin-driven movements with nanometre-scale precision. *Nature* **331**: 450-453.

24. Ghosh, RN and Webb, WW (1994). Automated detection and tracking of individual and clustered cell surface low density lipoprotein receptor molecules. *Biophys J* **66**: 1301-1318.

25. Martin, DS, Forstner, MB and Kas, JA (2002). Apparent subdiffusion inherent to single particle tracking. *Biophys J* **83**: 2109-2117.

26. Forier, K, Messiaen, AS, Raemdonck, K, Deschout, H, Rejman, J, De Baets, F *et al.* (2013). Transport of nanoparticles in cystic fibrosis sputum and bacterial

biofilms by single-particle tracking microscopy. *Nanomedicine (Lond)* **8**: 935-949.

27. Murphy, DB (2001). *Fundamentals of light microscopy and electronic imaging*, Wiley-Liss, New York, xii, 368 p.pp.

28. Diaspro, A (2010). *Nanoscopy and multidimensional optical fluorescence microscopy*, CRC Press/Taylor & Francis Group, Boca Raton.

29. Crocker, JC and Hoffman, BD (2007). Multiple-particle tracking and two-point microrheology in cells. *Methods Cell Biol* **83**: 141-178.

30. Small, A and Stahlheber, S (2014). Fluorophore localization algorithms for super-resolution microscopy. *Nat Methods* **11**: 267-279.

31. Deschout, H, Cella Zanacchi, F, Mlodzianoski, M, Diaspro, A, Bewersdorf, J, Hess, ST *et al.* (2014). Precisely and accurately localizing single emitters in fluorescence microscopy. *Nat Methods* **11**: 253-266.

32. Parthasarathy, R (2012). Rapid, accurate particle tracking by calculation of radial symmetry centers. *Nat Methods* **9**: 724-726.

33. Cheezum, MK, Walker, WF and Guilford, WH (2001). Quantitative comparison of algorithms for tracking single fluorescent particles. *Biophys J* **81**: 2378-2388.

34. Thompson, RE, Larson, DR and Webb, WW (2002). Precise nanometer localization analysis for individual fluorescent probes. *Biophys J* **82**: 2775-2783.

35. Bobroff, N (1986). Position Measurement with a Resolution and Noise-Limited Instrument. *Review of Scientific Instruments* **57**: 1152-1157.

36. Ober, RJ, Ram, S and Ward, ES (2004). Localization accuracy in single-molecule microscopy. *Biophys J* **86**: 1185-1200.

37. Savin, T, Spicer, PT and Doyle, PS (2008). A rational approach to noise discrimination in video microscopy particle tracking. *Applied Physics Letters* **93**.

38. Savin, T and Doyle, PS (2005). Static and dynamic errors in particle tracking microrheology. *Biophys J* **88**: 623-638.

39. Berg, HC (1993). *Random walks in biology*, Princeton University Press, Princeton, NJ, 152pp.

40. Deschout, H, Neyts, K and Braeckmans, K (2012). The influence of movement on the localization precision of sub-resolution particles in fluorescence microscopy. *J Biophotonics* **5**: 97-109.

41. Savin, T and Doyle, PS (2005). Role of a finite exposure time on measuring an elastic modulus using microrheology. *Physical Review E* **71**.

42. Chenouard, N, Smal, I, de Chaumont, F, Maska, M, Sbalzarini, IF, Gong, Y *et al.* (2014). Objective comparison of particle tracking methods. *Nat Methods* **11**: 281-289.

43. Betzig, E, Patterson, GH, Sougrat, R, Lindwasser, OW, Olenych, S, Bonifacino, JS *et al.* (2006). Imaging intracellular fluorescent proteins at nanometer resolution. *Science* **313**: 1642-1645.

44. Rust, MJ, Bates, M and Zhuang, X (2006). Sub-diffraction-limit imaging by stochastic optical reconstruction microscopy (STORM). *Nat Methods* **3**: 793-795.

45. Hess, ST, Girirajan, TP and Mason, MD (2006). Ultra-high resolution imaging by fluorescence photoactivation localization microscopy. *Biophys J* **91**: 4258-4272.

46. Sanders, NN, De Smedt, SC and Demeester, J (2000). The physical properties of biogels and their permeability for macromolecular drugs and colloidal drug carriers. *Journal of Pharmaceutical Sciences* **89**: 835-849.

47. Tarran, R, Grubb, BR, Gatzy, JT, Davis, CW and Boucher, RC (2001). The relative roles of passive surface forces and active ion transport in the modulation of airway surface liquid volume and composition. *Journal of General Physiology* **118**: 223-236.

48. Lai, SK, Wang, YY and Hanes, J (2009). Mucus-penetrating nanoparticles for drug and gene delivery to mucosal tissues. *Adv Drug Deliv Rev* **61**: 158-171.

49. Lai, SK, O'Hanlon, DE, Harrold, S, Man, ST, Wang, YY, Cone, R *et al.* (2007). Rapid transport of large polymeric nanoparticles in fresh undiluted human mucus. *Proc Natl Acad Sci U S A* **104**: 1482-1487.

50. Suk, JS, Lai, SK, Wang, YY, Ensign, LM, Zeitlin, PL, Boyle, MP *et al.* (2009). The penetration of fresh undiluted sputum expectorated by cystic fibrosis patients by non-adhesive polymer nanoparticles. *Biomaterials* **30**: 2591-2597.

51. Sanders, NN, De Smedt, SC, Van Rompaey, E, Simoens, P, De Baets, F and Demeester, J (2000). Cystic fibrosis sputum: a barrier to the transport of

nanospheres. *American Journal of Respiratory and Critical Care Medicine* **162**: 1905-1911.

52. Lai, SK, Suk, JS, Pace, A, Wang, YY, Yang, M, Mert, O *et al.* (2011). Drug carrier nanoparticles that penetrate human chronic rhinosinusitis mucus. *Biomaterials* **32**: 6285-6290.

53. Lai, SK, Wang, YY, Hida, K, Cone, R and Hanes, J (2010). Nanoparticles reveal that human cervicovaginal mucus is riddled with pores larger than viruses. *Proc Natl Acad Sci U S A* **107**: 598-603.

54. Rubin, BK, Ramirez, O, Zayas, JG, Finegan, B and King, M (1990). Collection and analysis of respiratory mucus from subjects without lung disease. *American Review of Respiratory Disease* **141**: 1040-1043.

55. Fahy, JV, Wong, H, Liu, J and Boushey, HA (1995). Comparison of samples collected by sputum induction and bronchoscopy from asthmatic and healthy subjects. *American Journal of Respiratory and Critical Care Medicine* **152**: 53-58.

56. Rubin, BK, Finegan, B, Ramirez, O and King, M (1990). General anesthesia does not alter the viscoelastic or transport properties of human respiratory mucus. *Chest* **98**: 101-104.

57. Nielsen, H, Hvidt, S, Sheils, CA and Janmey, PA (2004). Elastic contributions dominate the viscoelastic properties of sputum from cystic fibrosis patients. *Biophysical Chemistry* **112**: 193-200.

58. Janmey, PA, Georges, PC and Hvidt, S (2007). Basic rheology for biologists. *Methods in Cell Biology* **83**: 3-27.

59. Crowther, RS and Wetmore, RF (1987). Fluorometric assay of O-linked glycoproteins by reaction with 2-cyanoacetamide. *Analytical Biochemistry* **163**: 170-174.

60. Saltzman, WM, Radomsky, ML, Whaley, KJ and Cone, RA (1994). Antibody diffusion in human cervical mucus. *Biophys J* **66**: 508-515.

61. Suh, J, Dawson, M and Hanes, J (2005). Real-time multiple-particle tracking: applications to drug and gene delivery. *Adv Drug Deliv Rev* **57**: 63-78.

62. Saxton, MJ and Jacobson, K (1997). Single-particle tracking: applications to membrane dynamics. *Annual Review of Biophysics and Biomolecular Structure* **26**: 373-399.

63. Mason, TG and Weitz, DA (1995). Optical measurements of frequency-dependent linear viscoelastic moduli of complex fluids. *Phys Rev Lett* **74**: 1250-1253.

64. Mason, TG, Ganesan, K, vanZanten, JH, Wirtz, D and Kuo, SC (1997). Particle tracking microrheology of complex fluids. *Physical Review Letters* **79**: 3282-3285.

65. Macosko, CW (1994). *Rheology: principles, measurements, and applications*, VCH, New York, xviii, 550 p.pp.

66. App, EM, Kieselmann, R, Reinhardt, D, Lindemann, H, Dasgupta, B, King, M *et al.* (1998). Sputum rheology changes in cystic fibrosis lung disease following two different types of physiotherapy: flutter vs autogenic drainage. *Chest* **114**: 171-177.

67. Innes, AL, Carrington, SD, Thornton, DJ, Kirkham, S, Rousseau, K, Dougherty, RH *et al.* (2009). Ex vivo sputum analysis reveals impairment of protease-dependent mucus degradation by plasma proteins in acute asthma. *American Journal of Respiratory and Critical Care Medicine* **180**: 203-210.

68. Suk, JS, Lai, SK, Boylan, NJ, Dawson, MR, Boyle, MP and Hanes, J (2011). Rapid transport of muco-inert nanoparticles in cystic fibrosis sputum treated with N-acetyl cysteine. *Nanomedicine (Lond)* **6**: 365-375.

69. Braeckmans, K, Peeters, L, Sanders, NN, De Smedt, SC and Demeester, J (2003). Three-dimensional fluorescence recovery after photobleaching with the confocal scanning laser microscope. *Biophys J* **85**: 2240-2252.

70. Garbuzenko, OB, Saad, M, Pozharov, VP, Reuhl, KR, Mainelis, G and Minko, T (2010). Inhibition of lung tumor growth by complex pulmonary delivery of drugs with oligonucleotides as suppressors of cellular resistance. *Proc Natl Acad Sci U S A* **107**: 10737-10742.

71. Ballester, M, Nembrini, C, Dhar, N, de Titta, A, de Piano, C, Pasquier, M *et al.* (2011). Nanoparticle conjugation and pulmonary delivery enhance the protective efficacy of Ag85B and CpG against tuberculosis. *Vaccine* **29**: 6959-6966.

72. Nembrini, C, Stano, A, Dane, KY, Ballester, M, van der Vlies, AJ, Marsland, BJ *et al.* (2011). Nanoparticle conjugation of antigen enhances cytotoxic T-cell responses in pulmonary vaccination. *Proc Natl Acad Sci U S A* **108**: E989-997.

73. World Health Organization. (2009). *Global health risks: mortality and burden of disease attributable to selected major risks*, World Health Organization, Geneva, Switzerland, vi, 62 p.pp.

74. Cai, LH, Panyukov, S and Rubinstein, M (2011). Mobility of nonsticky nanoparticles in polymer liquids. *Macromolecules* **44**: 7853-7863.

75. Wong, IY, Gardel, ML, Reichman, DR, Weeks, ER, Valentine, MT, Bausch, AR *et al.* (2004). Anomalous diffusion probes microstructure dynamics of entangled F-actin networks. *Phys Rev Lett* **92**: 178101.

76. Jokerst, JV, Lobovkina, T, Zare, RN and Gambhir, SS (2011). Nanoparticle PEGylation for imaging and therapy. *Nanomedicine (Lond)* **6**: 715-728.

77. de Gennes, PG (1980). Conformations of Polymers Attached to an Interface. *Macromolecules* **13**: 1069-1075.

78. Dickey, BF (2012). Biochemistry. Walking on solid ground. *Science* **337**: 924-925.

79. Matthews, LW, Spector, S, Lemm, J and Potter, JL (1963). Studies on pulmonary secretions. I. The over-all chemical composition of pulmonary secretions from patients with cystic fibrosis, bronchiectasis, and laryngectomy. *American Review of Respiratory Disease* **88**: 199-204.

80. Lai, SK, Wang, YY, Cone, R, Wirtz, D and Hanes, J (2009). Altering mucus rheology to "solidify" human mucus at the nanoscale. *PLoS One* **4**: e4294.

81. Shin, JH, Gardel, ML, Mahadevan, L, Matsudaira, P and Weitz, DA (2004). Relating microstructure to rheology of a bundled and cross-linked F-actin network in vitro. *Proc Natl Acad Sci U S A* **101**: 9636-9641.

82. Bernhard, W, Haagsman, HP, Tschernig, T, Poets, CF, Postle, AD, van Eijk, ME *et al.* (1997). Conductive airway surfactant: surface-tension function, biochemical composition, and possible alveolar origin. *American Journal of Respiratory Cell and Molecular Biology* **17**: 41-50.

83. Gehr, P, Green, FH, Geiser, M, Im Hof, V, Lee, MM and Schurch, S (1996). Airway surfactant, a primary defense barrier: mechanical and immunological aspects. *Journal of Aerosol Medicine* **9**: 163-181.

84. Suk, JS, Boylan, NJ, Trehan, K, Tang, BC, Schneider, CS, Lin, JM *et al.* (2011). N-acetylcysteine enhances cystic fibrosis sputum penetration and airway gene transfer by highly compacted DNA nanoparticles. *Mol Ther* **19**: 1981-1989.

85. Johnson, LG, Boyles, SE, Wilson, J and Boucher, RC (1995). Normalization of raised sodium absorption and raised calcium-mediated chloride secretion by adenovirus-mediated expression of cystic fibrosis transmembrane conductance regulator in primary human cystic fibrosis airway epithelial cells. *J Clin Invest* **95**: 1377-1382.

86. Hyde, SC, Gill, DR, Higgins, CF, Trezise, AE, MacVinish, LJ, Cuthbert, AW *et al.* (1993). Correction of the ion transport defect in cystic fibrosis transgenic mice by gene therapy. *Nature* **362**: 250-255.

87. Mueller, C and Flotte, TR (2008). Gene therapy for cystic fibrosis. *Clin Rev Allergy Immunol* **35**: 164-178.

88. Flotte, TR, Fischer, AC, Goetzmann, J, Mueller, C, Cebotaru, L, Yan, Z *et al.* (2010). Dual reporter comparative indexing of rAAV pseudotyped vectors in chimpanzee airway. *Mol Ther* **18**: 594-600.

89. Sanders, N, Rudolph, C, Braeckmans, K, De Smedt, SC and Demeester, J (2009). Extracellular barriers in respiratory gene therapy. *Adv Drug Deliv Rev* **61**: 115-127.

90. Hida, K, Lai, SK, Suk, JS, Won, SY, Boyle, MP and Hanes, J (2011). Common gene therapy viral vectors do not efficiently penetrate sputum from cystic fibrosis patients. *PLoS One* **6**: e19919.

91. Kitson, C, Angel, B, Judd, D, Rothery, S, Severs, NJ, Dewar, A *et al.* (1999). The extra- and intracellular barriers to lipid and adenovirus-mediated pulmonary gene transfer in native sheep airway epithelium. *Gene Ther* **6**: 534-546.

92. Liu, X, Yan, Z, Luo, M and Engelhardt, JF (2006). Species-specific differences in mouse and human airway epithelial biology of recombinant adeno-associated virus transduction. *Am J Respir Cell Mol Biol* **34**: 56-64.

93. Opie, SR, Warrington, KH, Jr., Agbandje-McKenna, M, Zolotukhin, S and Muzyczka, N (2003). Identification of amino acid residues in the capsid proteins

of adeno-associated virus type 2 that contribute to heparan sulfate proteoglycan binding. *J Virol* **77**: 6995-7006.

94. Walters, RW, Yi, SM, Keshavjee, S, Brown, KE, Welsh, MJ, Chiorini, JA *et al.* (2001). Binding of adeno-associated virus type 5 to 2,3-linked sialic acid is required for gene transfer. *J Biol Chem* **276**: 20610-20616.

95. Wu, Z, Miller, E, Agbandje-McKenna, M and Samulski, RJ (2006). Alpha2,3 and alpha2,6 N-linked sialic acids facilitate efficient binding and transduction by adeno-associated virus types 1 and 6. *J Virol* **80**: 9093-9103.

96. Wu, P, Xiao, W, Conlon, T, Hughes, J, Agbandje-McKenna, M, Ferkol, T *et al.* (2000). Mutational analysis of the adeno-associated virus type 2 (AAV2) capsid gene and construction of AAV2 vectors with altered tropism. *J Virol* **74**: 8635-8647.

97. Kern, A, Schmidt, K, Leder, C, Muller, OJ, Wobus, CE, Bettinger, K *et al.* (2003). Identification of a heparin-binding motif on adeno-associated virus type 2 capsids. *J Virol* **77**: 11072-11081.

98. Zolotukhin, S, Potter, M, Zolotukhin, I, Sakai, Y, Loiler, S, Fraites, TJ, Jr. *et al.* (2002). Production and purification of serotype 1, 2, and 5 recombinant adeno-associated viral vectors. *Methods* **28**: 158-167.

99. Salganik, M, Aydemir, F, Nam, HJ, McKenna, R, Agbandje-McKenna, M and Muzyczka, N (2014). Adeno-associated virus capsid proteins may play a role in transcription and second-strand synthesis of recombinant genomes. *J Virol* **88**: 1071-1079.

100. Zolotukhin, S, Byrne, BJ, Mason, E, Zolotukhin, I, Potter, M, Chesnut, K *et al.* (1999). Recombinant adeno-associated virus purification using novel methods improves infectious titer and yield. *Gene Ther* **6**: 973-985.

101. Bartlett, JS, Wilcher, R and Samulski, RJ (2000). Infectious entry pathway of adeno-associated virus and adeno-associated virus vectors. *J Virol* **74**: 2777-2785.

102. Bates, D, Maechler, M, Bolker, B and Walker, S (2013). lme4: Linear mixed-effects models using Eigen and S4.

103. Kim, AJ, Boylan, NJ, Suk, JS, Hwangbo, M, Yu, T, Schuster, BS *et al.* (2013). Use of single-site-functionalized PEG dendrons to prepare gene vectors that penetrate human mucus barriers. *Angew Chem Int Ed Engl* **52**: 3985-3988.

104. Dawson, M, Wirtz, D and Hanes, J (2003). Enhanced viscoelasticity of human cystic fibrotic sputum correlates with increasing microheterogeneity in particle transport. *J Biol Chem* **278**: 50393-50401.

105. Hamid, Q, Shannon, J and Martin, JG (2005). *Physiologic basis of respiratory disease*, BC Decker, Hamilton, ON, 793pp.

106. Solic, N, Wilson, J, Wilson, SJ and Shute, JK (2005). Endothelial activation and increased heparan sulfate expression in cystic fibrosis. *Am J Respir Crit Care Med* **172**: 892-898.

107. Chan, SC, Shum, DK and Ip, MS (2003). Sputum sol neutrophil elastase activity in bronchiectasis: differential modulation by syndecan-1. *Am J Respir Crit Care Med* **168**: 192-198.

108. Lieleg, O, Lieleg, C, Bloom, J, Buck, CB and Ribbeck, K (2012). Mucin biopolymers as broad-spectrum antiviral agents. *Biomacromolecules* **13**: 1724-1732.

109. Auricchio, A, O'Connor, E, Hildinger, M and Wilson, JM (2001). A single-step affinity column for purification of serotype-5 based adeno-associated viral vectors. *Mol Ther* **4**: 372-374.

110. Walters, RW, Pilewski, JM, Chiorini, JA and Zabner, J (2002). Secreted and transmembrane mucins inhibit gene transfer with AAV4 more efficiently than AAV5. *J Biol Chem* **277**: 23709-23713.

111. Wang, YY, Kannan, A, Nunn, KL, Murphy, MA, Subramani, DB, Moench, T *et al.* (2014). IgG in cervicovaginal mucus traps HSV and prevents vaginal Herpes infections. *Mucosal Immunol*.

112. Cone, R (1999). Mucus. *Mucosal Immunol* **3**: 43-64.

113. Olmsted, SS, Padgett, JL, Yudin, AI, Whaley, KJ, Moench, TR and Cone, RA (2001). Diffusion of macromolecules and virus-like particles in human cervical mucus. *Biophys J* **81**: 1930-1937.

114. Chirmule, N, Propert, K, Magosin, S, Qian, Y, Qian, R and Wilson, J (1999). Immune responses to adenovirus and adeno-associated virus in humans. *Gene Ther* **6**: 1574-1583.

115. Halbert, CL, Miller, AD, McNamara, S, Emerson, J, Gibson, RL, Ramsey, B *et al.* (2006). Prevalence of neutralizing antibodies against adeno-associated virus

(AAV) types 2, 5, and 6 in cystic fibrosis and normal populations: Implications for gene therapy using AAV vectors. *Hum Gene Ther* **17**: 440-447.

116. Calcedo, R, Vandenberghe, LH, Gao, G, Lin, J and Wilson, JM (2009). Worldwide epidemiology of neutralizing antibodies to adeno-associated viruses. *J Infect Dis* **199**: 381-390.

117. Boyle, MP, Enke, RA, Reynolds, JB, Mogayzel, PJ, Jr., Guggino, WB and Zeitlin, PL (2006). Membrane-associated heparan sulfate is not required for rAAV-2 infection of human respiratory epithelia. *Virol J* **3**: 29.

118. Mogayzel, PJ, Jr., Naureckas, ET, Robinson, KA, Mueller, G, Hadjiliadis, D, Hoag, JB *et al.* (2013). Cystic fibrosis pulmonary guidelines. Chronic medications for maintenance of lung health. *Am J Respir Crit Care Med* **187**: 680-689.

119. Kesimer, M, Ehre, C, Burns, KA, Davis, CW, Sheehan, JK and Pickles, RJ (2013). Molecular organization of the mucins and glycocalyx underlying mucus transport over mucosal surfaces of the airways. *Mucosal Immunol* **6**: 379-392.

120. Virella-Lowell, I, Poirier, A, Chesnut, KA, Brantly, M and Flotte, TR (2000). Inhibition of recombinant adeno-associated virus (rAAV) transduction by bronchial secretions from cystic fibrosis patients. *Gene Ther* **7**: 1783-1789.

121. Excoffon, KJ, Koerber, JT, Dickey, DD, Murtha, M, Keshavjee, S, Kaspar, BK *et al.* (2009). Directed evolution of adeno-associated virus to an infectious respiratory virus. *Proc Natl Acad Sci USA* **106**: 3865-3870.

122. Wu, Y, Wawrzusin, P, Senseney, J, Fischer, RS, Christensen, R, Santella, A *et al.* (2013). Spatially isotropic four-dimensional imaging with dual-view plane illumination microscopy. *Nat Biotechnol* **31**: 1032-1038.

123. Ritter, JG, Veith, R, Siebrasse, JP and Kubitscheck, U (2008). High-contrast single-particle tracking by selective focal plane illumination microscopy. *Opt Express* **16**: 7142-7152.

124. Ritter, JG, Veith, R, Veenendaal, A, Siebrasse, JP and Kubitscheck, U (2010). Light sheet microscopy for single molecule tracking in living tissue. *PLoS One* **5**: e11639.

125. Spille, JH, Kaminski, T, Konigshoven, HP and Kubitscheck, U (2012). Dynamic three-dimensional tracking of single fluorescent nanoparticles deep inside living tissue. *Opt Express* **20**: 19697-19707.

126. Deschout, H, Raemdonck, K, Stremersch, S, Maoddi, P, Mernier, G, Renaud, P *et al.* (2014). On-chip light sheet illumination enables diagnostic size and concentration measurements of membrane vesicles in biofluids. *Nanoscale* **6**: 1741-1747.

127. Ruthardt, N, Lamb, DC and Brauchle, C (2011). Single-particle tracking as a quantitative microscopy-based approach to unravel cell entry mechanisms of viruses and pharmaceutical nanoparticles. *Mol Ther* **19**: 1199-1211.

128. Reuel, NF, Dupont, A, Thouvenin, O, Lamb, DC and Strano, MS (2012). Three-dimensional tracking of carbon nanotubes within living cells. *ACS Nano* **6**: 5420-5428.

129. Berg, HC (1971). How to track bacteria. *Review of Scientific Instruments* **42**: 868-871.

130. Kao, HP and Verkman, AS (1994). Tracking of single fluorescent particles in three dimensions: use of cylindrical optics to encode particle position. *Biophys J* **67**: 1291-1300.

131. Pavani, SR and Piestun, R (2008). Three dimensional tracking of fluorescent microparticles using a photon-limited double-helix response system. *Opt Express* **16**: 22048-22057.

132. Thompson, MA, Lew, MD, Badieirostami, M and Moerner, WE (2010). Localizing and tracking single nanoscale emitters in three dimensions with high spatiotemporal resolution using a double-helix point spread function. *Nano Lett* **10**: 211-218.

133. Prabhat, P, Ram, S, Ward, ES and Ober, RJ (2004). Simultaneous imaging of different focal planes in fluorescence microscopy for the study of cellular dynamics in three dimensions. *IEEE Trans Nanobioscience* **3**: 237-242.

134. Toprak, E, Balci, H, Blehm, BH and Selvin, PR (2007). Three-dimensional particle tracking via bifocal imaging. *Nano Lett* **7**: 2043-2045.

135. Juette, MF and Bewersdorf, J (2010). Three-dimensional tracking of single fluorescent particles with submillisecond temporal resolution. *Nano Lett* **10**: 4657-4663.

Curriculum Vitae

CURRICULUM VITAE FOR Ph.D. CANDIDATES

For Ph.D. candidates at the Johns Hopkins University School of Medicine

Benjamin Schuster
Name

August 7, 2014
Date of this version

Educational History:

Ph.D. expected	2014	Biomedical Engineering Mentor: Justin Hanes, Ph.D.	Johns Hopkins School of Medicine
B.S.	2008	Biomedical Engineering	University of Minnesota

Other Professional Experience:

Research internship	2007-8	Labs of David Odde, Ph.D. and Victor Barocas, Ph.D.	University of Minnesota
Research internship	2007	Lab of: Sriram Subramaniam, Ph.D.	National Institutes of Health
Research internship	2006	Lab of: Yiannis Kaznessis, Ph.D.	University of Minnesota Bioinformatics Summer Institute

Scholarships and Fellowships:

UROP Fellowship	2007	University of Minnesota	Research stipend
Bentson Family Scholarship	2004-208	University of Minnesota	Tuition support
Presidential Scholarship	2004-2008	University of Minnesota	Tuition support

Award and Honors:

Invited Presentation	2013	12th Annual U.S.-Japan Symposium on Drug Delivery Systems
Biomedical Engineering Summer Intern	2007	National Institutes of Health

Peer-Reviewed Publications:

Schuster BS, Allan DB, Ensign LM, Suk JS, Hanes J. Particle tracking: A powerful and accessible technique for drug and gene delivery research. In preparation, *Advanced Drug Delivery Reviews*.

Schuster BS, Kim AJ, Kays JC, Kanzawa MM, Guggino WB, Boyle MP, Rowe SM, Muzyczka N, Suk JS, Hanes J. Overcoming the cystic fibrosis airway mucus barrier to leading adeno-associated virus gene therapy vectors. *Molecular Therapy*. 2014; 22(8):1484-93.

Kim AJ, Boylan NJ, Suk JS, Hwangbo M, Yu T, **Schuster BS**, Cebotaru L, Lesniak WG, Oh JS, Adstamongkonkul P, Choi AY, Kannan RM, Hanes J. Use of single-site-functionalized PEG dendrons to prepare gene vectors that penetrate human mucus barriers. *Angew Chem Int Ed* 2013; 52:3985-8.

Schuster BS, Suk JS, Woodworth GF, Hanes J. Nanoparticle diffusion in respiratory mucus from humans without lung disease. *Biomaterials* 2013; 34:3439-46.

Langham AA, Khandelia H, **Schuster B**, Waring AJ, Lehrer RI, Kaznessis YN. Correlation between simulated physicochemical properties and hemolycity of protegrin-like antimicrobial peptides: predicting experimental toxicity. *Peptides* 2008; 29:1085-93.

Posters, Abstracts, and Presentations:

Schuster BS. "Probing and overcoming extracellular barriers to inhaled nanomedicine." Johns Hopkins Cystic Fibrosis Seminar, Baltimore, MD. May 6, 2014. (Presentation)

Schuster BS, Kim AJ, Kays JC, Kanzawa MM, Suk JS, Hanes J. "The cystic fibrosis sputum barrier to adeno-associated virus gene therapy." 12th Annual US- Japan Symposium on Drug Delivery Systems, Lahaina, Maui, Hawaii. December 18, 2013. (Poster and Invited Presentation)

Birket S, Chu KK, Li Y, Houser GH, Mazur M, **Schuster BS**, Hanes, J, Tearney GJ, Rowe SM. "The relationship between periciliary liquid hydration and mucus transport is affected by bicarbonate transport." 27th Annual North American Cystic Fibrosis Conference. Salt Lake City, UT. October 18, 2013. (Poster)

Donaldson SH, Zeman K, Laube B, Corcoran T, Locke L, Pilewski J, Hanes J, **Schuster B**, Kanzawa M, Rowe SM, Bennett WD. "Effect of Ivacaftor on mucociliary clearance and mucus rheology in patients with a G551D CFTR mutation." 27th Annual North American Cystic Fibrosis Conference. Salt Lake City, UT. October 18, 2013. (Poster)

Wilsterman E, Chu KK, Li Y, Diephuis B, Birket S, **Schuster BS**, Hanes, J, Rowe SM, Tearney GJ. "Rheological validation of particle tracking micro-optical coherence tomography." 27th Annual North American Cystic Fibrosis Conference. Salt Lake City, UT. October 18, 2013. (Poster)

Schuster BS, Suk JS, Woodworth GW, Hanes J. "Nanoparticle diffusion in human respiratory mucus." Johns Hopkins Institute for NanoBioTechnology Symposium, Baltimore, MD. May 17, 2013. (Poster)

Schuster BS. "Nanoparticle diffusion in human respiratory mucus." Biomedical Engineering Society Annual Conference, Atlanta, GA. October 26, 2012. (Presentation)

Schuster BS. "Distribution and clustering of envelope glycoproteins in AIDS viruses." Biomedical Engineering Summer Internship Program, National Institutes of Health, Bethesda, MD. August 9, 2007. (Presentation)

Halper-Stromberg A, Zabransky D, **Schuster BS**, Liu J, Bartesaghi A, Subramaniam S. "Distribution and clustering of envelope glycoproteins in AIDS viruses." Summer Research Poster Day, National Institutes of Health, Bethesda, MD. August 1, 2007. (Poster)

Schuster BS. "Development of a QSAR for antimocrobial peptides." Bioinformatics Summer Institute, University of Minnesota, Minneapolis, MN. August 4, 2006. (Presentation)

Service, Leadership, and Teaching Experience:

Teaching Experience

Fall 2010: Systems Bioengineering III: From Genes to Cells, teaching assistant
Professor: Dr. Joel Bader

Mentoring of undergraduate students:

Joshua Kays (JHU BME), 9/2012 – 5/2014, Provost's Undergraduate Research Award winner
Mia Kanzawa (JHU BME), 1/2012 – 5/2014

Mentoring of high school students:

Diversity and Academic Advancement Summer Institute, Summers 2010-2013. Mentored Dunbar High School students during six-week (25 hr/wk) summer internships in lab. Students mentored: Mark Banks, Nelson Buchanan, Myron Jackson.

Incentive Mentoring Program, 2009-2012. Advised, mentored, and tutored an at-risk Baltimore teenager as part of a family of mentors. Served as "Head of Household" for 1 year.